

**DYNAMICS OF MAGNETIC FLUX TUBES
IN ADVECTIVE FLOWS AROUND
GALACTIC AND EXTRAGALACTIC BLACK HOLES**

**Thesis submitted for the degree of
Doctor of Philosophy (Science)
in Physics (Theoretical)**

**by
Arnab Deb**

**Department of Physics
University of Calcutta
2019**

abstract

Processes by which compact objects such as black holes gravitationally capture ambient matter either from winds of a collection of stars or from a single companion star is called accretion. Though most of the matter could fall onto compact objects, a fraction of it is generally ejected as an outflow which is eventually collimated and accelerated to produce radio jets observed in quasars and microquasars. According to the transonic flow models of Chakrabarti and his collaborators (Chakrabarti 1989, 1990, 1999, 1996; Molteni, Lanzafame, Chakrabarti 1994; Giri, Chakrabarti 2010, 2012, 2014 and references therein) thermodynamically radiation pressure or ion pressure supported and hydrodynamically centrifugal pressure supported boundary layer (i.e the post-shock region) of a black hole is the source of this outflowing matter. Observations in the two spectral regions of the electromagnetic spectrum, in the domain of the hard X-rays on one hand (Sunyaev et al 1991; Paul et al 1991), and in the domain of radio wavelengths on the other hand, revealed the existence of relativistic jets in microquasars (Mirabel et al 1992; Mirabel & Rodriguez 1998). Relativistic jets with sudden enhancement of outflow rate can be produced when the inner part of the disk is destroyed and the matter is squeezed (Chakrabarti & D'Silva, 1994; Nandi et al. 2001) by magnetic stress. Clearly, magnetic field is seen to play a major role in origin, acceleration and collimation of these relativistic jets. We extend the earlier work of Chakrabarti & D'Silva (1994) and D'Silva & Chakrabarti (1994) to study the effects of predominantly toroidal magnetic flux tubes on the dynamics of matter which is falling towards the black hole or are ejected as the outflow. The processes involved are hydrodynamic and hydromagnetic in nature. Understanding of the launching of jets translates to precise understanding of magnetic activity at the base of the jets. Prior to this, fields must be brought to this region through advection from the surrounding stars. These flux tubes are compressed by the disk, amplified by the shear, convection, and advection and finally eliminated by the buoyancy effect.

In this thesis, we survey the dynamics of the toroidal flux tubes by solving equa-

tions of motion of flux tubes using density, velocity, and temperature profiles which we obtain from time dependent solutions of axially symmetric dimensional accretion flows around a black hole. The simulations were carried out using finite difference method and Total Variation Diminishing (TVD) scheme for the Schwarzschild black holes. Our aim is to check whether the flux tubes contribute to increase in the outflow rates, and the outflow velocities by squeezing the jet matter and improve the collimation of outflows due to the presence of the hoop stress of toroidal field component. It is seen that depending on the cross sectional radius of the flux tubes which control drag forces, these field lines may be advected towards the central object or oscillate vertically and radially before eventually escaping out of the thick disk through the funnel wall (pressure zero surface) along with the jets. At the same time, we also wish to investigate the flow and spectral properties of a truly two dimensional flow when no reflection symmetry on the equatorial plane is assumed. We study the effects of viscosity and cooling on this type of flow and study its stability properties. We also focus on how the flux tubes behave if they are injected in a viscous flow.

In chapter 1 we give a general introduction about the properties of black hole and accretion flow models. We also discuss about the ubiquitous nature of jets and outflows which can be seen in huge ensemble of astrophysical objects. We present a brief review about the magnetized disc and how it is connected to the creation of highly collimated jets.

In chapter 2 we discuss about the governing hydrodynamic equations and also the numerical schemes involved in solving them. We presented a brief discussion on how the hydrodynamic equation is written in terms of conservative and primitive variables and how the eigenvalues and eigenvectors of the Jacobian matrices are constructed. We add the magnetic force term to the source term to incorporate the effects of the magnetic fields and study the dynamics of it. Following the prescription in Giri, Chakrabarti (2013) and Giri, Garain, Chakrabarti (2015) we add radiative cooling and viscosity to produce the Keplerian disc with magnetic fields.

In chapter 3 we discuss about the simulation set up and initial conditions necessary to undergo the simulation of inviscid and viscous non magnetized as well as magnetized flow. Here we couple the time dependant hydrodynamic code with the code to compute the trajectories of the flux tube by using the velocity, temperature, and pressure profile calculated by the hydrodynamic code at every time instant. We also remove the reflection symmetry along the equatorial plane and test the code using spherical Bondi flow for both magnetized and non mag-

netized cases.

In chapter 4 we discuss the results of a bi-quadrant inviscid flow simulation where reflection symmetry is not invoked. Doing so we have allowed the flow to undergo horizontal as well as vertical oscillations. It is found that as we go towards higher angular momentum, the flow becomes very turbulent and it is observed from the simulation that at some times, a part of the CENBOL is shifted towards the upper quadrant of the flow and for other times the CENBOL is shifted towards the lower quadrant. This shifting of CENBOL has an effect on the outflow also. When the CENBOL shifts towards the upper quadrant, the total outflow from the upper quadrant becomes significantly higher than that from the lower quadrant and vice versa. As a result, the outflows from upper and lower quadrants show anti-correlation. In chapter 5 we have discussed the simulation of viscous flows and it can be seen that in the presence of radiative cooling, depending on the optical depth, the Keplerian disc is formed and the temperature inside the disc has the distribution of $\sim r^{-0.79}$ which almost matches with the analytical distribution of $\sim r^{-3/4}$.

In chapter 6, we studied the dynamics of magnetic flux tubes which are released at the outer edge of a time dependant two quadrant thick advective disc and their role in collimation and acceleration of the jet and outflow from the upper boundary. We also examine whether these magnetic flux tubes aid in the acceleration and collimation of the jets or not.

In chapter 7, we draw the conclusions and discuss our future plan.

Acknowledgments

I express my sincere thanks and gratitude to my supervisor Prof. Sandip K. Chakrabarti for his immense help in finishing this thesis work and to my development as a physicist. I am obliged to my group members Dr. Kinsuk Giri, Dr. Sudip Garain, Dr. Himadri Ghosh, Dr. Arka Chatterjee, Abhishek Roy, Arindam Ghosh, Ayan Bhattacharjee, Anuvab Banerjee, Prantik Nandi, Piklu Santra for discussion on physics and constant encouragement.

My sincerest thanks go out to my colleagues of S.N. Bose National Centre for Basic Sciences for their assistance and motivation throughout. I take the opportunity to convey my sincere gratitude to all the members of Indian Centre for Space Physics as well.

I am specially thankful to my seniors Dr. Kinsuk Giri, Dr. Sudip Garain, Dr. Himadri Ghosh for their guidance throughout this journey. Most importantly I would like to acknowledge the support of my family. The love and sacrifice of my parents enabled me to pursue this career. I am grateful to my wife, Pooja Mitra, who has been a constant source of inspiration. I would like to thank my fellow friends for being there always.

Finally I would like to acknowledge S. N. Bose National Centre for Basic Sciences, Kolkata, India for providing me the opportunity, academic environment and facilities during my Ph. D. tenure.

List of publications

1. *"Numerical simulation of vertical oscillations in an axisymmetric thick accretion flow around a black hole"*
Arnab Deb, Kinsuk Giri, Sandip K. Chakrabarti
Monthly Notices of the Royal Astronomical Society, Volume 462, Issue 4, p.3502-3510 .
2. *"Dynamics of magnetic flux tubes in an advective flow around a black hole"*
Arnab Deb, Kinsuk Giri, Sandip K. Chakrabarti
Monthly Notices of the Royal Astronomical Society, Monthly Notices of the Royal Astronomical Society, Volume 472, Issue 2, p.1259-1271.

List of Figures

- 1.1 Comparison between general relativistic and Newtonian effective potentials. Effective potential with GR approach is drawn for $\lambda = 0, 3, 2\sqrt{3}, 3.7, 4, 4.5$ and Newtonian effective potential is drawn for $\lambda = 3, 2\sqrt{3}, 4.5$. The dashed line for which $V_{eff} = 1$ denotes rest mass energy of particle falling into the black hole. 4
- 1.2 Hubble Space telescope images of three YSO (also called Herbig-Haro(HH) objects) jets. The HH 30 jet is observed to emerge from the embedded source surrounded by a disk of gas and dust. Terminal bright bow shocks are clearly seen on both sides of the HH 46 jet, and a chain of emission knots in HH 34 jet. (*Credit: C. Burrows (STScI & ESA), J. Hester (Arizona State University), J. Morse/STScI and NASA*) 13
- 1.3 The top left picture is a radio image of M87, which is taken with the Very Large Array (VLA) radio telescope which shows giant bubble-like structures where radio emission is thought to be powered by the jets. The top right picture is a visible light image of the giant elliptical galaxy M87. The bottom picture is a Very Long Baseline Array (VLBA) radio image of the region close to the black hole. (*Credit: HST press release*) 14
- 1.4 Images obtained with the Very Large Array (VLA) of jets in a FR I source 3C31 at the radio freq. 1.4 GHz and 8.4 GHz. (*Credit: NRAO/AUI by R. Laing, A. Bridle, R. Perley, L. Feretti, G. Giovannini, and P. Parma (Laing 1996)*) 16
- 1.5 Trajectories of toroidal flux tubes released at the positions $R = 4, 5, 6, 8, 10 r_g$ drawn on the $R - z$ plane. This figure is drawn for $n = 0$ i.e. for constant angular momentum. This figure is reproduced using the parameters from Chakrabarti & D'Silva, 1994. 19

1.6	Trajectories of toroidal flux tubes released at the positions $R = 5, 10 r_g$ drawn on the $R - z$ plane. This figure is drawn for $n = 0$ i.e. for constant angular momentum. This figure is reproduced using the parameters from D'Silva & Chakrabarti, 1994.	20
3.1	A schematic diagram of the system under consideration. Solid box is our computational region on the $r - z$ plane. No reflection symmetry along the equatorial plane has been assumed.	44
3.2	Density colour plot and velocity vector plot of a spherical Bondi flow for non-magnetized case. No reflection symmetry along the equatorial plane has been assumed.	49
3.3	Density colour plot and velocity vector plot of a spherical Bondi flow for non-magnetized case. No reflection symmetry along the equatorial plane has been assumed.	50
3.4	Density colour plot and velocity vector plot of a spherical Bondi flow for magnetized case. No reflection symmetry along the equatorial plane has been assumed.	51
4.1	Density and velocity vector map to show quasi-periodic formation and deformation of the CENBOL at (a) $t = 21.36$ s, (b) 21.84 s, (c) 22.08 s and (d) 24.95 s. Specific angular momentum is considered to be $\lambda = 1.6$. In (a), high density region due to centrifugal supported boundary layer (CENBOL) has a symmetric shape. In (b), symmetry is about to be broken due to vertical oscillation of the perturbing mass. In (c), CENBOL is deformed but not destroyed. In (d), the CENBOL is restored back (Deb, Giri, Chakrabarti, 2016).	55
4.2	Radial distribution of the (a) radial velocity component and (b) radial Mach number (v_r/a) on the equatorial plane. Time is $t = 24.95$ s and specific angular momentum is $\lambda = 1.6$. We clearly see the slowing down of matter at the centrifugal barrier (a) and a supersonic to sub-sonic transition (b) forming a shock (Deb, Giri, Chakrabarti, 2016).	56

- 4.3 Density and velocity vector plots of the accretion flow to show instability within the flow. (a) and (c) show that the CENBOL is shifted above: flow density is higher in the upper quadrant and (b) and (d) show that the CENBOL is shifted below: flow density is higher in the lower quadrant. Plots are drawn at $t = 17.34, 22.57, 40.08,$ and 43.2 seconds respectively. Specific angular momentum is considered to be $\lambda = 1.7$ (Deb, Giri, Chakrabarti, 2016). 58
- 4.4 Time variation of the ratio between the total outflow rate (\dot{M}_{out}) and the total inflow rate (\dot{M}_{in}) showing an anti-correlated behavior. When the outflow rate from the upper boundary is high, the outflow rate in the lower boundary is low and vice versa. Here (a) $\lambda = 1.7$ and (b) $\lambda = 1.8$. Dot-dashed curve represents the outflow inflow rate ratio in upper quadrant, solid curve represents the ratio in lower quadrant, and dashed curve represents the mean value (time averaged) of the outflow inflow rate ratio. We note that the mean outflow rate as well as the degree of deviation from the mean is higher when angular momentum is higher (Deb, Giri, Chakrabarti, 2016). 60
- 4.5 Plot of cross correlation between total outflow rates from upper and lower quadrant to show the anti-correlated behavior of the outflow. Fig 4.5(a) is drawn for $\lambda = 1.7$ and 4.5(b) is drawn for $\lambda = 1.8$ (Deb, Giri, Chakrabarti, 2016). 61
- 4.6 Time variation of shock location for two quadrant flow with $\lambda = 1.6$ angular momentum and their respective power density spectra. Group (i) shows the shock location variation in upper (a) and lower (b) quadrants. Group (ii) shows the power density spectra (PDS) of these locations. We see evidence of a prominent peak at $\sim 0.16\text{Hz}$ in both the cases and a harmonics at $\sim 0.32\text{Hz}$ 62
- 4.7 Same as in Fig. 4.6 for $\lambda = 1.7$. Note that the shock oscillates around a larger mean location, though the symmetry in upper and lower quadrant is lost. The power density spectra have several peaks and the oscillation is more chaotic. 63

4.8	Same as in Fig. 4.6 for $\lambda = 1.8$. Note that the shock oscillates around a mean location similar to what we observed for $\lambda = 1.7$, perhaps due to the post-shock turbulence. The symmetry in upper and lower quadrant is lost. The power density spectra have several peaks and the oscillation is more chaotic.	64
5.1	Variation of viscosity parameter (α) along the z -direction. Here, $\alpha_{max} = 0.012$	68
5.2	Density and velocity vector map to show the gradual formation of Keplerian disc at (a) $t = 9.6$ s, (b) 24.4 s, and (d) 95 s. Specific angular momentum is considered to be $\lambda = 1.7$	69
5.3	A comparison between specific angular momentum distribution at the equatorial plane with the Keplerian angular momentum distribution. Injected angular momentum is 1.7 and figures are drawn for different times as specified in fig 5.2.	70
5.4	Mach number distribution for the subsonic (i) and supersonic (ii) flow.	71
5.5	Temperature variation of the fluid flow. Temperatures are written in KeV unit. Here, we have plotted $\log_{10} T$. This snapshot of the temperature variation is taken for time $t = 95$ s	72
5.6	Radial variation of the temperature of the simulated Keplerian disc. Temperatures are written in KeV unit. Here, we have used $\log - \log$ scale. The index γ of the radial variation of temperature $T(r) \sim r^{-\gamma}$ is 0.797	73
6.1	Trajectories of flux tubes injected from the outer boundary i.e., $r = 200r_g$ and $\theta = 89^\circ$ with zero initial velocity. Trajectories are in $r = R \sin \theta$ vs. $z = R \cos \theta$ plane. The trajectories are drawn for a flow with angular momentum $\lambda = 1.6$ and energies 0.001 (upper panel) and 0.002 (lower panel). σ is the cross sectional radii of the injected flux tubes. Here σ values are $0.001 r_g$, $0.005 r_g$, $0.01 r_g$ and $0.1 r_g$ (Deb, Giri, Chakrabarti 2017).	79

- 6.2 Trajectories of the flux tubes injected from the outer boundary i.e., $r = 200r_g$ and $\theta = 89^\circ$ with zero initial velocity. Trajectories are drawn in $r = R \sin \theta$ vs. $z = R \cos \theta$ plane. The trajectories are drawn for a flow with angular momentum $\lambda = 1.7$ and energies 0.006 (lower panel) and 0.002 (upper panel). σ signifies the cross sectional radii of the flux tubes for which the trajectories are drawn. Here σ values are $0.001 r_g$, $0.005 r_g$, and $0.1 r_g$ (Deb, Giri, Chakrabarti 2017) 80
- 6.3 Trajectory of the flux ring having cross sectional radius (σ) $0.01 r_g$ released at $r = 200r_g$ and $\theta = 89^\circ$ with zero initial velocity. Angular momentum of the flow is 1.7 and the flow energies are $\varepsilon = 0.002$ (upper panel) and 0.006 (lower panel) (Deb, Giri, Chakrabarti 2017). 81
- 6.4 Trajectories of flux tubes having same σ but with different flow energies (marked) are drawn to demonstrate energy dependence of the trajectory of the flux tube inside the disc. $\varepsilon = 0.001$ & 0.002 are marked on the curves. Angular momentum of the flow is 1.6 (Deb, Giri, Chakrabarti 2017). 82
- 6.5 Same as in Fig. 6.4 except $\varepsilon = 0.002$ & 0.006 and specific angular momentum of the flow is 1.7 (Deb, Giri, Chakrabarti 2017). 83
- 6.6 Time variations of radial component of the entropy gradient plot of the flow having angular momentum (λ) 1.6 and energy (ε) 0.002. Both the plot shows that the radial component of the entropy gradient switches sign from positive to negative and vice versa. This switching is responsible for providing an anchorage of the oscillating flux tubes and consequently may cause a corona like structure. Two plots are drawn at $t \sim 4.06$ & 6.33 s respectively (Deb, Giri, Chakrabarti 2017). 85
- 6.7 z variation of the radius of cross section(σ) of flux tubes released in an inviscid accretion flow with energy $\varepsilon = 0.002$ and angular momentum(λ) 1.6. Each panel shows the σ variation for different initial cross sectional radius. initial σ 's are $\sigma = 0.001, 0.005, 0.01, \& 0.1 r_g$ (Deb, Giri, Chakrabarti 2017) 86

- 6.8 z variation of the radius of cross section (σ) of flux tubes released in an inviscid accretion flow with energy $\varepsilon = 0.006$ and angular momentum (λ) 1.7. Each panel shows the σ variation for different initial cross sectional radius. initial σ 's are $\sigma = 0.001, 0.005, 0.01, \& 0.1 r_g$ (Deb, Giri, Chakrabarti 2017). 87
- 6.9 Velocity vector plot of the flow with magnetic flux tubes. (a,b), (c,d),(e,f), and (g,h) are velocity vector fields of the flow having magnetic flux tube of cross sectional radii 0.001, 0.005, 0.01, $0.1 r_g$ respectively. Angular momentum and specific energy are 1.6 and 0.002 respectively. The times specified are the same as in Fig. 6.10. The dots signify the position of flux tube at the respective times specified in each panel. 89
- 6.10 Radial distribution of the outflow rate (\dot{M}_{out}) of the flow having the specific angular momentum (λ) = 1.6 and energy (ε) = 0.002. The black solid curve represents the outflow rate for the flow with magnetic field and red solid curve (dot-dashed in hard copies) denotes the result in non-magnetic case. The upper two rows (a-h) of the plot show the collimation of the outflow from upper and lower quadrants respectively for different flux tubes with different σ . The lower two rows (i-p) depict the gradual reduction of the collimating effects once the flux tube has escaped or fallen into the black hole. The vertical dashed lines drawn in panels of first two rows depict the position of the flux tube at time for which the outflow rates are drawn (Deb, Giri, Chakrabarti 2017). 90
- 6.11 Same as Fig. 6.10, but $\lambda = 1.7$ and $\varepsilon = 0.006$ (Deb, Giri, Chakrabarti 2017). 91
- 6.12 Time variation of the total outflow rate for magnetic and non-magnetic cases with angular momentum 1.6 and specific energy 0.002. Panels (a,c,e,g) represents net outflow rate for upper quadrant and panels (b,d,f,h) represents total outflow rate for lower quadrant of the flow. Solid line represents total outflow rate for magnetic cases and dashed line represents the non-magnetic cases. Panels (a,b), (c,d), (e,f), and (g,h) are drawn for flux tube with cross sectional radii 0.001, 0.005, 0.01, $0.1 r_g$ (Deb, Giri, Chakrabarti 2017). 92

6.13	Map of the difference between z-velocity of magnetized and non-magnetized flows. (a-d) represent the upper quadrant and (e-h) represent the lower quadrant of a two quadrant flow. Each pair of panels (upper and lower) represent different cross sectional radius. Here, σ ($= 0.001, 0.005, 0.01, 0.1 r_g$). Angular momentum (λ) is 1.6 and specific energy (ε) is 0.002. Each panel is drawn for different times. The circles drawn in the panel give the position of flux tube at times for which the panels are drawn (Deb, Giri, Chakrabarti 2017).	94
6.14	Same as Fig. 13, but $\lambda = 1.7$ and $\varepsilon = 0.006$. The time written in each panel is the same as Fig. 6.11 (Deb, Giri, Chakrabarti 2017). . .	95
6.15	Trajectories of flux tubes injected from the outer boundary i.e., $r = 200r_g$ and $\theta = 89^\circ$ with zero initial velocity. Trajectories are in $r = R \sin \theta$ vs. $z = R \cos \theta$ plane. The trajectories are drawn for a flow with angular momentum $\lambda = 1.6$ and energies 0.001. σ is the cross sectional radii of the injected flux tubes. Here σ values are $0.001 r_g, 0.01 r_g,$ and $0.05 r_g$	96
6.16	Comparison between radial distribution of magnitude of buoyancy force for $m_0 = 0.01$ (green) and $m_0 = 0.5$ (magenta).	97
6.17	Comparison between radial distribution of outflow rate of magnetized and non-magnetized viscous flows. Panel (i) is drawn for upper quadrant and panel (ii) is drawn for lower quadrant at $t = 1.2s$.	98

Contents

1	Introduction	1
1.1	Black Holes- A Brief Overview	2
1.1.1	Gravitational Field: Difference between a Newtonian star and a Black hole	3
1.1.2	Pseudo-Newtonian approach	5
1.2	Accretion processes	5
1.3	Overview of theoretical disc models	7
1.3.1	Standard disc model	7
1.3.2	Thick disc model	9
1.3.3	Advective Accretion disc	10
1.4	Jets and Outflows and importance of magnetic fields	11
1.4.1	Jets from Young Stellar Objects (YSO)	12
1.4.2	Jets from AGNs	13
1.4.3	Jets from Stellar Mass Black Hole & Microquasars:	15
1.4.4	Magnetized disc: A Brief Review	17
2	Governing equations and Computational scheme	21
2.1	Hydrodynamic flow equation	21
2.2	equations for inviscid flow	22
2.3	Numerical procedure	25
2.3.1	Finite Difference Method	25
2.3.2	Construction of Flux Jacobians	26
2.3.3	Computation of eigenvalues and eigenvectors	26
2.3.4	Euler equation	27
2.3.5	Total Variation Diminishing scheme	29
2.3.6	grid size and time step	32
2.4	viscous flow	32
2.5	Energy equation and cooling	36
2.6	Magnetized inviscid flow	37
2.6.1	Modified Source term	38

2.6.2	Equation of Motion	39
2.6.3	Adiabatic picture and Calculation of Magnetic Buoyancy:	41
3	Simulation setup & Testing	43
3.1	Simulation Setup	43
3.1.1	Geometry of the System:	44
3.1.2	Computational Box and Initial Conditions	45
3.1.3	Boundary conditions	46
3.1.4	Comment on the Code Units	47
3.2	Testing of the Code: non-magnetized and Magnetized:	47
3.2.1	spherical flow without reflection symmetry	47
3.2.2	Magnetized Spherical Flow	48
4	Non Magnetized Inviscid Flow	52
4.1	Simulation set up and procedure	53
4.2	Instability due to breaking of the reflection symmetry	54
4.2.1	Formation and deformation of CENBOL	54
4.2.2	High angular momentum case	57
4.3	Effect on the inflow-outflow ratio	59
4.4	Time Variation of Shock Location	61
5	Non magnetized viscous flow	66
5.1	Simulation Procedure:	67
5.2	Simulation results	68
6	Magnetized accretion flow	74
6.1	Introduction	74
6.2	Computational procedure	75
6.3	Inviscid magnetized disc	77
6.3.1	Dynamics of magnetic flux tubes inside an advective flow	77
6.3.2	Collimation and acceleration of outflows/jets	87
6.4	Viscous magnetized disc	93

7	Conclusions & Future Work	99
7.1	Conclusions	99
7.2	Future Work	103

Dynamics Of Magnetic Flux Tubes In Advective Flows Around Galactic And Extragalactic Black Holes

Abstract

Though most of the matter gets accreted to the compact object, a fraction of it is ejected as an outflow which is eventually collimated accelerated to produce radio jets observed in quasars and micro-quasars. Relativistic jets with significant matter content are produced when the inner part of the disc is destroyed and evacuated (Chakrabarti & D'Silva, 1994; Nandi et al. 2001). Clearly, Magnetic field has to play a major role in origin, acceleration and collimation of these relativistic jets. One of our goals would be to study the effects of magnetic fields on the origin, acceleration and collimation of jets. The processes involved are hydrodynamic and hydro magnetic in nature. In this thesis, we survey the dynamics of the toroidal flux tubes by solving equations of motion of flux tube using density, velocity, and temperature profiles which we obtain from time dependent solutions of two dimensional (axially symmetric) accretion flows around black hole. The simulations were carried out using finite difference method and Total Variation Diminishing (TVD) scheme for the black holes having Schwarzschild geometry. Our goal is to study dynamics of the flux tubes and to check whether the flux tubes contribute to increase in the outflow rates, to increase in the outflow velocities by squeezing the jet matter or to improve the collimation of outflows due to the presence of the hoop stress due to toroidal fields. It is seen that depending on the cross sectional radius of the flux tubes (which control drag forces), these field lines may move towards the central object or oscillate vertically before eventually escaping out of the funnel wall (pressure zero surface) along with the jets. At the same time, we also wish to investigate flow properties of a truly two dimensional flow when no reflection symmetry on the equatorial plane is assumed. We study the effects of viscosity and cooling on this type of flow and study its stability properties. We focused on how the flux tube will behave if they are to be injected in a viscous flow.

Arnav

Chapter 1

Introduction

Black holes are the most compact objects among all the celestial bodies. The formation of a black hole is due to catastrophic gravitational collapse of matter. Depending on the mass of the progenitor matter, black holes can be classified into three broad classes, namely, stellar mass black holes, intermediate mass black holes and supermassive black holes. Generally, the stellar mass black holes have mass $\sim 10M_{\odot}$ (where $M_{\odot} = 1.99 \times 10^{33}$ g is the mass of the Sun). Many candidates of this variant have been discovered within our very own galaxy (e.g., Cygnus X-1, GRS 1915+105, GRO J1655-40, GX 339-4 to name a few). On the other hand, the super-massive black holes have a mass in the range $\geq 10^6-10^8M_{\odot}$ and are mostly found at centers of galaxies (e.g., Sagittarius A* in our galaxy, M87 etc.). Recently, it has been reported that another class of black holes having mass in the intermediate range ($\sim 10^2 - 10^4M_{\odot}$) may have been observed (Colbert & Mushotzky 1999; Dewangan, Titarchuk & Griffiths 2006; Patruno, Zwart, Dewi & Hopman 2006). These are called intermediate mass black holes. The key factor of a star to collapse to a stellar black hole is its initial mass. Progenitor stars more massive than $\sim 40 - 50M_{\odot}$ end up becoming black holes. The collapse happens when a massive star runs out of nuclear fuel inside it and cannot generate enough outward thermal pressure to balance the effect of the inward gravitational force. In case of black hole formation, the star collapses completely creating a singularity as opposed to the formation of a white dwarf or a neutron star when the star collapses partially as the electron (in case of white dwarf) or neutron degeneracy pressure (in case of neutron star) halts the gravitational pull preventing the star to collapse completely.

Of all the celestial objects, black holes are the simplest as the defining feature of this genre of compact stars is presence of an imaginary boundary known as the event horizon through which nothing including light can come out. Matter

falls towards this boundary due to enormous gravitational pull of the compact object and enters into the horizon with a speed of light. This condition is fixed irrespective of black hole mass and spin. Non-rotating black holes are called Schwarzschild black holes which are the simplest. There are other types of black holes, namely, Kerr black holes (rotating black holes) and Reissner-Nordstrom black holes (black holes having charge but no spin). Accretion is a common phenomenon for many astrophysical systems such as young stellar objects, X-ray binaries, active galactic nuclei etc. In case of X-ray binaries, if the companion is a compact star (black hole or white dwarf or neutron star) they can feed on the companion star of the binary system. Matter from a companion star is accreted to compact objects either by Roche lobe overflow or as winds. Another common feature of many astrophysical systems is the presence of jets and/or outflows. The Jets and outflows for a black hole candidate must originate from the accretion disc itself. As matter approaches towards a black hole, the centrifugal force dominates over the gravitational force and this causes matter to slow down and gradually pile up creating a region which is called Centrifugal pressure supported BOUNDARY Layer or CENBOL. In TCAF (Two Component Advective Flow) paradigm (Chakrabarti 1996, 1997) jets and outflows are strictly coupled to this CENBOL. In §1.1, we describe the properties of black holes in a nutshell and in §1.2, we discuss the basic features and different aspects of accretion processes. We also discuss physics behind accretion. In §1.3, we describe all the theoretical models and finally, we discuss jets and outflows and what role does magnetic fields play in §1.4.

1.1 Black Holes- A Brief Overview

A black hole can simply be defined as a region of spacetime that cannot communicate with the rest of the universe. The boundary of this region is called the event horizon through which nothing, not even light, can come out. Einstein's equations inside this horizon breaks down developing a singularity which is said to be "causally disconnected" from the exterior world. Most general stationary black hole solution is known as the Kerr-Newman metric which depends on three independent observable quantities namely, (i) Mass (M), (ii) Angular momentum (J), and (iii) Charge (Q). As early as 1795 Laplace in his book "*Le Système du Monde*" conjectured that light cannot escape from an object with sufficiently high mass and small radius as a consequence of Newtonian gravity and Newton's corpuscular theory of light. It is well known that the escape velocity of a particle from a

gravitating body of mass M and radius R is,

$$v \geq \sqrt{\frac{2GM}{R}} \quad (1-1)$$

Using this, we can compute the no-escape radius for light which is,

$$R \leq \frac{2GM}{c^2} \quad (1-2)$$

Following Schwarzschild's work in 1916, the metric of the spacetime around the simplest black hole (non-rotating, no charge i.e. $J = 0$ and $Q = 0$) can be written as

$$ds^2 = -\left(1 - \frac{2GM/c^2}{r}\right)dt^2 + \left(1 - \frac{2GM/c^2}{r}\right)^{-1}dr^2 + r^2d\theta^2 + r^2\sin^2\theta d\phi^2 \quad (1-3)$$

From the expression of this metric it is evident that this metric is not valid when $r = \frac{2GM}{c^2}$. It develops a singularity when $r \rightarrow \frac{2GM}{c^2}$ which re-establishes 1-2 through accurate theory of general relativity. This quantity $r = \frac{2GM}{c^2}$ is known as the Schwarzschild radius (r_g) of a black hole with mass M . This is also the position of event horizon. If $1M_\odot$ star could form a black hole, the value of r_g would be 3 km .

1.1.1 Gravitational Field: Difference between a Newtonian star and a Black hole

A test particle around a Newtonian star experiences Newtonian gravitational potential given as,

$$\phi_N = -\frac{GM}{r}. \quad (1-4)$$

and the effective potential of a rotating gas with specific angular momentum λ is

$$\phi_{eff} = \phi_N + \frac{\lambda^2}{2r^2} \quad (1-5)$$

The matter to fall onto the Newtonian star of finite size the gravitational force must overcome the centrifugal barrier and thus it can be easily found that only those matter with angular momentum less than the Keplerian value $\lambda_{Kep,N} = \sqrt{GMr}$ will accrete. In case of the black hole, the situation is quite different as this effective potential can not be obtained by simply adding the components as

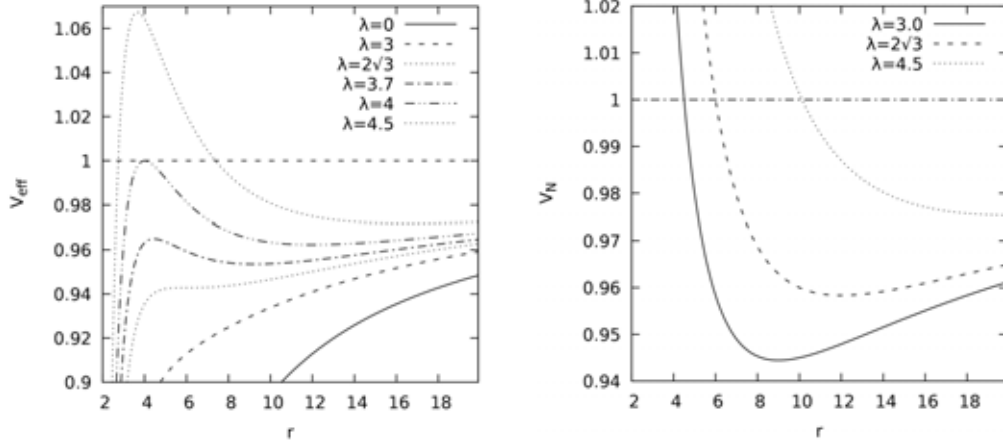


Figure 1.1: Comparison between general relativistic and Newtonian effective potentials. Effective potential with GR approach is drawn for $\lambda = 0, 3, 2\sqrt{3}, 3.7, 4, 4.5$ and Newtonian effective potential is drawn for $\lambda = 3, 2\sqrt{3}, 4.5$. The dashed line for which $V_{eff} = 1$ denotes rest mass energy of particle falling into the black hole.

it was done in case of a Newtonian star. The effective potential can be derived from the metric given in 1-3. The effective potential is given as,

$$V_{eff} = \left\{ \left(1 - \frac{2}{r} \right) \left(1 + \frac{\tilde{\lambda}^2}{r^2} \right) \right\}^{\frac{1}{2}} \quad (1-6)$$

where, $\tilde{\lambda} = \frac{\lambda}{m}$ and $\tilde{E} = \frac{E}{m}$. We can have a general picture of the capture orbits of the particle from this effective potential. If $\frac{\partial^2 V_{eff}}{\partial r^2} > 0$ i.e., V_{eff} is concave upwards then we will have stable circular orbits and if $\frac{\partial^2 V_{eff}}{\partial r^2} < 0$ then we will have unstable circular orbits. Circular orbits (bound) occur when we have $\frac{\partial V_{eff}}{\partial r} = 0$ and $\frac{dr}{d\tau} = 0$. Using the above conditions we get the last stable orbit (marginally stable orbit) $r_{ms} = 6$ (in the units of $\frac{GM}{c^2}$) having the angular momentum $\lambda_{min} \equiv \lambda_{ms} = 2\sqrt{3}$. We have plotted the effective potential for black hole and Newtonian star in Fig 1.1. The dashed horizontal line in both the diagram represents the rest mass energy of the particle. From the potential diagram of Newtonian star we can see that only unbound and bound orbit can exist i.e., no matter how high the energy of the particle is it can not enter in the star but in case of black hole, the diagram of V_{eff} shows that depending of the angular

momentum and the energy of the particle black hole may capture them i.e. particles can exist in capture orbits. From this we can get an idea of initial energy value and angular momentum value of the injected flow which we shall use in the simulation.

1.1.2 Pseudo-Newtonian approach

In case of all astrophysical systems involving black holes it is necessary to use general relativistic approach to solve the problem as long as one is not interested in the region very close to the horizon. Instead of full general relativistic approach, a Paczyński & Wiita type potential can also be used (Paczyński & Wiita 1980). This potential is known as the pseudo-Newtonian potential and is given as,

$$\Phi_{PN} = -\frac{1}{2(r-1)} \quad (1-7)$$

which is written in units of $\frac{2GM}{c^2}$ and thus we can find the effective potential as,

$$V_{ePN} = 1 + \Phi_{PN} + \frac{\lambda^2}{2r^2} \quad (1-8)$$

Using the condition for circular orbits we can find the Keplerian angular momentum distribution to be given as $\sqrt{\frac{r^3}{2(r-1)^2}}$ which is the same as the result produced by the GR approach. Also in pseudo-Newtonian approach the binding energy of the particle at the marginally stable orbit is found to be 6.25% as compared to 5.72% for the GR approach. Thus, this pseudo-Newtonian approach is quite accurate and hence we believe we can use this potential successfully to mimic the GR effects in our simulations.

1.2 Accretion processes

The process by which the diffused gas or matter accumulates around a compact object due to gravity is called accretion. Accretion is the main source of power of these objects and is of high importance in study of X-ray binaries. In case of binaries accretion happens in two ways. First, when the companion star fills the Roche lobe, matter passes through the innermost Lagrange point (L_1) and second, matter coming out of a bloated star in its evolutionary phase may also be captured by the compact object and they enter towards the compact object through

Lagrange points of the Roche lobe. This is known as wind accretion. Apart from these binary systems, isolated compact objects accrete when they pass through interstellar medium or pass by nearby stars and accrete matter from them by tidal effects. Matter falling onto the compact objects, due to its intrinsic angular momentum forms a disc like structure which is called Accretion disc. When accretion takes place, the gravitational energy of the matter is converted into the kinetic energy and heat which is then partly released as radiation. If the accreted matter is ionized hydrogen and radiation exerts force mainly on the electrons by Thomson scattering (because the scattering cross section for protons is a factor $(\frac{m_e}{m_p})^2$ smaller than that of electrons) and this force is felt by the protons also due to Coloumb coupling. There exists a critical limit of the luminosity above which the radiation pressure exceeds gravity and this limit is called Eddington luminosity (L_{Edd}) which is given as,

$$L_{Edd} = \frac{4\pi cGMm_p}{\sigma} = 1.3 \times 10^{38} \frac{M}{M_\odot} \text{ erg s}^{-1}. \quad (1-9)$$

The mass equivalent of L_{Edd} is called the mass Eddington rate (\dot{m}_{Edd}) and is given by,

$$\dot{m}_{Edd} = \frac{L_{Edd}}{c^2} = 1.44 \times 10^{17} \frac{M}{M_\odot} \text{ gm s}^{-1}. \quad (1-10)$$

Since matter coming from the companion star in a binary system possesses some angular momentum, it will not fall freely onto the compact object. Instead it will form a disc like structure. At some distance from the black hole, the centrifugal force is comparable to the gravitational force and the matter begins to rotate in circular orbits. The matter can approach towards the gravitational radius only if there exists some mechanism that can transport the angular momentum outward and this mechanism is believed to be effective due to the presence of viscosity. The efficiency of the mechanism of the angular momentum transport is characterized by the parameter,

$$\alpha = \frac{v_t}{v_s} + \frac{H^2}{4\pi\rho v_s^2} \quad (1-11)$$

where

$$\frac{\rho v_s^2}{2} = \frac{3}{2} \rho \frac{kT}{m_p} + \varepsilon_r \quad (1-12)$$

is the thermal energy density of the matter, ε_r is the energy density of radiation, v_s is the sound velocity and v_t is the turbulent velocity (Shakura & Sunyaev, 1973).

1.3 Overview of theoretical disc models

Historically, the study of accretion started with the study of the interaction of a spherical gravitating star moving supersonically in a uniform medium which is described in the pioneering work of Hoyle and Lyttleton (1939) and Bondi and Hoyle (1944). They tried to quantify the matter accumulation on the star surface from the interstellar medium but they did not consider the pressure term. Bondi in 1952 used the pressure term and obtained the complete transonic flow solution for spherical flows. This solution was later applied by Parker (1959) to explain winds emerging from the sun. The simple spherical flow was then improved upon by addition of angular momentum to it. Many research groups such as, Lynden-Bell (1969); Zeldovich & Novikov (1973); Ostriker et al. (1976); Chakrabarti (1989, 1995, 1996 etc.) have contributed significantly in shaping up the theoretical and analytical aspects of the accretion disc.

1.3.1 Standard disc model

Shakura & Sunyaev (1973) (SS73) proposed a model for accretion disc which they assumed to be thin i.e., the height of the disc at a radial distance is very small compared to the radial distance ($H(r) \ll r$). They also assumed that the matter revolves around the compact object in circular Keplerian orbits. In SS73 paper Newtonian potential was considered and Novikov & Thorne repeated the calculations using General Relativistic approach as well. According to this model viscosity transports angular momentum efficiently and slowly spirals inward with Keplerian angular momentum. The heat generated by the viscous stress is radiated away efficiently in the vertical direction and the disk cools down $kT \ll GMm_p/r$. Some part of the gravitational energy increases the kinetic energy of rotation and other part converted into thermal energy. In the thin disk limit, vertical velocity could be neglected compared to the radial velocity or azimuthal velocity. The accretion rate is considered to sub-Eddington and the pressure is negligible so that the radial force balance equation dictates the specific angular momentum distribution to become Keplerian. A Keplerian circular orbit of radius r around a Newtonian star has an angular momentum,

$$\tilde{l} = (GMr)^{1/2}. \quad (1-13)$$

Let $2H$ be the vertical height of the disk and Σ be the surface density of the disc at radius r . Therefore,

$$\Sigma \equiv \int_{-H}^H \rho dz. \quad (1-14)$$

ρ is computed on the mid plane of the disc. Replacing the integral of products by the product of the averages, the above integral becomes,

$$\Sigma \approx 2H\rho. \quad (1-15)$$

For a Keplerian disk, the stress tensor is

$$t_{r\phi} = \eta r \frac{d\Omega}{dr} = -\frac{3}{2}\eta\Omega, \quad (1-16)$$

where,

$$\Omega^2 = GM/r^3 \quad (1-17)$$

is the Keplerian angular velocity. Let f_ϕ denote the viscous stress exerted in the ϕ direction by the fluid element at r on neighboring element at $r + dr$. The viscous stress is related to the stress tensor according to $f_\phi = -t_{r\phi}$ and therefore,

$$f_\phi = -t_{r\phi} = \frac{3}{2}\eta\Omega = \frac{3}{2}\eta(GM/r^3)^{1/2}. \quad (1-18)$$

Here η is the dynamic viscosity coefficient. In order to obtain a steady disc configuration one has to solve for the equations governing conservation of mass, the specific angular momentum, specific energy and the vertical momentum equilibrium (For detailed discussion see Chakrabarti, 1996 (*Physics Report*), SS73). These are given as,

$$\dot{M} = 2\pi r \Sigma v_r = \text{constant} \quad (1-19)$$

$$\mathcal{G} = f_\phi(2\pi r \cdot 2H)r = \dot{M}(GM)^{1/2}(r^{1/2} - r_I^{1/2}) \quad (1-20)$$

$$F(r) = HQ_+ = \frac{3\dot{M}GM}{4\pi r^3} \left[1 - \left(\frac{r_I}{r}\right)^{1/2}\right]. \quad (1-21)$$

$$\frac{H}{r} \sim \frac{a_s}{v_\phi} \quad (1-22)$$

Using the above mentioned equations as well as the α viscosity prescription we can solve for the physical quantities that are needed to describe structure and thermodynamic property of the disc (Chakrabarti, 1996 (*Physics Report*), SS73). Hence, we have,

$$F(r) = 5 \times 10^{26} M^{-2} \dot{M}_{17} r^{-3} [1 - \sqrt{\frac{6}{r}}] \text{ erg cm}^{-2} \text{ s}^{-1},$$

$$\Sigma(r) = 7\alpha^{-1} M \dot{M}_{17}^{-1} r^{3/2} [1 - \sqrt{\frac{6}{r}}]^{-1} \text{ gm cm}^{-2},$$

$$H(r) = 10^5 \dot{M}_{17} [1 - \sqrt{\frac{6}{r}}] \text{ cm},$$

$$\rho(r) = 3 \times 10^{-5} \alpha^{-1} M \dot{M}_{17}^{-2} r^{3/2} [1 - \sqrt{\frac{6}{r}}]^{-2} \text{ gm cm}^{-3},$$

$$T(r) = 5 \times 10^7 (\alpha M)^{-1/4} r^{-3/4} \text{ K},$$

$$\tau_{es}(r) = 3\alpha^{-1} M \dot{M}_{17}^{-1} r^{3/2} [1 - \sqrt{\frac{6}{r}}]^{-1}$$

All these are written in GM/c^2 unit. The surface temperature can be measured using local effective temperature.

$$T_s(r) = \left[\frac{F(r)}{\sigma} \right]^{1/4} \approx 5 \times 10^7 \left(\frac{M}{M_\odot} \right)^{-1/2} \dot{M}_{17}^{1/4} r^{-3/4} (1 - \sqrt{\frac{6}{r}})^{1/4} \text{ K}. \quad (1-23)$$

In case of stellar mass black holes, the effective temperature peak occurs at around 1 KeV. For AGNs, this peak shifts toward the UV-region and known as the big blue bump (Malkan & Sargent 1982; Malkan 1983; Sun & Malkan 1989; Chakrabarti 2010).

1.3.2 Thick disc model

A thick disc model refers to a geometrically thick disc where $H(r) \sim r$. The disc becomes thick when the thermal energy ($\sim a^2$) becomes comparable with the gravitational energy (Rees 1984, Chakrabarti 1996). Depending upon the cause of dominating pressure, a thick disc can be of two types, (i) radiation pressure dominated (Paczynski & Wiita, 1980) and (ii) ion pressure dominated (ion-tori model) (Rees et al., 1982). When the accretion rate is high, the radiation pressure dominates. The radiation emitted by the infalling matter exerts a significant pressure on the infalling gas and this pressure must be incorporated to find the dynamical structure of the disc. The radial component of the Euler equation can be written as,

$$u \frac{dv}{dr} + \frac{1}{\rho} \frac{dP}{dr} - \frac{\lambda^2}{r^3} + \frac{d\phi}{dr} = 0, \quad (1-24)$$

where λ is the angular momentum of the flow and ϕ is the potential (pseudo-Newtonian or Newtonian) of the gravitational field. Ignoring the advecting term, we can write the angular momentum distribution as (Chakrabarti, 1996a),

$$\lambda \propto \left\{ r^3 \frac{d\phi}{dr} + \frac{r^3}{\rho} \frac{dP}{dr} \right\}^{1/2}. \quad (1-25)$$

We can see that when the pressure gradient term is zero or the pressure itself is zero, the angular momentum distribution is Keplerian. If pressure gradient term is positive, the angular momentum is higher than the Keplerian value and vice versa. In case of ion pressure dominated disc, the accretion rate is very small and due to inefficient radiative cooling, the flow is hotter causing the disc to puff up (Rees, 1984). One important characteristics of the equipotential surfaces of a thick accretion disk around a black hole is the presence of a cusp. The cusp is formed at the inner edge (r_i) between the marginally bound ($2 r_g$) and the marginally stable ($3 r_g$) orbits. Matter fills the closed potential and forms the thick accretion disk, and the excess matter is accreted to the black hole through the cusp.

1.3.3 Advective Accretion disc

Applications of the standard Shakura-Sunyaev disk, the thick disk or the spherical accretion models are limited in the sense that either the advective effect or the pressure gradient effect or the effects of rotation were not taken into account. In the early 90s, Chakrabarti and his collaborators (Chakrabarti, 1990; Chakrabarti & Molteni, 1993; Chakrabarti, 1996b; Molteni, Sponholtz & Chakrabarti, 1996) for the first time presented a global and complete accretion disk solution incorporating all the physical processes while solving the most general flow equations. The aim was to achieve a single paradigm so that all observational features could be explained within a single framework.

An advective disk is the one that advects, or carries ‘something’, namely, the mass, entropy, energy etc. Since this fundamentally means that radial velocity must be important. In advective disks the radial velocity may reach even velocity of light (c) on the horizon. Therefore, before entering into a black hole, matter had to be supersonic (i.e., Mach number, $M = v/a > 1$, where v is the radial velocity and a is the sound speed which can have a maximum value of $c/\sqrt{3}$). Thus, the advective flow must pass through at least one sonic point (i.e., the flow is transonic) as a sub-Keplerian flow (angular momentum must be less than the

Keplerian angular momentum). One more aspect of the advective disk is that the infall time close to the black hole is so small that the viscosity, which transports the angular momentum and thus makes accretion possible, does not get sufficient time to transport the angular momentum. Hence the angular momentum λ of the flow remains almost constant close to the black hole. Since the centrifugal force $\sim \lambda^2/r^3$ grows at a much faster rate near the black hole as compared to the gravitational force $\sim 1/r^2$, the matter slows down. The incoming matter piles up on the top of this matter and a shock may form. Dividing the entire parameter space spanned by angular momentum λ and specific energy ϵ of the flow, one can show (Chakrabarti, 1990) that for a large region of the parameter space, a stable solution can have a standing shock. Depending on physical parameters, a shock may be oscillating in nature or it may even be absent. At the shock, the flow kinetic energy is converted into thermal energy forming a hot Compton cloud which can inverse-Comptonize the soft photons into hard photons and produce outflows and winds. This region is called CENtrifugal pressure supported BOundary Layer (CENBOL).

Two Component Advective Flow (TCAF) is a combination of two types of flows: Keplerian component which is accreted in long, viscous time scale and the initially sub-Keplerian component, which plunges in short, free-fall time scale. Inside the post shock region or CENBOL, the Keplerian matter mixes up with the sub-Keplerian halo and forms a single component (Chakrabarti, 1997 and references therein). The low energy photons or soft photons generated from the Keplerian disc are intercepted by the hot electron cloud or CENBOL and are energized by inverse comptonization. Eventually they emerge as hard photons.

1.4 Jets and Outflows and importance of magnetic fields

Astrophysical jets are a ubiquitous phenomenon along which mass, momentum, energy, and magnetic flux are channeled from stellar, galactic, and extra galactic objects to the outer medium. Geometrically, these jets have very small angle i.e., narrow conical or cylindrical/semi-cylindrical protrusions. Highly collimated supersonic jets and less collimated outflows are observed to emerge from a wide variety of astrophysical objects. They can be seen in young stellar objects, protoplanetary nebulae, compact objects such as black holes, microquasars, X-ray binary stars, and in the active galactic nuclei (AGNs). Jets span a large range of luminosity and degree of collimation, starting from those emerge from the AGNs which produce most powerful jets to the jets associated to low-mass young stel-

lar objects within our own galaxy. In the intermediate region of this spectrum, between two extreme cases, evidences of outflows associated with neutron stars, massive X-ray binary systems, and galactic stellar mass black holes can be found. Less collimated supersonic outflows are often seen to emerge from massive hot stars in their late stages of evolution, e.g., the LBV (luminous-blue-variable) stars and also from low mass stars in their late evolutionary stages, like the protoplanetary nebulae. Most of these outflows, though they are different in various aspects such as physical scales and power, are morphologically very similar which indicates that they are originated through common physical processes. All the jet classes share common properties. In general, they (i) are highly collimated and in most cases two-sided, (ii) originate from the vicinity of compact objects, (iii) show a chain of more or less regularly spaced emission knots which in some cases move at high speeds away from the central source, (iv) often terminate in emission lobes, which are believed to be the “working surfaces” where the jets shock against the ambient medium, (v) are associated with the magnetic fields, and (vi) show evidences of accretion of matter onto central source via an accretion disc.

1.4.1 Jets from Young Stellar Objects (YSO)

Protostellar jets are produced during the major accretion phase of the star formation process, i.e., during the class 0 and I phases of the life of a protostellar core/young star. This phase of the star formation process is thought to last about 10^5 yr (Lada 1999). The YSO jets have typically projected lengths between 0.01-few pcs. Many of them can be classified as Herbig-Haro(HH) objects which show a linear chain of bright, traveling knots. These jets often terminate in a bow shock like structure where the jet impacts with a slower ambient medium (Fig. 1.3). Outflows from young stars manifest observational data over a wide range of wave lengths from the ultraviolet to the radio. From the available high resolution observations it can be seen that the flow coming out of a stellar or circumstellar region is bipolar. Well collimated flow sweeps up the ambient molecular gas in its vicinity, creating two cavities oriented in opposite directions with respect to the central star. The molecular gas displaced from the cavities expands in the form of irregular lobes and incomplete shells and constitutes the CO outflow. Bipolar outflows from YSOs contain ionized, atomic, and molecular gas. It has mainly two components, i) relatively cold molecular gas traced by classical (SHV) CO outflows, and ii) EHV CO component. All the luminous structures produce

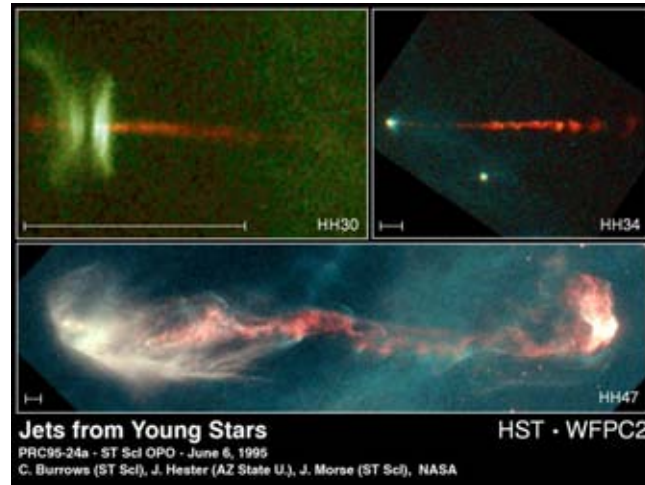


Figure 1.2: Hubble Space telescope images of three YSO (also called Herbig-Haro(HH) objects) jets. The HH 30 jet is observed to emerge from the embedded source surrounded by a disk of gas and dust. Terminal bright bow shocks are clearly seen on both sides of the HH 46 jet, and a chain of emission knots in HH 34 jet. (Credit: C. Burrows (STScI & ESA), J. Hester (Arizona State University), J. Morse/STScI and NASA)

emission line spectra in the mainly in optical and infrared bands. Spectral lines give information on local temperature and density, on the bulk velocity of the jet emitting matter and on the presence of shocks along the jet. Prominent features include hydrogen Balmer lines and transitions of neutral atoms and ions. High ionization and excitation lines can also be observed along with very low excitation spectrum in the inner jet region.

1.4.2 Jets from AGNs

About 10% of AGNs, besides accreting matter, are able to expel a part of it at relativistic speeds in two opposite directions forming jets with energy in the radio range. These radio jets can reach up to a few Mpc s in size and tens of times the radius of host galaxies. AGNs having relativistic jets were believed to have elliptical as host galaxies but this paradigm was challenged when narrow line ($FWHM \leq 2000kms^{-1}$) Seyfert-1 galaxies were observed. The radio emission produced by jets is only a small fraction of the entire electromagnetic power they emit. Since most of it is produced in mm-optical and in γ -ray band, the electro-

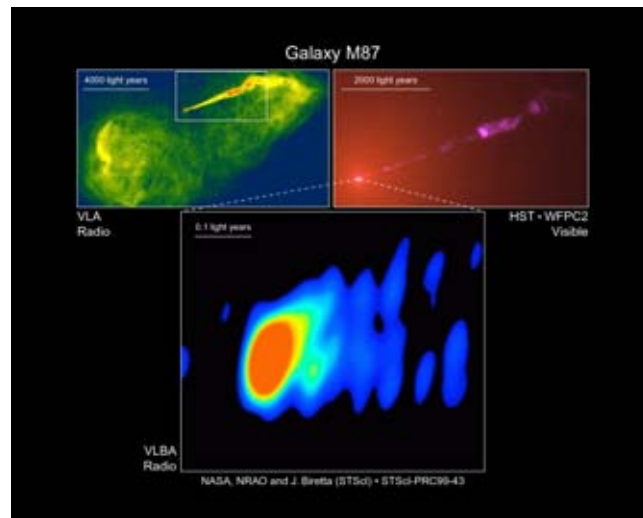


Figure 1.3: The top left picture is a radio image of M87, which is taken with the Very Large Array (VLA) radio telescope which shows giant bubble-like structures where radio emission is thought to be powered by the jets. The top right picture is a visible light image of the giant elliptical galaxy M87. The bottom picture is a Very Long Baseline Array (VLBA) radio image of the region close to the black hole. (Credit: HST press release)

magnetic output is only a small fraction of the total power carried by the jet. Most of it is spent to give sufficient kinetic energy to the matter in order to achieve relativistic speed and to move the magnetic field, i.e., the Poynting flux. In powerful sources it reaches large radio structures like hot spots and the radio lobes which are absent in less powerful candidates. Powerful sources are called FR II radio galaxies and weaker ones are called FR I radio galaxies. Since the emitted matter is moving with a bulk Lorentz factor, we see that for the part of the jet pointing towards us, the intensity gets amplified and if the jet points in the opposite direction, the intensity is suppressed. The large structures (e.g., hot spots, radio lobes) being static, their emission remains isotropic. The ratio between the jet emission and the radio lobe emission is thus a strong function of the viewing angle. Hence, it can be inferred that, (I) at very low frequencies the emission is always dominated by the lobe, irrespective of the viewing angles, (II) Lobe and jet emission are equal at some frequency which increases as the viewing angle increases, and (III) aligned sources give a flat radio spectrum and misaligned sources show a steep radio spectrum. Sources whose jets are pointed towards the observer are

called blazars. Classifications of blazars are done depending on either how they were discovered or the location of their synchrotron peak, or the presence or absence of broad emission lines.

$$EW = \int \frac{F_0 - F_\lambda}{F_0} d\lambda$$

those with weak or absent line and $EW < 5 \text{ \AA}$ are called BL Lac objects and those with strong emission lines and $EW > 5 \text{ \AA}$ are called Flat Spectrum Radio Quasars.

1.4.3 Jets from Stellar Mass Black Hole & Microquasars:

Microquasar or relativistic jets from stellar mass black holes in binary stars emitting X-rays (Black Hole X-Ray Transients or BHXRTs), are scaled down versions of AGN jets, typically extending for 1 pc. Since all the timescales for black holes are proportional to mass, the accretion-ejection phenomena is expected to last much shorter as compared to AGNs. As matter approaches near the compact object the centrifugal force becomes comparable to the gravitational force and thus slowing the inflow considerably and the flow may suffer a shock, where the Mach number jumps discontinuously from supersonic to subsonic. This region may be thin or extended depending upon whether the shock condition namely Rankine-Hugoniot conditions are satisfied or not. This hot, slowed-down region puffs up and forms a torus called CENBOL. The outflow can be formed in this region since it is hotter as compared to a disk. At the shock, a fraction of accreting matter bounces off the centrifugal barrier and is ejected along the axis of symmetry as outflows or jets. Some amount of this outflow also fed back to the sub-Keplerian flow. It has been shown that the collimation of jets is possible by toroidal magnetic field which is accreted by the compact object from the companion. Since the azimuthal component of the velocity is very high, it will convert the accreted random magnetic flux tubes into toroidal flux tubes. These flux tubes can either be stored or expelled towards the funnel and due to buoyancy it will float up. These expelled flux tubes will then eventually puff up. Since matter cannot radially expand through the flux tubes due to Lorentz force, the flux tubes would end up collimating the outflows.

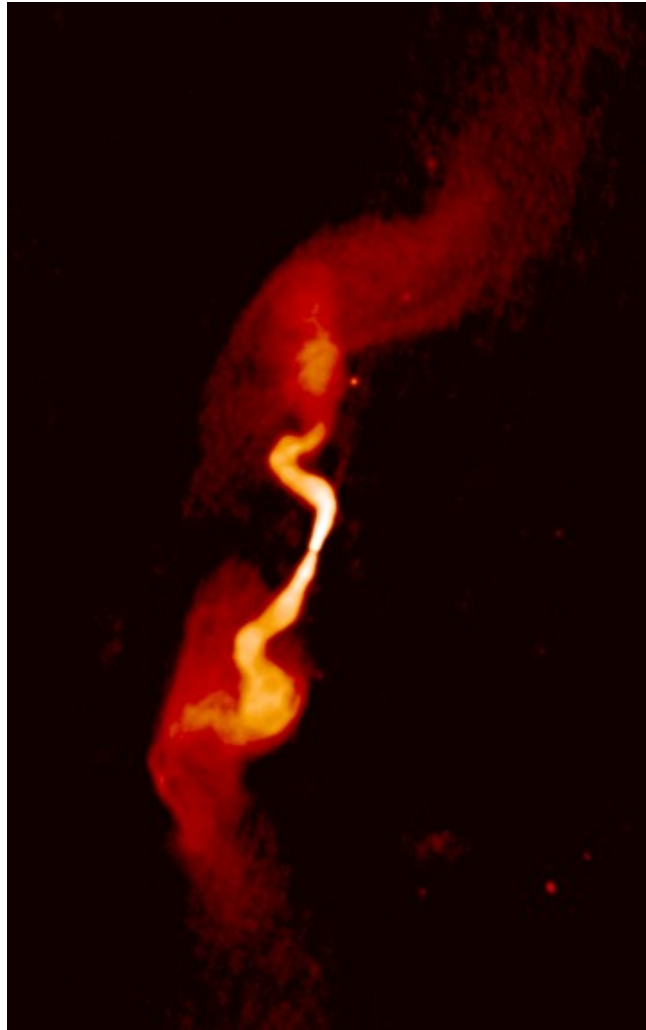


Figure 1.4: Images obtained with the Very Large Array (VLA) of jets in a FR I source 3C31 at the radio freq. 1.4 GHz and 8.4 GHz. (Credit: NRAO/AUI by R. Laing, A. Bridle, R. Perley, L. Feretti, G. Giovannini, and P. Parma (Laing 1996))

1.4.4 Magnetized disc: A Brief Review

As discussed earlier, the accretion discs are important because the only observational evidence of black holes that one can get is its radiation and accretion is the main source which fuels this. An accretion flow is Transonic and has shocks which is due to tug of war between centrifugal force and gravitational force. The puffed up post-shock region or CENBOL acts as a region for which a part of the inflowing matter ejected as an outflow and when it is collimated and accelerated, it gives rise to relativistic jets of which many observations were made. However, a clear understanding of formation, acceleration, and collimation of these jets has been eluding the astrophysicists. Historically, the theoretical approach to study the collimation and acceleration started with the study of thin as well as geometrically thick discs as it was believed that the origin of bipolar jets is somehow related to the properties and geometry of the accretion discs. Along with the viscosity, outflows and jets can also transport angular momentum from the disc very efficiently and thus helping the accretion process and since various properties of outflow heavily rely upon the properties of disc, theoretical as well as numerical disc model must produce disc and jet simultaneously. Several theoretical models (Blandford & Payne 1982, Chakrabarti & Bhaskaran 1992, Camenzind 1989), Heyvaerts & Norman 1989), Lovelace 1976, Königl 1989) etc.) in the context of thin disc it was shown that the hydromagnetic processes are crucial in explaining collimation and acceleration of outflows/jets. However, there are no satisfactory numerical work that can successfully produce collimated and accelerated outflows/jets originating from a magnetized disc although separate simulations of magnetized discs and jets exist. Blandford & Payne (1982) considered an infinitesimally thin, cold, Keplerian disc from which centrifugally driven, self-similar MHD wind originates provided the poloidal component of the magnetic field makes an angle less than 60° with the disc surface. At large distance from the disc the toroidal component becomes dominant and collimates the outflow creating a bipolar jet coming out of the disc perpendicularly. Contopoulos & Lovelace (1994) assume a power-law distribution of magnetic field in case of a self-similar, infinitesimally thin Keplerian disc and show that asymptotically collimated jets can be obtained for a particular set of power indices. Königl (1989) numerically determined the radially self-similar solutions for the magnetic field configuration inside a cold, partially ionized Keplerian disc and also showed that for certain set of disc parameters, Blandford-Payne type winds can be produced that attain super-Alfvénic velocity and can be magnetically collimated at a finite distance from the disc surface. Chakrabarti & Bhaskaran (1992) provided a more

general solution of the field. They solved for the field outside and the inside the disc as well, simultaneously and showed that a well collimated bipolar outflows and radio jets are possible to achieve in a self-consistent manner from magnetized protostellar disc and active galactic nuclei. Similar to previous works of Blandford & Payne and Königl they also considered the field to be self-similar in radial direction but functional form of field inside and outside the disc is different. Instead of considering a Keplerian disc, they assume a disc with an angular momentum distribution assumed to be a power-law function of the radial distance. They analytically solve the complete set of Euler-Maxwell equation. In their work they showed that there exists a complete set of solution for magnetized disc which allows an accelerated and collimated outflow to form. Another genre of magnetized disc solutions are present in the literature where the background flow is assumed to be the standard Keplerian disks and the magnetic field is assumed to be sheared and advected by the flow (Khanna & Camenzind, 1992; Lovelace et al. 1987; Wang et al. 1990). In those works, it can be seen that for sufficient supply of magnetic flux to the disc, the fine structure close to the disc surface can become Blandford-Payne type and be able to, in principle, launch cosmic jets. The gravitomagnetic potential of a rotating black hole in presence of a differentially rotating disk is seen to drive a self-excited dynamo and amplify weak (even axisymmetric) magnetic field to a higher field strength (Khanna & Camenzind 1994). A large body of literature is present that explores many aspects of the effects of buoyancy and shear amplification on these magnetic flux in the paradigm of thin accretion disc (e.g., Eardley & Lightman 1975, Galeev et al. 1979, Coroniti 1981, Shibata et al. 1990, Chakrabarti et al. 1994). All the works discussed above are in the context of thin accretion disc or standard Keplerian disc. In a magnetized thick accretion disc, due to resultant effects of magnetic tension and buoyancy, toroidal flux tubes are ejected from different parts of the disc creating a magnetically active region. This can, in principle, launch collimated jets. General idea of thick disc has already been discussed in the previous section. Thick accretion discs have a vortex like opening due to strong centrifugal force near the black hole (Lynden-Bell, 1978) on the either sides of the disc and the anisotropic radiation field at that region could be sufficiently strong to launch radio jets. However, in case of rapid variabilities found in blazars in optical regime (Miller 1988; Miller, Carini, Goodrich 1989; Wagner et al. 1990; Carini et al. 1992; Noble 1995; Noble & Miller 1996; Kidger & de Diego 1992) and in AGNs in X-Ray band (Treves et al. 1982; McHardy & Czerny 1987; Lawrence et al. 1987; Abraham & McHardy 1989) plausible explanation involves relativistic shock in-jet models

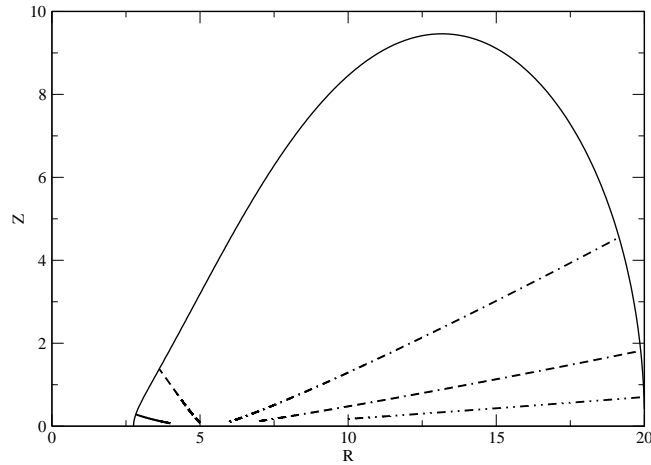


Figure 1.5: Trajectories of toroidal flux tubes released at the positions $R = 4, 5, 6, 8, 10 r_g$ drawn on the $R - z$ plane. This figure is drawn for $n = 0$ i.e. for constant angular momentum. This figure is reproduced using the parameters from Chakrabarti & D'Silva, 1994.

(Blandford & Königl, 1979; Hughes, Aller, & Aller 1985, 1989; Marscher & Gear, 1985; Marscher, Gear & Travis, 1992; Türler, Courvoisier, & Paltani 1999, 2000; Aller, Aller, & Hughes, 2003; Vlahakis & Königl, 2004; Camenzind, 2005) which require magnetic activity at the base of the jet. A thorough analytical study of the behavior of toroidal magnetic flux tubes in the backdrop of thick accretion discs has been studied by Chakrabarti & D'Silva (1994a, hereafter CD94) and D'Silva & Chakrabarti (1994b, hereafter, DC94) which also ensures the "chimney" like opening of the disc to be a magnetically active region. They showed that depending upon various flows and field parameters, such as, initial position of release, cross-sectional radius of the flux tubes, angular momentum distribution, etc. flux rings injected into thick disc will emerge into the "chimney" (funnel like opening at the inner part of the disc). The disc thermodynamic parameters were time independent while flux tube is allowed to be advected in with a suitably chosen radial flow. The magnetic field is expected to be brought along with the in-falling matter and are expected to be sheared to form mainly toroidal flux tubes in the disc. Due to the joint effects of drag, Coriolis force, magnetic tensions, buoyancy force a significant fraction of these fields are found to be emerging in the funnel whereas the remaining fraction would be expelled from the outer parts of the disc. It was shown that (1) if the disc is sufficiently hot ($T_p > 4 \times 10^{10} K$), the magnetic tension dominates over all other effects and the tube collapses catastrophically towards

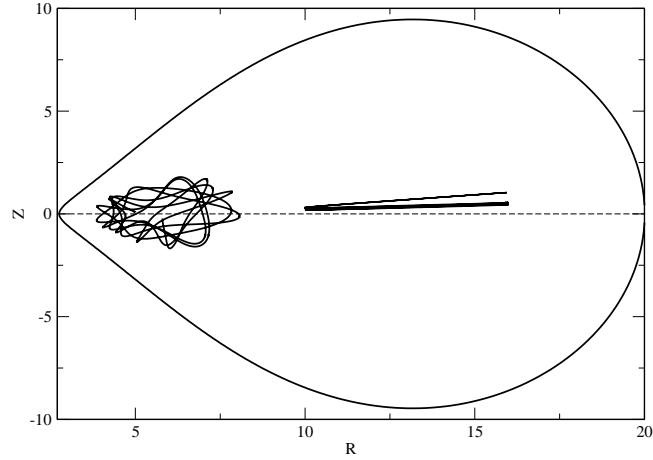


Figure 1.6: Trajectories of toroidal flux tubes released at the positions $R = 5, 10 r_g$ drawn on the $R - z$ plane. This figure is drawn for $n = 0$ i.e. for constant angular momentum. This figure is reproduced using the parameters from D'Silva & Chakrabarti, 1994.

the axis and thus squeezing out matter in the disc along the axis of the black hole in the process to form radio jets. (2) Formation of coronal structure is possible since this require ability to anchor the flux tubes inside the disc and because flux tubes can oscillate inside the disc with proper entropy condition, the disc can have an internal structure similar to the solar interior. If the entropy condition is proper, the coronae would form, otherwise it would come out of the disk as a whole without causing any flare. In the former case, there would be sporadic flaring events on the disc surface, whereas in the latter case, the collapse of fields in the funnel would cause destruction of the inner part of the disk and formation of blobby radio jets. Detailed observation of GRS1915+105 shows these features (Mirabel & Rodriguez 1994, Nandi et al. 2001). These processes could also be responsible for the formation of jets in active galaxies.

Chapter 2

Governing equations and Computational scheme

In this present Chapter, the equations that govern the dynamics of flow around a black hole are discussed. The numerical methodology and schemes to solve these equations are discussed as well. In case of an accretion disc, matter coming from the binary companion is essentially ionized plasma consisting of electrons and ions at the vicinity of a black hole. Generally it is assumed that an accretion flow onto a compact object is hydrodynamic in nature. The fluid approximation holds if the characteristic length scale of the system which are being studied, is much larger than the collision length. Furthermore, the characteristic time scale over which the dynamics is studied is much larger than the collision time. The self-gravity of the flow and any change in the mass of the central object is not considered. Owing to its fluid nature, the dynamics of the accreting matter is governed by Navier-Stokes equation. In the following sections the implementation of the hydrodynamic equations are discussed in details.

2.1 Hydrodynamic flow equation

The Navier-Stokes equation is comprised of three conservation laws, namely, (i) mass conservation law, (ii) momentum conservation law, and (iii) energy conservation law. The mass conservation law is known as the continuity equation. Similarly, momentum conservation law yields momentum equation and energy equation yields energy conservation law. The three equations are (Landau & Lifshitz, 1959),

$$\frac{\partial \rho}{\partial t} + \vec{\nabla} \cdot (\rho \vec{v}) = 0 \quad (2-1)$$

$$\rho \frac{\partial \vec{v}}{\partial t} + \rho \vec{v} \cdot \vec{\nabla} \vec{v} = -\vec{\nabla} P + \vec{F}_{ext} \quad (2-2)$$

$$\frac{\partial}{\partial t} \left(\frac{1}{2} \rho v^2 + \rho \epsilon \right) + \vec{\nabla} \cdot \left[\left(\frac{1}{2} \rho v^2 + \rho \epsilon + P \right) \cdot \vec{v} \right] = \vec{F} \cdot \vec{v} - \vec{\nabla} \cdot \vec{F}_{rad} - \vec{\nabla} \cdot \vec{q} \quad (2-3)$$

Equations 2.1, 2.2, and 2.3 are continuity, momentum density, and energy density equation respectively. In equation 2.2, P is the gas pressure and \vec{F} is the external force which includes gravitational force, viscosity, body forces such as electromagnetic forces etc. For viscous flow the effect of viscosity is manifested through the viscous stress tensor. The terms, ρv^2 and $\rho \epsilon$ in the eq. 2.3 are the measures of kinetic energy and internal energy density. \vec{F}_{rad} is the radiative flux vector and \vec{q} is conductive heat flux. Alongwith these conservation equations, in the absence of an energy equation, one needs an equation of state to describe the astrophysical flows completely. For this purpose, the ideal gas equation is given as,

$$P = \frac{\rho k T}{\mu m_p} \quad (2-4)$$

where, k is the Boltzmann constant, T is the temperature, m_p is the mass of hydrogen atom and μ is the mean molecular weight for neutral hydrogen, $\mu = 1$ and for fully ionized hydrogen, $\mu = \frac{1}{2}$.

2.2 equations for inviscid flow

Equations governing inviscid flow can be obtained from the Navier-Stokes equations by imposing some constraints. Since the flow is inviscid, no contribution from viscous stress tensor will be there and also heat flux vector is ignored (Landau & Lifshitz, 1959). Equation 2.1 remains the same. Equation 2.2 is modified to,

$$\rho \frac{\partial \vec{v}}{\partial t} + \rho \vec{v} \cdot \vec{\nabla} \vec{v} = -\vec{\nabla} P + \vec{F}_g \quad (2-5)$$

and also the energy equation (eq. 2.3) is changed to

$$\frac{\partial}{\partial t} \left(\frac{1}{2} \rho v^2 + \rho \epsilon \right) + \vec{\nabla} \cdot \left[\left(\frac{1}{2} \rho v^2 + \rho \epsilon + P \right) \cdot \vec{v} \right] = \vec{F}_g \cdot \vec{v} \quad (2-6)$$

since no radiative cooling was considered, \vec{F}_{rad} is ignored. \vec{F}_g is the gravitational force term which is given as,

$$\vec{F}_g = F_{gr}\hat{r} + F_{gz}\hat{z} \quad (2-7)$$

where,

$$F_{gr} = -\rho \frac{1}{2(\sqrt{r^2 + z^2} - 1)^2} \frac{r}{\sqrt{r^2 + z^2}}, \quad (2-8)$$

$$F_{gz} = -\rho \frac{1}{2(\sqrt{r^2 + z^2} - 1)^2} \frac{z}{\sqrt{r^2 + z^2}}. \quad (2-9)$$

Here, pseudo-Newtonian type potential is used which has the form of $\frac{1}{2(R-1)}$ where, $R = \sqrt{r^2 + z^2}$ (Paczynski & Wiita, 1980). Here, cylindrical co-ordinate system is used. The equation of state used here can be derived from the ideal gas equation using expression of internal energy and it takes the form,

$$\epsilon = \frac{P/\rho}{\gamma - 1} \quad (2-10)$$

where, P is the gas pressure and ϵ is the internal energy. It is convenient to write the set of hydrodynamical equations in terms of conserved variable such as density (ρ), momentum ($\rho\vec{v}$, and energy (E). Hence we simply rearrange the equations 2.2, and 2.3 (Ryu et al 1995; Molteni, Ryu, Chakrabarti 1996 [MRC98]). From eq 2.2 using cylindrical coordinate system and writing component wise we get,

$$\rho \frac{\partial v_r}{\partial t} + \rho v_r \frac{\partial v_r}{\partial r} + \rho v_z \frac{\partial v_r}{\partial z} + \frac{\partial P}{\partial r} = -\frac{\rho v_\theta^2}{r} - \frac{\rho r}{2(\sqrt{r^2 + z^2} - 1)^2 \sqrt{r^2 + z^2}} \quad (2-11)$$

$$\rho \frac{\partial v_\theta}{\partial t} + \rho v_r \frac{\partial v_\theta}{\partial r} + \rho v_z \frac{\partial v_\theta}{\partial z} + = -\frac{\rho v_r v_\theta}{r} \quad (2-12)$$

$$\rho \frac{\partial v_z}{\partial t} + \rho v_r \frac{\partial v_z}{\partial r} + \rho v_z \frac{\partial v_z}{\partial z} + \frac{\partial P}{\partial r} = -\frac{\rho z}{2(\sqrt{r^2 + z^2} - 1)^2 \sqrt{r^2 + z^2}} \quad (2-13)$$

Now in order to write in terms of conservative variable from eq. 2.11 and using $\rho v_r \frac{\partial v_r}{\partial r} = \frac{r \rho v_r}{r} \frac{\partial v_r}{\partial r} = \frac{1}{r} \frac{\partial}{\partial r} (r \rho v_r^2) - v_r \frac{1}{r} \frac{\partial}{\partial r} (r \rho v_r^2)$ and $\rho v_z \frac{\partial v_z}{\partial z} = \frac{\partial}{\partial z} (\rho v_r v_z) - v_r \frac{\partial}{\partial z} (\rho v_z)$ and also using eq. 2.1 we have,

$$\frac{\partial(\rho v_r)}{\partial t} + \frac{1}{r} \frac{\partial(r\rho v_r^2)}{\partial r} + \frac{\partial P}{\partial r} + \frac{\partial(\rho v_r v_z)}{\partial z} = -\frac{\rho v_\theta^2}{r} - \frac{\rho r}{2(\sqrt{r^2 + z^2} - 1)^2 \sqrt{r^2 + z^2}} \quad (2-14)$$

Similarly eqs. 2.6, 2.12, and 2.13 can be rearranged and written in terms of conservative variable as,

$$\frac{\partial(\rho v_\theta)}{\partial t} + \frac{1}{r} \frac{\partial(r\rho v_\theta v_r)}{\partial r} + \frac{\partial(\rho v_\theta v_z)}{\partial z} = -\frac{\rho v_\theta v_r}{r} \quad (2-15)$$

$$\frac{\partial(\rho v_z)}{\partial t} + \frac{1}{r} \frac{\partial(r\rho v_z v_r)}{\partial r} + \frac{\partial(\rho v_z^2 + P)}{\partial z} = -\frac{\rho z}{2(\sqrt{r^2 + z^2} - 1)^2 \sqrt{r^2 + z^2}} \quad (2-16)$$

$$\frac{\partial E}{\partial t} + \frac{1}{r} \frac{\partial(r(E + P)v_r)}{\partial r} + \frac{\partial[(E + P)v_z]}{\partial z} = -\frac{\rho(rv_r + zv_z)}{2(\sqrt{r^2 + z^2} - 1)^2 \sqrt{r^2 + z^2}} \quad (2-17)$$

where, $E = \frac{1}{2}\rho v^2 + \rho\epsilon$. Above mentioned four equations eq. 2.14 - 2.17 can be written in a compact form:

$$\frac{\partial \mathbf{q}}{\partial t} + \frac{1}{r} \frac{\partial(r\mathbf{F}_1)}{\partial r} + \frac{\partial \mathbf{F}_2}{\partial r} + \frac{\partial \mathbf{G}}{\partial z} = \mathbf{S} \quad (2-18)$$

where, \mathbf{q} is the state vector, \mathbf{F}_1 , \mathbf{F}_2 , \mathbf{G} are flux vectors and \mathbf{S} is called the source term. Expressions for the state vector, flux vectors and source term are given as,

$$\mathbf{q} = \begin{pmatrix} \rho \\ \rho v_r \\ \rho v_\theta \\ \rho v_z \\ E \end{pmatrix},$$

$$\mathbf{F}_1 = \begin{pmatrix} \rho v_r \\ \rho v_r^2 \\ \rho v_\theta v_r \\ \rho v_z v_r \\ (E + p)v_r \end{pmatrix}, \quad \mathbf{F}_2 = \begin{pmatrix} 0 \\ p \\ 0 \\ 0 \\ 0 \end{pmatrix}, \quad \mathbf{G} = \begin{pmatrix} \rho v_z \\ \rho v_r v_z \\ \rho v_\theta v_z \\ \rho v_z^2 + p \\ (E + p)v_z \end{pmatrix},$$

$$\mathbf{S} = \begin{pmatrix} 0 \\ \frac{\rho v_\theta^2}{r} - \frac{\rho r}{2(\sqrt{r^2+z^2}-1)^2 \sqrt{r^2+z^2}} \\ -\frac{\rho v_r v_\theta}{r} \\ -\frac{\rho z}{2(\sqrt{r^2+z^2}-1)^2 \sqrt{r^2+z^2}} \\ -\frac{\rho(rv_r+zv_z)}{2(\sqrt{r^2+z^2}-1)^2 \sqrt{r^2+z^2}} \end{pmatrix}. \quad (2-19)$$

We solve this set of hyperbolic partial differential equations numerically and detail discussion on the numerical schemes and procedure is discussed in the next section.

2.3 Numerical procedure

In order to solve the fluid dynamics equations mentioned in the earlier section we have chosen the finite difference method. The basic idea of finite difference method is that the derivatives in the differential equations are written in terms of discrete quantities of dependent and independent variable and thus generating a set of simultaneous algebraic equations with all the unknowns defined at discrete grid points. We will briefly discuss the basics of the method here.

2.3.1 Finite Difference Method

To illustrate what we started discussing at the start of this section, let us consider a simple form of a hyperbolic PDE (Chung 2002, Balsara 2013) which is same as the compact form of the Euler's equation written in eq. 2.18.

$$\frac{\partial \mathbf{U}}{\partial t} + \frac{\partial \mathbf{F}}{\partial x} = 0 \quad (2-20)$$

Using finite difference method we can discretise the differential equation as given below,

$$\frac{u_i^{n+1} - u_i^n}{\Delta t} + \frac{F^n_{i+\frac{1}{2}} - F^n_{i-\frac{1}{2}}}{\Delta x} = 0 \quad (2-21)$$

where Δx is the grid size and Δt is the timestep. We shall discuss in the subsequent section how these two should be chosen in case of a hydrodynamical problem. Now, in case of Euler's equation describing the inviscid flow a finite set of discretized value of density and velocity is defined over a mesh of size $N \times N$.

2.3.2 Construction of Flux Jacobians

Let us first consider a general system of conservation laws in formal notation,

$$\mathbf{U}_t + \mathbf{F}(\mathbf{U})_x + \mathbf{G}(\mathbf{U})_y = \mathbf{S}(\mathbf{U}) \quad (2-22)$$

where, \mathbf{U} is the vector of conserved variables and \mathbf{F} & \mathbf{G} are the flux vectors and \mathbf{S} is the vector representing the source term. For any such system we can always derive characteristic matrices and write eq. 2.21 involving them as,

$$\mathbf{U}_t + \mathbf{A}(\mathbf{U})\mathbf{U}_x + \mathbf{B}(\mathbf{U})\mathbf{U}_y = \mathbf{S}(\mathbf{U}) \quad (2-23)$$

With $\mathbf{A}(\mathbf{U}) = \frac{\partial \mathbf{F}(\mathbf{U})}{\partial \mathbf{U}}$ and $\mathbf{B}(\mathbf{U}) = \frac{\partial \mathbf{G}(\mathbf{U})}{\partial \mathbf{U}}$. There exists another set of variables " \mathbf{V} " called primitive variables which help to simplify the system of PDEs. There is an invertible Jacobian matrix $\frac{\partial \mathbf{U}}{\partial \mathbf{V}}$ which gives a relation between any fluctuation in conservative variable (\mathbf{U}) and any fluctuation in primitive variable (\mathbf{V}).

2.3.3 Computation of eigenvalues and eigenvectors

In previous sub-section we have discussed the idea of generalized flux Jacobian using which one can simply write the system of hyperbolic conservation laws in terms of primitive variables. The eigenvalues of the characteristic matrices can be written in an ordered sequential manner as (For detailed discussion see Chung 2002, Balsara 2013),

$$\lambda_1 \leq \lambda_2 \leq \dots \leq \lambda_m \quad (2-24)$$

Associated with m eigenvalues, λ_i with $i = 1, \dots, m$, we can define right and left eigenvectors as,

$$\mathbf{A}\mathbf{r}_i = \lambda_i\mathbf{r}_i; \quad \mathbf{l}_i\mathbf{A} = \lambda_i\mathbf{l}_i \quad (2-25)$$

The eigenvectors can be arranged in such a way so that we can write a matrix \mathbf{R} whose i^{th} column is \mathbf{r}_i . Similarly, we can obtain a matrix for left eigenvectors \mathbf{L} as well. We have $\mathbf{L}\mathbf{R} = \mathbf{I}$ as left and right eigenvectors are orthonormal. Defining a diagonal matrix $\mathbf{\Lambda} = \text{diag} \{ \lambda_1, \lambda_2, \dots, \lambda_m \}$ we can write,

$$\mathbf{L}\mathbf{A}\mathbf{R} = \mathbf{\Lambda} \quad \text{or} \quad \mathbf{A} = \mathbf{R}\mathbf{\Lambda}\mathbf{L} \quad (2-26)$$

From eqn. 2.22 ignoring the source term we get a system of m equations involving a scalar variable called characteristic variable or eigenweight. The system of equations is given by,

$$\partial_t w_i + \lambda_i \partial_x w_i + \beta_i \partial_y w_i = 0 \quad (2-27)$$

This equation yields a wave like solution for both continuous and discontinuous initial data where initial profile for each characteristic field is advected with appropriate wave speed giving rise to a m number of simple waves. With this we next stumble upon the Riemann problem. In next subsection we shall see the application of these aforementioned procedure to Euler equation.

2.3.4 Euler equation

We first consider the compact vector form of Euler equation written in eqn. 2.18 and rewrite the flux functions as (Ryu et al. 1993, Chung 2002),

$$\mathbf{F}(\mathbf{U}) = \mathbf{F}(\mathbf{q}) = \mathbf{F}_1(\mathbf{q}) + \mathbf{F}_2(\mathbf{q}); \quad \mathbf{G}(\mathbf{U}) = \mathbf{G}(\mathbf{q}) \quad (2-28)$$

and their corresponding Jacobian matrices are $\mathbf{A}(\mathbf{q}) = \frac{\partial \mathbf{F}(\mathbf{q})}{\partial \mathbf{q}}$ and $\mathbf{B}(\mathbf{q}) = \frac{\partial \mathbf{G}(\mathbf{q})}{\partial \mathbf{q}}$. We can easily obtain their eigenvalues using the method described in 2.3.2 and 2.3.3. The eigenvalues of $\mathbf{A}(\mathbf{q})$ are given as,

$$\lambda_1 = v_r - c_s, \quad \lambda_2 = v_r, \quad \lambda_3 = v_r, \quad \lambda_4 = v_r, \quad \lambda_5 = v_r + c_s \quad (2-29)$$

and eigenvalues of $\mathbf{B}(\mathbf{q})$ can be obtained by proper permutation of the indices. The corresponding right eigenvectors are,

$$\mathbf{R}_1 = \begin{pmatrix} 1 \\ v_r - c_s \\ v_\theta \\ v_z \\ H - v_r c_s \end{pmatrix}$$

$$\mathbf{R}_2 = \begin{pmatrix} 0 \\ 0 \\ 1 \\ 0 \\ v_\theta \end{pmatrix}$$

$$\mathbf{R}_3 = \begin{pmatrix} 1 \\ v_r \\ v_\theta \\ v_z \\ \Theta/2 \end{pmatrix}$$

$$\mathbf{R}_4 = \begin{pmatrix} 0 \\ 0 \\ 0 \\ 1 \\ v_z \end{pmatrix}$$

$$\mathbf{R}_5 = \begin{pmatrix} 1 \\ v_r + c_s \\ v_\theta \\ v_z \\ H + v_r c_s \end{pmatrix} \quad (2-30)$$

where, $H = (E + P)/\rho$ is enthalpy and $\Theta = (v_r^2 + v_\theta^2 + v_z^2)/2$. The orthonormal set of left eigenvectors are given as,

$$\mathbf{L}_1 = \begin{pmatrix} \frac{(\gamma - 1)\Theta/2 + c_s v_r}{2c_s^2} & -\frac{(\gamma - 1)v_r + c_s}{2c_s^2} & -\frac{(\gamma - 1)v_\theta}{2c_s^2} & -\frac{(\gamma - 1)v_z}{2c_s^2} \\ \frac{\gamma - 1}{2c_s^2} \end{pmatrix} \quad (2-31)$$

$$\begin{aligned} \mathbf{L}_2 &= \begin{pmatrix} -v_\theta & 0 & 1 & 0 & 0 \end{pmatrix} \\ \mathbf{L}_3 &= \begin{pmatrix} 1 - \frac{(\gamma - 1)\Theta}{2c_s^2} & \frac{(\gamma - 1)v_r}{c_s^2} & \frac{(\gamma - 1)v_\theta}{c_s^2} & \frac{(\gamma - 1)v_z}{c_s^2} & -\frac{\gamma - 1}{c_s^2} \end{pmatrix} \\ \mathbf{L}_4 &= \begin{pmatrix} -v_z & 0 & 0 & 1 & 0 \end{pmatrix} \\ \mathbf{L}_5 &= \begin{pmatrix} \frac{(\gamma - 1)\Theta/2 - c_s v_r}{2c_s^2} & -\frac{(\gamma - 1)v_r - c_s}{2c_s^2} & -\frac{(\gamma - 1)v_\theta}{2c_s^2} & -\frac{(\gamma - 1)v_z}{2c_s^2} \\ \frac{\gamma - 1}{2c_s^2} \end{pmatrix} \end{aligned} \quad (2-32)$$

The details of the numerical method to solve the eigensystem is given in the following section. For this purpose, we have used a Eulerian grid-based finite difference method known as the Total Variation Diminishing (TVD) method.

2.3.5 Total Variation Diminishing scheme

The Navier-Stokes equations as well as the Euler equation can be solved numerically using first order upwind scheme accurately and central schemes may also be used but they come with a drawback of creating excessive damping and also shock discontinuities may not be well resolved in that case. This trend can be compensated using upwind schemes but first order upwind scheme may cause an occurrence of undershoots and overshoots at the discontinuity. A remedy is provided through low or high resolution second order upwind scheme. All these schemes employ finite difference method to solve the PDE system.

Harten (1983) came up with a second order high resolution upwind scheme to solve hyperbolic PDE systems which involves a process called Total Variation Non Increasing (TVNI) coined by Harten himself and later it was changed to Total Variation Diminishing (TVD) Scheme by other researchers. The crux of the scheme is as follows. In systems described by PDEs, such as the one dimensional advection equation described by a hyperbolic PDE as (Chung 2002),

$$\frac{\partial u}{\partial t} + a \frac{\partial u}{\partial x} = 0 \quad (2-33)$$

the total variation (TV) is given as,

$$TV = \int \left| \frac{\partial u}{\partial x} \right| dx \quad (2-34)$$

and if written in discretized manner it will be given as,

$$TV = \sum |u^{n+1} - u^n| \quad (2-35)$$

A numerical scheme will be called TVD if it exhibits following property,

$$TV^{n+1} \leq TV^n \quad (2-36)$$

where, n signifies the time in the time iteration. The TVD property ensures that the total variation given at a timestep is restricted by the initial and boundary value. It is an explicit second order accurate upwind scheme which is capable of solving hyperbolic PDE system which is analogous to the Navier-Stokes or Euler equation. This nonlinear scheme first employs a modification to the flux functions and then use non-oscillatory first order accurate scheme to achieve second order accurate solution.

Procedure of TVD

In this section we discuss about the non-linear second order accurate TVD scheme in brief. The building block of this scheme is a first order monotonic upwind scheme which gives us the first order fluxes ($F^{*,t}_{i+1/2}$) at the i^{th} cell boundary and modifying it with second order corrections we get second order fluxes ($F^t_{i+1/2}$) at the i^{th} cell boundary. We can define two second order flux corrections using cell centered fluxes from the adjacent cells depending on the sign of the advection velocity. Thus we have (Ryu et al. 1993, Giri 2014, Harten 1983, Chung 2002),

$$\Delta F^{L,t}_{i+1/2} = \frac{F^t_i - F^t_{i-1}}{2}; \quad \Delta F^{R,t}_{i+1/2} = \frac{F^t_{i+1} - F^t_i}{2} \quad (2-37)$$

when advection velocity is positive and when it is negative we have,

$$\Delta F^{L,t}_{i+1/2} = -\frac{F^t_{i+1} - F^t_i}{2}; \quad \Delta F^{R,t}_{i+1/2} = -\frac{F^t_{i+2} - F^t_{i+1}}{2} \quad (2-38)$$

A flux limiter is used to determine the appropriate second order corrections,

$$\Delta F_{i+1/2}^t = \phi \left(\Delta F_{i+1/2}^{L,t}, \Delta F_{i+1/2}^{R,t} \right) \quad (2-39)$$

which still obeys the TVD condition. The second order flux corrections are then added to the first order fluxes to obtain the second order fluxes. Now, the time updation is done using a second order Runge-Kutta scheme where first we do a half time step updation given as,

$$u^{t+\Delta t/2}_i = u^t_i - \left(\frac{F_{i+1/2}^t - F_{i-1/2}^t}{\Delta x} \right) \frac{\Delta t}{2} \quad (2-40)$$

and then a full step time updation is computed as

$$u^{t+\Delta t}_i = u^t_i - \left(\frac{F_{i+1/2}^{t+\Delta t/2} - F_{i-1/2}^{t+\Delta t/2}}{\Delta x} \right) \Delta t \quad (2-41)$$

Roe's Approximate Riemann Solver:

Instead of dealing with non-linear problem, Roe's approximate Riemann solver (Roe, 1981) tackles a linearized version of the problem. In TVD scheme which is an Eulerian grid based procedure the fluxes are defined at the grid boundary while the physical quantities such as density, velocity, energy etc. are defined at the grid centre. Hence we use Roe's approximation to obtain an average value of the physical quantities at the grid boundary. Therefore, we have (Ryu 1993, Roe 1981),

$$v_{r,i+1/2} = \frac{\sqrt{\rho_i} v_{r,i} + \sqrt{\rho_{i+1}} v_{r,i+1}}{\sqrt{\rho_i} + \sqrt{\rho_{i+1}}} \quad (2-42)$$

$$v_{\theta,i+1/2} = \frac{\sqrt{\rho_i} v_{\theta,i} + \sqrt{\rho_{i+1}} v_{\theta,i+1}}{\sqrt{\rho_i} + \sqrt{\rho_{i+1}}} \quad (2-43)$$

$$v_{z,i+1/2} = \frac{\sqrt{\rho_i} v_{z,i} + \sqrt{\rho_{i+1}} v_{z,i+1}}{\sqrt{\rho_i} + \sqrt{\rho_{i+1}}} \quad (2-44)$$

$$H_{i+1/2} = \frac{\sqrt{\rho_i} H_i + \sqrt{\rho_{i+1}} H_{i+1}}{\sqrt{\rho_i} + \sqrt{\rho_{i+1}}} \quad (2-45)$$

$$a_{i+1/2} = \left[(\gamma - 1) \left\{ H_{i+1/2} - \frac{1}{2} \left(v_{r,i+1}^2 + v_{\theta,i+1}^2 + v_{z,i+1}^2 \right) \right\} \right]^{\frac{1}{2}} \quad (2-46)$$

2.3.6 grid size and time step

Since the numerical scheme discussed here employs finite difference method, we need a grid based system to implement the scheme. Now, to realize the difference equation using finite difference we need grid size. If this grid size or grid length is too coarse it would give spurious result and too fine grid would result in large truncation errors in the difference equation. Thus, choosing right grid size is important. The time step is calculated using Courant condition given as,

$$\Delta t \leq \frac{\Delta x}{c_s + |v|} \quad (2-47)$$

which is to be satisfied everywhere.

2.4 viscous flow

In order to study effects of energy dissipation, occurring during the motion of the flow, on that motion itself we must look into thermodynamic irreversibility of the motion and one of the reason behind this is internal friction or viscosity. In case of Euler equations the momentum flux represents a completely reversible process but in presence of viscosity an irreversible transfer of momentum takes place from points with higher velocity to the lower. Hence an extra term must be added to take into account of irreversible viscous transfer and the resulting momentum flux density tensor yields (Giri, Chakrabarti 2012, Giri 2014)

$$\sigma_{ik} = \tau_{ik} - p\delta_{ik} \quad (2-48)$$

which is called stress tensor and τ_{ik} is called the viscous stress tensor. The most general form of this viscous stress tensor is given by (Landau & Lifshitz 1959),

$$\tau_{ik} = \eta \left(\frac{\partial v_i}{\partial x_k} + \frac{\partial v_k}{\partial x_i} - \frac{2}{3} \delta_{ik} \frac{\partial v_l}{\partial x_l} \right) + \zeta \delta_{ik} \frac{\partial v_l}{\partial x_l} \quad (2-49)$$

Using this and also considering the viscosity coefficients to be constant throughout the fluid we can have the Navier stokes equation for incompressible fluid where contribution from viscous stress is given as,

$$\rho \frac{\partial \vec{v}}{\partial t} + \rho \vec{v} \cdot \vec{\nabla} \vec{v} = -\vec{\nabla} P + \vec{F}_b + \vec{\nabla} \tau. \quad (2-50)$$

Here $\boldsymbol{\sigma}$ is the viscous stress having six mutually independent components. In cylindrical coordinates the components of the velocity vector given by $\vec{v} = (v_r, v_\theta, v_z)$. The six independent components of the viscous stress tensor (Landau & Lifshitz 1959) are listed here in cylindrical coordinates, $\tau_{rr}, \tau_{r\theta}, \tau_{rz}, \tau_{\theta\theta}, \tau_{\theta z}$ & τ_{zz} . Since the flow is incompressible hence the viscous stress tensor becomes,

$$\tau_{ik} = \eta \left(\frac{\partial v_i}{\partial x_k} + \frac{\partial v_k}{\partial x_i} \right) \quad (2-51)$$

If we split all the viscous stress tensor, three components of equation 2.53 takes the following forms (Landau & Lifshitz 1959 and Acheson 1990). The v_r component of Navier-Stokes equation is given by

$$\begin{aligned} & \rho \left[\frac{\partial v_r}{\partial t} + v_r \frac{\partial v_r}{\partial r} + \frac{v_\theta^2}{r} + \frac{v_\theta}{r} \frac{\partial v_r}{\partial \theta} + v_z \frac{\partial v_r}{\partial z} \right] = \\ & -\frac{\partial P}{\partial r} + \eta \left[\frac{\partial^2 v_r}{\partial r^2} + \frac{1}{r} \frac{\partial v_r}{\partial r} - \frac{v_r}{r^2} + \frac{1}{r^2} \frac{\partial^2 v_r}{\partial \theta^2} + \frac{\partial^2 v_r}{\partial z^2} - \frac{2}{r^2} \frac{\partial v_\theta}{\partial \theta} \right] + F_r. \end{aligned} \quad (2-52)$$

Again, the v_θ component is given by

$$\begin{aligned} & \rho \left[\frac{\partial v_\theta}{\partial t} + v_r \frac{\partial v_\theta}{\partial r} + \frac{v_\theta v_r}{r} + \frac{v_\theta}{r} \frac{\partial v_\theta}{\partial \theta} + v_z \frac{\partial v_\theta}{\partial z} \right] = \\ & -\frac{1}{r} \frac{\partial P}{\partial \theta} + \eta \left[\frac{\partial^2 v_\theta}{\partial r^2} + \frac{1}{r} \frac{\partial v_\theta}{\partial r} - \frac{v_\theta}{r^2} + \frac{1}{r^2} \frac{\partial^2 v_\theta}{\partial \theta^2} + \frac{\partial^2 v_\theta}{\partial z^2} + \frac{2}{r^2} \frac{\partial v_\theta}{\partial \theta} \right] + F_\theta. \end{aligned} \quad (2-53)$$

Finally, the v_z component is given by

$$\begin{aligned} & \rho \left[\frac{\partial v_z}{\partial t} + v_r \frac{\partial v_z}{\partial r} + \frac{v_\theta}{r} \frac{\partial v_z}{\partial \theta} + v_z \frac{\partial v_z}{\partial z} \right] = \\ & -\frac{\partial P}{\partial z} + \eta \left[\frac{\partial^2 v_z}{\partial r^2} + \frac{1}{r} \frac{\partial v_z}{\partial r} + \frac{1}{r^2} \frac{\partial^2 v_z}{\partial \theta^2} + \frac{\partial^2 v_z}{\partial z^2} \right] + F_z, \end{aligned} \quad (2-54)$$

where, η is the dynamic viscosity defined by $\eta = \mu\rho$ and μ is called the kinematic viscosity. As we have chosen the axisymmetric case, we have neglected $\frac{\partial}{\partial \theta}$ added terms. So the above equations reduce as following.

Equation 2.55 reduces to

$$\begin{aligned} & \rho \left[\frac{\partial v_r}{\partial t} + v_r \frac{\partial v_r}{\partial r} + v_z \frac{\partial v_r}{\partial z} \right] = \\ & -\frac{\partial P}{\partial r} - \frac{v_\theta^2}{r} + \eta \left[\frac{\partial^2 v_r}{\partial r^2} + \frac{1}{r} \frac{\partial v_r}{\partial r} - \frac{v_r}{r^2} + \frac{\partial^2 v_r}{\partial z^2} \right] + F_{gr}. \end{aligned} \quad (2-55)$$

Equation 2.56 takes the form,

$$\begin{aligned} & \rho \left[\frac{\partial v_\theta}{\partial t} + v_r \frac{\partial v_\theta}{\partial r} + v_z \frac{\partial v_\theta}{\partial z} \right] = \\ & -\frac{v_\theta v_r}{r} + \eta \left[\frac{\partial^2 v_\theta}{\partial r^2} + \frac{1}{r} \frac{\partial v_\theta}{\partial r} - \frac{v_\theta}{r^2} + \frac{\partial^2 v_\theta}{\partial z^2} \right]. \end{aligned} \quad (2-56)$$

Equation 2.57 reduces to,

$$\begin{aligned} & \rho \left[\frac{\partial v_z}{\partial t} + v_r \frac{\partial v_z}{\partial r} + v_z \frac{\partial v_z}{\partial z} \right] = \\ & -\frac{\partial P}{\partial z} + \eta \left[\frac{\partial^2 v_z}{\partial r^2} + \frac{1}{r} \frac{\partial v_z}{\partial r} + \frac{\partial^2 v_z}{\partial z^2} \right] + F_{gz}. \end{aligned} \quad (2-57)$$

For a thin accretion flow, we can neglect all the components of stress tensor except the $\tau_{r\theta}$ component as the dominant contributor to the viscous stress tensor and only this component will contribute to transporting angular momentum along the radial direction. Hence the viscous term that will go into the hydrodynamic equation is given as,

$$\eta \left[\frac{\partial^2 v_\theta}{\partial r^2} + \frac{1}{r} \frac{\partial v_\theta}{\partial r} - \frac{v_\theta}{r^2} \right] = \frac{1}{r^2} \frac{\partial}{\partial r} (r^2 \tau_{r\theta}), \quad (2-58)$$

where,

$$\tau_{r\theta} = \eta r \frac{\partial \Omega}{\partial r}.$$

Here, Ω is angular velocity and defined as

$$\Omega = \frac{v_\theta}{r}.$$

In a binary system, matter flowing out of the companion star and falling onto the black hole possesses considerable amount of angular momentum relative to the black hole and this angular momentum prevents free fall of matter. Thus a mechanism to transport angular momentum is needed. It has long been conjectured that outward transport of matter in an accretion flow is driven by the

turbulence present in the fluid flow. Shakura & Sunyaev (1973) gave the α -prescription of viscosity which introduces a phenomenological shear stress to mimic the effect of turbulence. This shear stress is proportional to the total pressure and this shear stress enables the exchange of angular momentum between two neighboring layers of the fluid. Diffusion of randomly moving gas molecule across shearing interface also generate viscosity, known as molecular viscosity which is microscopic in nature but it is too small to explain timescales of the evolution of accretion disc. Thus it is evident that macroscopic turbulence plays a major role in generating viscosity. Winds and outflows also transport some angular momentum but it is not a dominating source. Using $SS\alpha$ prescription, we can assume $\tau_{r\theta} = -\alpha p$, where α is a proportionality factor which need not be constant throughout the flow. This has been used in the simulations by CM95 and C96. In Eq. 2.61 we put $-\alpha p$ in the place of $\tau_{r\theta}$. In that case, the viscous term reduces to

$$\frac{1}{r^2} \frac{\partial}{\partial r} (-r^2 \alpha p) = -\alpha \left(\frac{2p}{r} + \frac{\partial p}{\partial r} \right). \quad (2-59)$$

In case of thick accretion flow, all viscous stress could be significant in flow dynamics. Assuming that the flow is thick $h \sim r$, the α -prescription could be written as (e.g., Igumenshchev et al. 1996) as

$$\mu = \alpha_s \rho \frac{a^2}{\Omega_k}, \quad (2-60)$$

where, α_s is constant of order 1, a is the adiabatic sound speed, and

$$\Omega_k = \left[\frac{1}{r} \frac{\partial \Phi}{\partial r} \right]^{\frac{1}{2}}$$

is the Keplerian angular velocity. It is to be noted that the heat generated by the viscous dissipation is assumed to be radiated away instantly. In the literature, other viscosity prescriptions are also available such as, the prescription given by Macfayden & Woosley (1999) where it is stated that the α is constant when $v_\theta > v_r$ while it is assume to be scaled as v_θ/v_r in the preshock flow to reduce shear. The result of the simulation using this prescription remains the same. Thus a constant α plays a similar role to that in a Keplerian disc (Giri, Ph.D. thesis, 2014). Contribution from the viscous stress term goes into source term only.

2.5 Energy equation and cooling

For radiative cooling, ideally we ought to be using Comptonization but since the process is highly non-linear and non-local we may consider bremsstrahlung cooling instead which can be computed from the local density and temperature. However, this process is too weak to have any significant effect. Thus a power-law type cooling is chosen (Giri, Chakrabarti 2013) with temperature dependence as T^β . We have included this in the energy equation (eq. 2.17). The cooling rate is $\Lambda_{powcool} \propto \rho^2 T^\beta$, where, $\beta > 0$ is the cooling index. The energy equation becomes:

$$\frac{\partial(\rho\epsilon)}{\partial t} + \nabla \cdot (\rho\epsilon\mathbf{v}) + \Lambda_{powcool} = 0, \quad (2-61)$$

where, $\epsilon = \frac{p/\rho}{(\gamma-1)} + (v_r^2 + v_\theta^2 + v_z^2)/2 + \Phi_g$, is the specific energy, γ is the adiabatic index, ρ is the mass density. Here, Λ_{cool} is the expression for power-law cooling. So, the energy conservation equation given in eq. 2.17 becomes,

$$\frac{\partial E}{\partial t} + \frac{1}{r} \frac{\partial(E+p)rv_r}{\partial r} + \frac{\partial(E+p)v_z}{\partial z} = - \frac{\rho(rv_r + zv_z)}{2(\sqrt{r^2 + z^2} - 1)^2 \sqrt{r^2 + z^2}} - \Lambda_{powcool}. \quad (2-62)$$

Here, the energy density E (without the potential energy) is defined as, $E = p/(\gamma - 1) + \rho(v_r^2 + v_\theta^2 + v_z^2)/2$, ρ is the mass density, γ is the adiabatic index, p is the pressure, v_r , v_θ and v_z are the radial, azimuthal and vertical components of velocity respectively. The default power-law for bremsstrahlung cooling is obtained by taking cooling index $\beta = \frac{1}{2}$. In a hydrogen plasma which is essentially an electron-proton system, the expression for bremsstrahlung cooling process (Lang, 1980; Rybicki & Lightman 1979) is given as,

$$\Lambda_{brems} = 1.43 \times 10^{-27} N_e N_i T^{\frac{1}{2}} Z^2 g_f \text{ erg cm}^{-3} \text{ s}^{-1}, \quad (2-63)$$

where,

$$N_i Z = \frac{\rho}{(m_p + m_e)} \approx \frac{\rho}{m_p}, \quad (2-64)$$

i.e.,

$$\Lambda_{brems} = 1.43 \times 10^{-27} \rho^2 T^{\frac{1}{2}} g_f, \quad (2-65)$$

where, m_p is the mass of the proton, T is the temperature, g_f is the Gaunt factor. In our work, to increase the cooling efficiency, we have taken the cooling index $\beta > 1/2$ but $\beta \leq 1$. So the cooling term in Eq. 2.65 reduces to,

$$\Lambda_{powcool} = 1.43 \times 10^{-27} \rho^2 T^\beta g_f, \quad (2-66)$$

where, everything is expressed in CGS units and g_f is the Gaunt factor which is assumed to be 1.0 throughout our work wherever radiative cooling is used. Now we will discuss how this cooling law is implemented. In each time step of the simulation two different types of coolings are used depending on the optical depth of the region. We begin with the power-law type cooling given in eq. 2.69 where β is chosen to 0.6 (as in Molteni, Sponholz & Chakrabarti, 1996) and at each time step optical depth is computed,

$$\tau = \int N(r, z) \sigma_T dz, \quad (2-67)$$

where, σ_T is Thompson scattering cross section, along the vertical direction from upper and lower grid boundary up to the equatorial plane. As soon as a Keplerian disk starts forming near the equatorial region optical depth of that region abruptly increases forming a surface of the Keplerian disc. In case of optically thick Keplerian disc, the energy is assumed to be radiated from the surface in the form of black body (Giri, Garain, Chakrabarti 2015) radiation whose cooling rate is given as,

$$\Lambda_{bb} = \sigma T^4(r, z) \text{ erg cm}^{-2} \text{ s}^{-1}, \quad (2-68)$$

where, σ is Stefan-Boltzmann constant given by $\sigma = 5.67 \times 10^{-5} \text{ erg cm}^{-2} \text{ deg}^{-4} \text{ s}^{-1}$. In the regions below the surface of the Keplerian disc, no separate cooling is necessary as the energy produced inside the disc is either radiated as black body from the surface or get advected.

2.6 Magnetized inviscid flow

As discussed in the previous chapter, the magnetic activity at the base of the jet region plays a major role in understanding many physical problems such as collimation and acceleration of jets, microvariability in blazars and BL Lac objects etc. As far as the source of the magnetic field is concerned they are steadily supplied with the inflow from the companion. Far away from the black hole, magnetic fields may have all the components but as soon as it gets accreted with the matter, due to large azimuthal velocity of the flow only toroidal component of the field becomes dominant and thus generate toroidal flux tubes. There is another

school of belief that magnetic field may also be generated from some seed field using dynamo mechanism inside the disc (Eardley & Lightman 1975; Galeev et al., 1979; Parker, 1979; Soward, 1978; Meyer & Meyer-Hofmeister, 1982; Pudritz, 1981; Stepinski & Levy, 1988, 1990; Vishniac, Jin & Diamond, 1990; Campbell, 1990; Tout & Pringle 1992 etc.) and also magnetic field can be generated ab initio by Biermann battery effect (Biermann, 1950) as inside a proto galactic tori (Chakrabarti, 1991, Chakrabarti, Rosner & Vainshtein 1994). The advantage of using toroidal magnetic flux tubes is that since it is a closed loop, it will always be divergence free. In an advective disc, the magnetic blob accreted from the companion will be stretched due to differential rotation into mostly azimuthal and opposite directed fields and the turbulent eddies present in the disc may push and reconnect creating more magnetic blobs. Hence the number of magnetic flux tubes will rise. However, a single thick flux tube may also be split into several axisymmetric flux tubes in presence of shear. Detailed analysis of this would require study of turbulences but since the chosen grid size of our simulation is much higher than the size of the turbulence cells it was not possible. In the next sub-section we will discuss the equation of motion of a single isolated flux tube in an advective disc and its effect on the source term we discussed earlier in this Chapter.

2.6.1 Modified Source term

The source function is

$$\mathbf{S} = \begin{pmatrix} 0 \\ \frac{\rho v_\theta^2}{r} - \frac{\rho r}{2(\sqrt{r^2+z^2}-1)^2 \sqrt{r^2+z^2}} - f_{mag,r} \\ -\frac{\rho v_r v_\theta}{r} \\ -\frac{\rho z}{2(\sqrt{r^2+z^2}-1)^2 \sqrt{r^2+z^2}} + f_{mag,z} \\ -\frac{\rho(rv_r+zv_z)}{2(\sqrt{r^2+z^2}-1)^2 \sqrt{r^2+z^2}} \end{pmatrix}. \quad (2-69)$$

Here we have only sub-Keplerian matter advected towards the black hole. Thus the accretion rate is only for sub-Keplerian halo that is advected towards the compact object, not of the conventional Keplerian disk. In order to include the effect of magnetic field the source function is changed but magnetic field is not permeated everywhere in the flow. It is only restricted to the flux tubes whose dynamics we are studying. Thus the Lorentz force is operative only due to them. The source function \mathbf{S} has two terms $f_{mag,r}$ and $f_{mag,z}$ which are r and z components of the Lorentz force due to the presence of toroidal magnetic field. The expression for the Lorentz force is given as,

$$\mathbf{f}_{mag} = \frac{\rho}{(m_{electron} + m_{proton})} \frac{e}{c} (\mathbf{v} \times \mathbf{B}). \quad (2-70)$$

2.6.2 Equation of Motion

Parker (1955) in his pathbreaking work demonstrated how magnetic buoyancy plays a major role in various magnetic activities in sun, such as how magnetic flux tubes generated at the solar interior comes out due to magnetic buoyancy eventually producing solar corona. In case of advective accretion discs around black holes the scenario is quite different as it is believed that flux tubes are accreted along with the matter from the companion only, instead of being produced inside the disc like the sun. The effect of differential rotation is also very pronounced in case of an accretion disc. In the literature there exists a significant amount of work regarding the stability, dynamics of magnetic flux tubes and their different aspects and effects on astrophysical jets (e.g., Shibata & Uchida (1985), Shibata & Uchida (1986), Ferriz-Mas et al. (1989), Moreno-Insertis et al. (1992), You et al. (2005), Longcope & Klapper (1997), Blackman (1996), Fendt & Camenzind (1996), Chakrabarti & D'silva 1994a, D'Silva & Chakrabarti 1994b). We assumed that the flux tube we are considering is azimuthally symmetric and also we employ thin flux tube approximation which enables us to consider that the variation of different physical quantities inside the flux tube is negligible. This approximation holds if the cross sectional radius of the flux tube is smaller compared to the local pressure scale height of the disc. The equations of motion for the thin flux tubes have been written by several authors in the context of solar physics as well as thick disc around a black hole (Choudhuri & Gilman 1987, CD94). Here, following CD94, the equations of motion for thin axisymmetric flux tube are given as,

$$\begin{aligned} \ddot{\xi} - \dot{\xi}\dot{\theta} + \frac{X}{(1+X)}[-\dot{\xi}\dot{\phi}^2 \sin^2 \theta - 2\dot{\xi}\omega\dot{\phi} \sin^2 \theta] = \\ \frac{X}{(1+X)} \left\{ \frac{M}{X} [g - \xi\omega^2 \sin^2 \theta] - T_{ens} \sin \theta - \frac{D_r}{\pi\sigma^2\rho_e} \right\}, \end{aligned} \quad (2-71)$$

$$\begin{aligned} \xi\ddot{\theta} + 2\dot{\xi}\dot{\theta} + \frac{X}{(1+X)}[-\dot{\xi}\dot{\phi}^2 \sin \theta \cos \theta - 2\dot{\xi}\omega\dot{\phi} \sin \theta \cos \theta] = \\ -\frac{X}{(1+X)} \left\{ \frac{M}{X} \xi\omega^2 \sin \theta \cos \theta + T_{ens} \cos \theta + \frac{D_\theta}{\pi\sigma^2\rho_e} \right\}, \end{aligned} \quad (2-72)$$

$$\begin{aligned} \xi \sin \theta \ddot{\phi} + 2\dot{\xi} \sin \theta (\dot{\phi} + \omega) + 2\dot{\xi} \cos \theta \dot{\theta} (\dot{\phi} + \omega) + \xi \sin \theta \\ \left\{ \dot{\xi} \frac{\partial \omega}{\partial r} + \dot{\theta} \frac{\partial \omega}{\partial \theta} \right\} = 0, \end{aligned} \quad (2-73)$$

where, (ξ, θ, ϕ) is the position of a point inside a flux ring having magnetic field B . Here, ξ is measure of radial distance in the unit of Schwarzschild radius (r_g). Here, X is defined as $X = m_i/m_e$ where, $m_i = \rho_i \pi \sigma^2 \cdot 2\pi r \sin \theta$ is the mass of the flow inside the flux tube of radius of cross section (in the meridional plane) σ and $m_e = \rho_e \pi \sigma^2 \cdot 2\pi r \sin \theta$ is the mass of the external flow displaced by the flux tube. The flux $\psi = B\pi\sigma^2$ through the ring remains constant. The flux tube experiences buoyancy and the buoyancy factor is given by,

$$M = \frac{\rho_e - \rho_i}{\rho_e} = \frac{m_e - m_i}{m_e}$$

where ρ_e and ρ_i represent external and internal densities respectively. The effective acceleration due to gravity is,

$$\mathbf{g}_{eff} = (g - \xi\omega^2 \sin^2 \theta)\hat{\xi} - \xi\omega^2 \sin \theta \cos \theta \hat{\theta} \quad (2-74)$$

where, g is given as $g = 1/2(\xi - 1)^2$ in Schwarzschild unit. The drag force per unit length is given as,

$$\mathbf{D} = -0.5C_D\rho_e\sigma|(\dot{\xi} - v)\hat{\xi} + \dot{\xi}\dot{\theta}\hat{\theta}|(\dot{\xi} - v)\hat{\xi} + \dot{\xi}\dot{\theta}\hat{\theta} \quad (2-75)$$

where, $C_D = 0.4$ is a dimensionless coefficient that has constant value of 0.4 for high Reynold's number (Goldstein, 1938). It is often said that a magnetic field line is like a rubber band. Just as a stretched band returns to its original size when released, a closed magnetic flux tube also has a tension which is often the most important force component. The tension force is given by

$$T_{ens} = \frac{4\pi M_0 T_e(\xi_0)}{\mu_e A(1 - M_0)\xi_0 \sin \theta_0} \quad (2-76)$$

which is a dimensionless measure of the magnetic tension (CD94) where, $T_e(\xi_0)$ is the initial temperature of the external fluid, (ξ_0, θ_0) is the initial position of the flux tube, A is area increment factor given as $A = (\sigma/\sigma_0)^2$ where σ_0 is the initial cross sectional radius and σ is the instantaneous radius, and M_0 is the initial buoyancy factor, which is calculated to be $M_0 = B^2/8\pi p_{g,e}$ where, $p_{g,e}$ is external gas pressure. As $A(t) = \sigma^2(t)/\sigma_0^2$, this gives the evolution of the flux tubes over the course of the simulation. Explicit form of this area expansion factor is given as (CD94),

$$A = \left(\frac{T_e(\xi_0, \theta_0)}{T_e(\xi, \theta)} \right)^3 \left(\frac{\xi_0 \sin \theta_0}{\xi \sin \theta} \right) \left(\frac{1 - M_0}{1 - M} \right) \quad (2-77)$$

where, $T_e(\xi, \theta)$ is directly coming from our simulation at each instant of time.

2.6.3 Adiabatic picture and Calculation of Magnetic Buoyancy:

The magnetic buoyancy factor (M) strictly depends on the nature of the energy transfer between disc and the flux tube and also on the initial entropy condition of the flux tube. There can be two way how the energy transfer between disc and flux tube happens, first one is by isothermal procedure and second one is according to adiabatic procedure though in realistic case the actual process lies between these two extremes. Here, we have considered that the flux tube moves adiabatically with the surrounding fluid i.e., there is no heat exchange between them. The entropy inside the flux tube remains constant throughout the dynamics of the flux ring. Hence, unlike the isothermal condition the radiation pressure inside the tube is not equal to the radiation pressure of surrounding fluid. Thus, using the fact that the flux tube is in pressure equilibrium with the surroundings we have,

$$p_{r,i} + p_{g,i} + \frac{B^2}{8\pi} = p_{r,e} + p_{g,e}, \quad (2-78)$$

where, $p_{r,i}$ and $p_{r,e}$ are radiation pressure for internal and external fluid and $p_{g,i}$ and $p_{g,e}$ are gas pressure for internal and external fluid. The ratio of gas pressure (p_g) to total pressure ($p_r + p_g$) is denoted by a constant β . From eq.2.81, using the assumption that the flux tube is in thermal equilibrium with the surrounding just prior to its release, we get,

$$\frac{B}{\rho_i \xi \sin \theta} = \text{constant} \quad (2-79)$$

Since the flux tube moves adiabatically, we have,

$$\frac{p_i}{p_{i0}} = \left(\frac{\rho_i}{\rho_{i0}} \right)^\gamma \quad (2-80)$$

$$\frac{p_e}{p_{e0}} = \left(\frac{\rho_e}{\rho_{e0}} \right)^\gamma \quad (2-81)$$

$$\frac{T_i}{T_{i0}} = \left(\frac{\rho_i}{\rho_{i0}} \right)^{\gamma-1} \quad (2-82)$$

$$\frac{T_e}{T_{e0}} = \left(\frac{\rho_e}{\rho_{e0}} \right)^{\gamma-1} \quad (2-83)$$

where, p and T represents pressure and temperature respectively and the subscripts i , e , & 0 represents flow inside the tube, external flow, and initial values of the physical quantities respectively. After rearranging and then dividing eq. 2.81 by $p_{g,e}$ we get,

$$\frac{1-\beta}{\beta} \left(1 - \frac{p_{r,i}}{p_{r,e}} \right) + 1 - \frac{p_{g,i}}{p_{g,e}} = \frac{B^2}{8\pi p_{g,e}} \quad (2-84)$$

putting $p_r = \frac{1}{3}aT^4$ and using the fact that $T_{i0} = T_{e0}$ in Eq. 2.87 we get,

$$\frac{1-\beta}{\beta} \left(1 - \frac{(T_i/T_{i0})^4}{(T_e/T_{e0})^4} \right) + 1 - \frac{(p_{g,i}/p_{i0}) p_{i0}}{(p_{g,e}/p_{e0}) p_{e0}} = \frac{B^2}{8\pi p_{g,e}} \quad (2-85)$$

Using eq. 2.82 - 2.86 into eq. 2.87 we get an expression for ρ_i/ρ_e ,

$$k_1 \left(\frac{\rho_i}{\rho_e} \right)^{4/3} + k_2 \left(\frac{\rho_i}{\rho_e} \right)^2 - 1 = 0, \quad (2-86)$$

where,

$$k_1 = \frac{(1 - \beta_e M_0)}{(1 - M_0)^{4/3}},$$

$$k_2 = \beta_e \frac{M_0}{(1 - M_0)^2} \left(\frac{T_e}{T_{e,0}} \right)^2 \left(\frac{\xi \sin \theta}{\xi_0 \sin \theta_0} \right)^2.$$

By solving this equation we get ρ_i/ρ_e and hence the magnetic buoyancy (M) and using eq. 2.80 we can eventually calculate the area expansion factor which gives us the cross sectional radius and magnetic field value at each time step.

Chapter 3

Simulation setup & Testing

A realistic accretion disc is non-axisymmetric, three dimensional and time dependent with many complex features embedded into it. It has viscous dissipation, radiative cooling and magnetic fields, each of which play different roles helping us to explain different observed phenomena. It is wise to start with the most simple setup, such as the spherical symmetric flow and slowly build up on that adding new features. In most of these cases, it is useful to assume the flow to be axisymmetric so that one can study its behavior on the $r - z$ plane of cylindrical co-ordinate system. This flow is essentially two dimensional. We first consider a spherical symmetric flow and then add magnetic field to it. As the next step we add angular momentum ignoring the viscous and radiative cooling part to make the flow inviscid. We study non magnetized and magnetized cases of the inviscid flow. Lastly we add viscosity and radiative cooling to investigate further. In this chapter, we shall discuss how we gradually set up the problem starting with spherical symmetric flow and discuss the assumptions and way the boundary condition is implemented.

3.1 Simulation Setup

Our simulations consist of two parts. In the first part, we solve the hydrodynamic equations for both inviscid and viscous systems and in the second part, we couple the hydrodynamics of the flow with the equations describing dynamics of magnetic flux tubes. All the necessary equations and the changes made to the hydrodynamics are already discussed in 2. We use injection methods and boundary condition same as Giri et al. (2010) and Giri & Chakrabarti (2014) but with some changes which will be discussed in the subsequent sections here. We

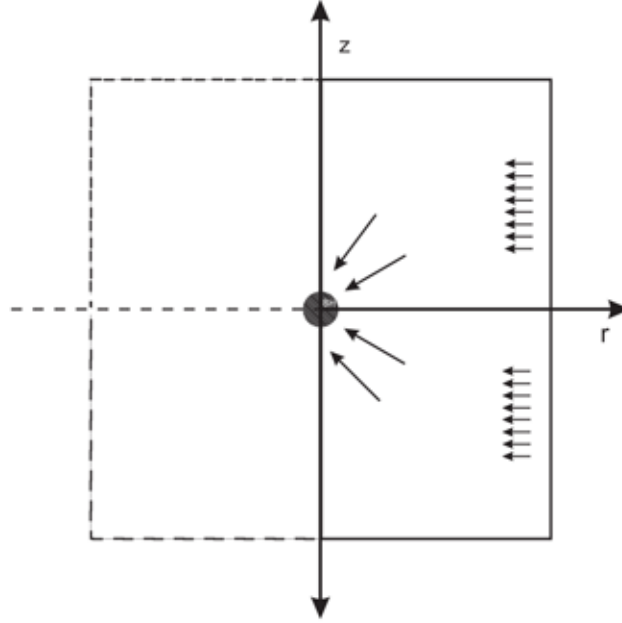


Figure 3.1: A schematic diagram of the system under consideration. Solid box is our computational region on the $r - z$ plane. No reflection symmetry along the equatorial plane has been assumed.

use Total Variation Diminishing scheme (Harten, 1983) for solving the hydrodynamical equations and for dynamics of the magnetic flux tubes we have used a fourth order Runge-Kutta scheme for second order system of coupled ordinary differential equations (ODE) all of which have been discussed in 2.

3.1.1 Geometry of the System:

For our simulation we consider that matter accreted from the companion is flowing towards the black hole axisymmetrically in the pseudo-Newtonian gravitational field of the central compact object. A black hole of mass M_{bh} is assumed to

be at the origin of the chosen co-ordinate system. Here, we have chosen a cylindrical co-ordinate system (r, θ, z) . We assume the pressure of the gas at infinity to be very low and specific energy to be zero. The gravitational field is chosen to be a Paczyński-Wiita type potential (Paczyński & Wiita, 1980). For simplicity we have constrained ourselves only to first and fourth quadrant of the $r - z$ plane of cylindrical co-ordinate system. The flow behavior can be generated in other two quadrants using reflection symmetry along z axis. Unlike Giri et al. (2010) and Giri & Chakrabarti (2012, 2014) we do not use any reflection boundary condition along r axis. The magnetic flux tube is symmetric about the axis of rotation of the disc and has only the azimuthal component of the field. To write the equations of motion for the magnetic flux tube which dictates its dynamics we have used spherical co-ordinate system. Hence, the position of slender flux tube is denoted by (r, θ, ϕ) . Since our system is two dimensional for a given θ (co-ordinate system of hydrodynamic code which is cylindrical) we can only see a cross section of the flux tubes.

3.1.2 Computational Box and Initial Conditions

The computational box occupies two quadrants of the $r - z$ plane of the cylindrical co-ordinate system. The size of this computational box is $0 \leq r \leq r_{out}$ in r direction and in z direction it spans as $-z_{out} \leq z \leq z_{out}$. Here, r_{out} is the outer boundary and z_{out} and $-z_{out}$ denotes the upper and lower boundary of the computational box respectively. Since, we are using finite difference method our system is grid based. If we have N_r number of grids in r direction and N_z number grids in z direction the grid sizes in r and z direction are $\Delta r = \frac{r_{out}}{N_r}$ and $\Delta z = \frac{2z_{out}}{N_z}$ respectively. In order to mimic the horizon ($r = 1 r_g$) we place an absorbing boundary at a region called inner boundary and in our simulation this inner boundary varies from $1.1 r_g$ to $2.5 r_g$. Initially, before injecting any matter into the computational grid we fill the box with a stationary gas with a very low density ($\rho_{bg} = 10^{-6}$). This is done to avoid any singularities till the grid is filled with actual matter. The injected matter is assumed to have a density $\rho_{in} = 1$ at the equatorial region and the density of matter at other grid points is scaled with respect to that. The initial low density matter will obviously be washed out by the incoming matter within a dynamical timescale. Since initial low density gas inside the computational box is stationary, only matter injected at the outer boundary will have non-zero velocity components and so the Mach number will also be non-zero at the outer boundary (r_{out}). In order to simulate the magnetized

flow, the initial conditions for the hydrodynamic part remains the same but a new set of initial conditions and parameters are introduced. Initially it is assumed that at the time of injection at the outer boundary the magnetic flux tube is stationary i.e., the initial velocity components (\dot{r} , $\dot{\theta}$, $\dot{\phi}$) of the flux tube are zero. In order to initiate the magnetized simulation we need an initial value of magnetic field intensity ($0, 0, B_\phi$) and initial magnetic buoyancy factor which can be found using the ratio between magnetic pressure and external gas pressure. We also need to supply the initial cross sectional radius of the flux tube and since drag force acting on the flux tube depends on the cross sectional radius of the flux tube, this parameter will have a major effect on the dynamics of the flux tube.

3.1.3 Boundary conditions

A simple outflow boundary condition is employed where the gradient of all the physical quantities are set to zero at the boundary in both the quadrants. We have not implemented any reflecting boundary condition along the r axis and reflecting boundary is set along the z axis for both the quadrants. By revoking the reflection boundary condition from the r axis we allowed the vertical oscillation of the shock front along with the horizontal oscillations. However, the flow remains axisymmetric as a reflecting boundary is invoked along the z axis. At the outer boundary, $r = r_{out}$, along the z boundary, matter is injected with supersonic velocity. We use the fact that the total energy of the injected flow is conserved at the boundary points for a given angular momentum. Thus we have the expression,

$$\epsilon = \frac{v_r^2}{2} + na^2 + \frac{\lambda^2}{2r^2} + \Phi(R) \quad (3-1)$$

where, n is the polytropic index, λ is the angular momentum and Φ is the pseudo-Newtonian gravitational potential given as,

$$\Phi(R) = -\frac{1}{2(R-1)}$$

where, $R = \sqrt{r^2 + z^2}$ for cylindrical co ordinate system and a is the sound speed. Now, if the flow is in hydrostatic equilibrium in the z - direction we get the height of the disc as a function of radial distance which is given as,

$$z(r) = ar^{\frac{1}{2}}(r-1)$$

and we can compute the sound speed (a) from this expression for a given r and z .

3.1.4 Comment on the Code Units

In our simulation the physical quantities are written in dimensionless manner. To achieve this, we have considered, $2G = M = c = 1$ where, M is solar mass, G is gravitational constant and c is velocity of light. Thus the units for mass becomes M_{\odot} , for length becomes $\frac{2GM_{bh}}{c^2}$, for velocity becomes c and for time becomes $\frac{2GM_{bh}}{c^3}$. The mass accretion rate is measured in the unit of mass Eddington rate given as $\frac{L_{Edd}}{c^2}$ where $L_{Edd} = 1.2 \times 10^3 8M_{bh}$. For our simulation purpose we consider only stellar mass black hole of $10 M_{\odot}$ but the result will remain equally valid for supermassive black holes as well. Only time and length scales will vary as they involve mass of the central object. Simulations are run for several thousands of dynamical time which in reality corresponds to few seconds of physical time.

3.2 Testing of the Code: non-magnetized and Magnetized:

In order to validate the code both magnetized and non-magnetized (without reflection symmetry along r axis) we must choose a known analytical solution of a test model and try to see whether it will match with the simulation of same model. So, for this purpose we chose a test case where a stationary gas cloud of low density and zero angular momentum sitting at the infinity will fall towards a central object spherically and try to match the simulation results with the analytical one. This spherical flow of gas is known as Bondi flow. We use the analytical solution of this flow at the outer boundary and inject the matter accordingly.

3.2.1 spherical flow without reflection symmetry

Bondi flow is a spherical flow of a gas falling towards a point mass due to Newtonian gravity (Bondi, 1950). In order to simulate a two dimensional Bondi like spherical flow, we have chosen a computational box of dimension $0 \leq r \leq 200 r_g$ in r direction and $-200 r_g \leq z \leq 200 r_g$ in z direction. The outer boundary is placed at $r_{out} = 200 r_g$. Since, we will use a finite difference code we have to define proper grid size. For this purpose, we have considered the number of grids in r -direction to be $N_r = 512$ and in z -direction to be $N_z = 1024$ and thus the grid size in both the directions is $0.39 r_g$. We choose the units used in the code in such a way that the outer boundary (r_{out}) becomes unity and also the density gets

normalized to unity at the equatorial plane. The central object is a Schwarzschild stellar mass black hole of mass $M_{bh} = 10M_{\odot}$. The gravitational potential is considered to be a Pseudo-Newtonian gravitational potential (Paczynski & Wiita, 1980) which is given as $\Phi_g = \frac{1}{2(R-1)}$ written in units of r_g . Calculations of the units of other physical quantities are done according the process shown in previous section. As previously discussed we have to specify radial velocity and sound speed at the outer boundary and the matter is injected with that velocities. In this case, the velocities are calculated using analytical Bondi solution. Now, since Bondi flow is a spherically symmetric flow, matter has to be injected from all the boundaries not only outer z boundary but both upper and lower r boundaries as well. The other boundary conditions are same as described in the previous section. We run the simulation for several hundred dynamical time scale until the steady state is achieved and then we compare our simulation results with the analytical solution. In Fig. 3.2 we have plotted the spatial variation of density and velocity vectors. From the figure it is evident that the density and velocity of the gas increases as it approaches towards the black hole. These are basically snapshots of our hydrodynamical simulation once it reached the steady state. From the density plot we see the spherical nature of the flow. In fig 3.3 we compare our simulation result with analytical 1-dimensional Bondi solution. In panels labelled (a) and (c) we have plotted the radial velocity and Mach number distribution respectively obtained from the hydrodynamic simulation and in panels (b) and (d) we have plotted the radial velocity and Mach number distribution obtained from the analytical solution. It is evident that the simulation result matches with that of the analytical result.

3.2.2 Magnetized Spherical Flow

In order to test the magnetized code we considered the same spherical Bondi flow just with a minute change i.e., a toroidal magnetic field is released at the outer boundary. Hence the numerical procedure and the simulation setup for the hydrodynamics discussed above in the previous sections remains same. We just change the source function in the manner already described in the section 2.6.1 which makes the flow magnetized. We choose the initial parameters for which we need to solve the dynamics of the flux tube. We consider the initial cross sectional radius for the flux tube to be $0.001 r_g$ and the initial magnetic buoyancy factor is chosen to be very small 0.01. After running the simulation for a sufficiently long time to obtain a steady value we have injected the flux tube and have observed

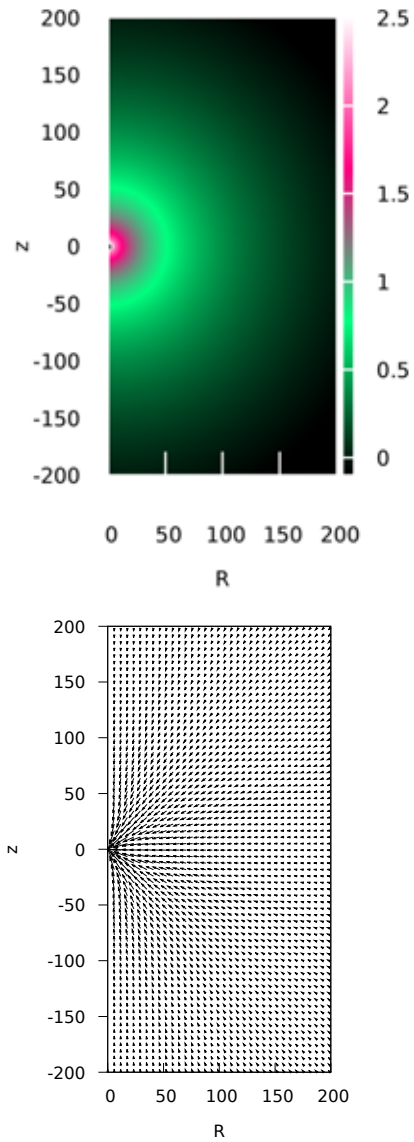


Figure 3.2: Density colour plot and velocity vector plot of a spherical Bondi flow for non-magnetized case. No reflection symmetry along the equatorial plane has been assumed.

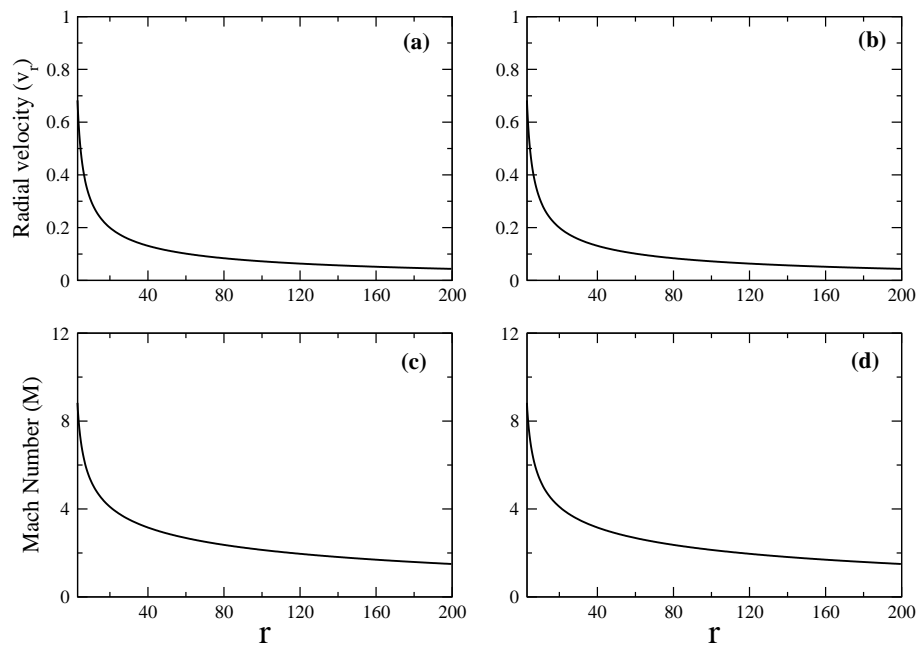


Figure 3.3: Comparison between radial velocity and Mach number plot obtained from hydrodynamic simulation and analytical solution respectively. Plots in panel (a) and (c) are from simulation and plots in panel (b) and (d) are drawn using analytical solution.

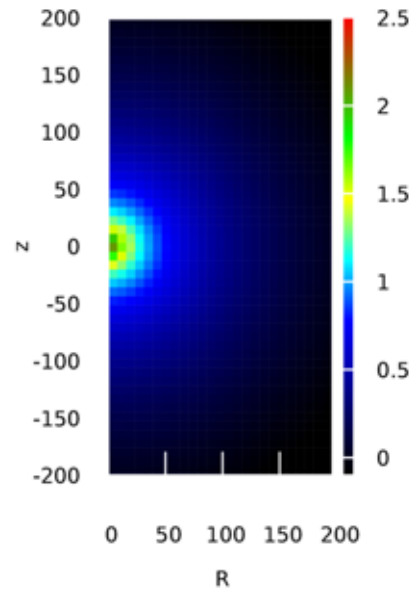


Figure 3.4: Density colour plot and velocity vector plot of a spherical Bondi flow for magnetized case. No reflection symmetry along the equatorial plane has been assumed.

that the flow remains spherical (see 3.4) as we have seen in the previous section.

Chapter 4

Non Magnetized Inviscid Flow

Various research groups (e.g., Hawley, Wilson & Smarr 1984; Eggum, Coroniti, & Katz 1985; Chakrabarti & Molteni, 1993; MLC94; Ryu, Brown, Ostriker & Loeb 1995; Molteni, Sponholz & Chakrabarti 1996; Molteni, Ryu & Chakrabarti, 1996, hereafter, MRC96; Ryu, Molteni & Chakrabarti, 1997, hereafter RMC97; Igumenshchev, Abramowicz & Narayan 2000; Chakrabarti, Acharya & Molteni, 2001, hereafter CAM01; Giri et al., 2010, hereafter GC10) presented a large number of numerical simulations of inviscid accretion flows around black holes. These simulations invoked standard reflection boundary condition on the equatorial plane with the assumption that the flow has an equatorial symmetry and therefore the flow behavior was studied only on one quadrant i.e., first quadrant. In MLC94 and GC10, the results of standing and oscillating shock formations in inviscid flows are presented using Smoothed Particle Hydrodynamics (SPH) method and finite difference method respectively. In GC10, simulations were carried out using two conserved quantities, namely, specific energy E and specific angular momentum λ as flow parameters chosen from the parameter space that provides the complete set of black hole accretion flow solution (Chakrabarti 1989; hereafter C89). Also, several simulations have been carried out without using any reflection symmetry along the equatorial plane by various groups for both black hole accretion (Molteni et al., 2001, hereafter M01; Chakrabarti, Acharya & Molteni, hereafter CAM01) as well as wind accretion onto stars (Fryxell & Taam, 1988; Taam & Fryxell, 1989; Matsuda et al., 1991, 1992). In M01 and CAM01, utilizing SPH, it was demonstrated that an instability can happen in the stream. They likewise showed that albeit matter being injected symmetrically, those instabilities may not remain symmetric with respect to the central plane. Moreover, incoming flow interacts strongly with the outgoing wind resulting in an instability in the flow (M01). SPH is known to be dissipative in nature and it is not inconceivable

that in energy conserving schemes one may see that such oscillations are really disrupting the matter flow. We, therefore, in this chapter extend the work of GC10 where energy is accurately preserved by removing the reflection condition along the equatorial plane and while doing so we intend to give answers to the following important questions in the subsequent sections: (a) Will the accretion flow be symmetric with respect to the equatorial plane? And if so, under what conditions? (b) Will this two quadrant flow have any effect on the formation of the so called ‘CENBOL’? This question is especially relevant as the CENBOL acts as the Compton cloud (Chakrabarti 1995, Chakrabarti 1997, Chakrabarti & Titarchuk 1995) while explaining the spectral and timing properties of black hole candidates. (c) If the flow symmetry is absent then will the accretion flow remain stable at all or the flow would be violent and disrupted? (d) What will be its effects on outflows which are known to be produced on the CENBOL surface?

4.1 Simulation set up and procedure

The computational box consists of two quadrants (first and fourth quadrant) as described in previous chapter. Here, we utilize the reflection symmetry condition just on the z -axis to realize the assumption that the flow around the black hole is axisymmetric in nature and hence obtain the solution in other quadrants. The inner boundary condition is required to constrain the flow to be axisymmetric near the black hole. The incoming gas enters the computational box symmetrically with respect to the equatorial plane through the outer boundary situated at $r_b = 200 r_g$. We inject the matter with radial velocity v_r , the sound speed a (i.e., temperature) at the boundary computed using the hybrid model and the boundary values of density ρ are supplied from the standard vertical equilibrium solution (C89). We scale the density so that the injected gas has the density of $\rho_{in} = 1.0$ at the equatorial plane. With a specific idea to emulate the horizon of the black hole, we put an absorbing inner boundary condition at $R = 2.5r_g$, inside which all the approaching matter is absorbed totally into the black hole. The inner sonic point is formed around this radius anyway, thus this decision of placement of the inner boundary does not influence the flow elements. In order to avoid any occurrence of singularities due to ‘division by zero’, we fill the grid with an initial matter of low density $\rho_{bg} = 10^{-6}$ having a sound speed (or, temperature) to be the same as that of the injected matter. Henceforth, the incoming matter has a pressure 10^6 times greater than that of the initial background matter. Obviously, this background matter is completely washed out and supplanted by

the injected matter within a dynamical time scale.

Initially, the low-density matter with which the computational grids are filled in is assumed to be static, i.e., the radial (v_r), rotational (v_ϕ) and azimuthal (v_z) velocity components are zero for all the grids apart from those on the outer boundary. Hence, the Mach number is zero everywhere with the exception of the outer boundary at the beginning of the simulation. The simulations were performed with a high resolution of 512×1024 grid points. Therefore, every r and z -grid has a size of 0.3906 in units of the Schwarzschild radius. Figure 3.1 indicates schematically our framework on the $r - z$ plane in the cylindrical coordinate system. In this chapter, we wish to investigate the stability of CENBOL and unsteadiness in the accretion disc around a black hole. All the simulation cases were done assuming a stellar mass black of mass $M_{BH} = 10M_\odot$. The conversion of the simulation's time unit to the physical unit is $2GM_{BH}/c^3$, and accordingly, the physical time for which the program was run would scale with the mass of the black hole. We generally find that the infall time from the outer to the inner boundary is about $\sim 0.5s$. This is calculated by summing $dr / \langle v_r \rangle$ over the whole radial grid, $\langle v_r \rangle$ being averaged over 20 vertical grids. We carry out the simulations over a few dynamical time-scales after any transient effects which may occur at the beginning.

4.2 Instability due to breaking of the reflection symmetry

In the earlier simulations (GC10, MLC01), the objective was to check whether the shocks could be created at the theoretically predicted positions, and if so, how does the puffed up post-shock region behave in reference to the thick accretion flow. In this section, we shall check whether the CENBOL truly stays symmetric with respect to the equatorial plane if we remove the reflection symmetry that was imposed on earlier simulations.

4.2.1 Formation and deformation of CENBOL

In GC10 all the simulations were carried out under the assumption that the flow is symmetric with respect to the equatorial plane and hence injection of matter was done just in one quadrant. M01, in their work involving cooling processes, has demonstrated that some instabilities got introduced in the accretion disc even in SPH simulations where angular momentum is conserved well (see,

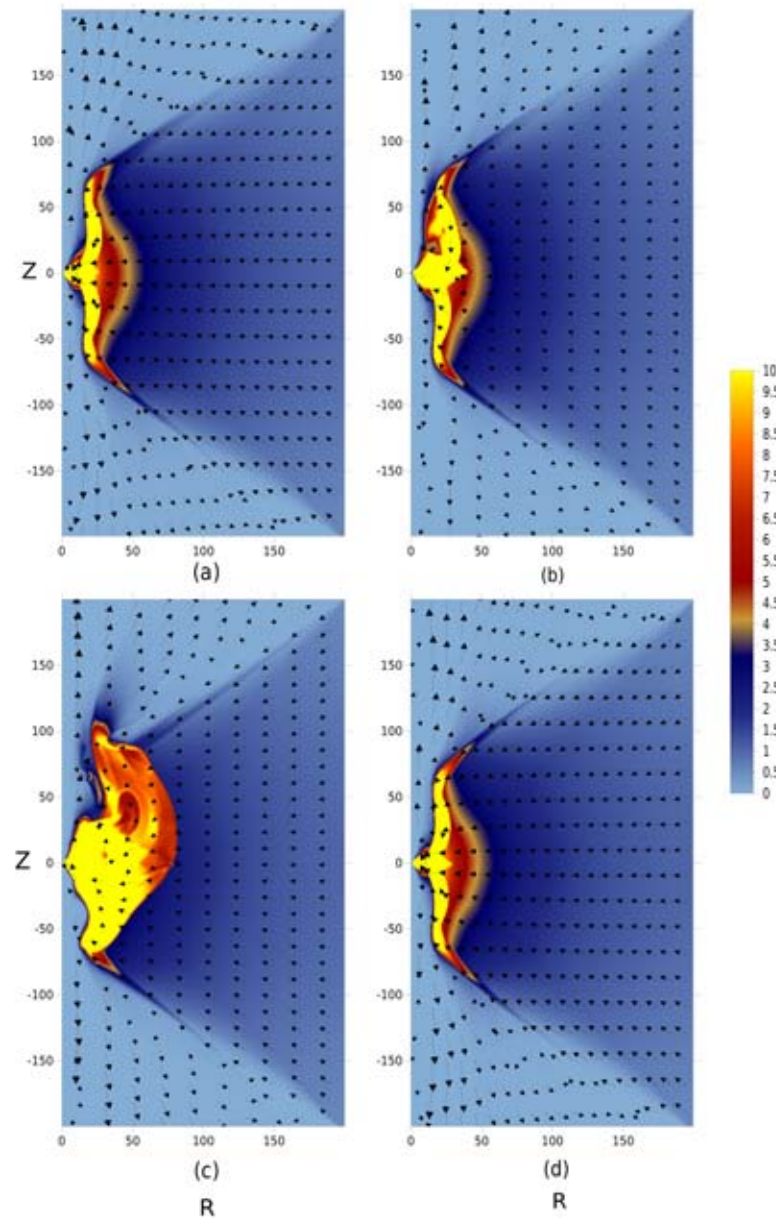
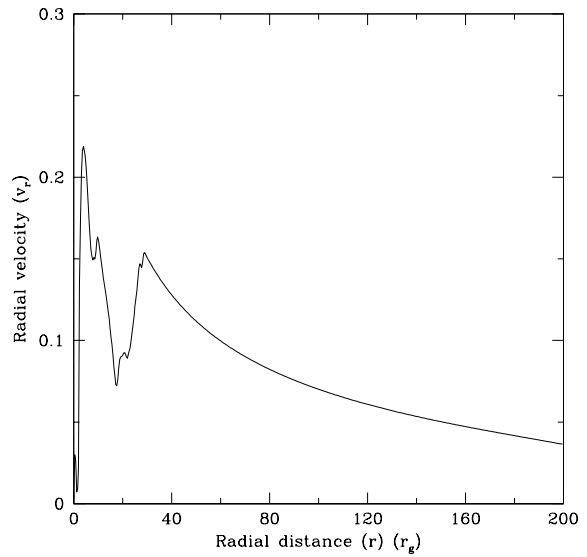
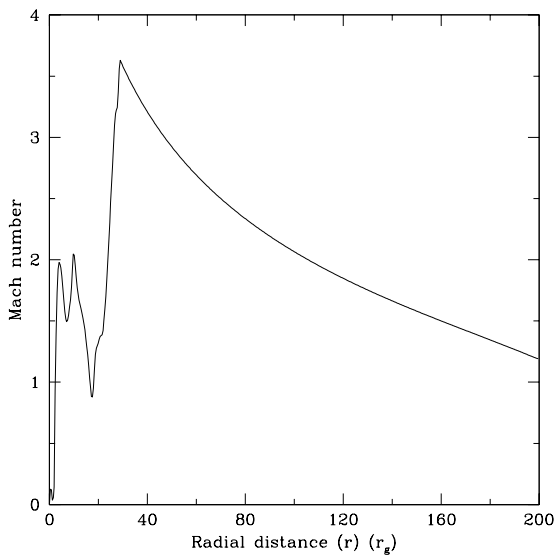


Figure 4.1: Density and velocity vector map to show quasi-periodic formation and deformation of the CENBOL at (a) $t = 21.36$ s, (b) 21.84 s, (c) 22.08 s and (d) 24.95 s. Specific angular momentum is considered to be $\lambda = 1.6$. In (a), high density region due to centrifugal supported boundary layer (CENBOL) has a symmetric shape. In (b), symmetry is about to be broken due to vertical oscillation of the perturbing mass. In (c), CENBOL is deformed but not destroyed. In (d), the CENBOL is restored back (Deb, Giri, Chakrabarti, 2016).



(a)



(b)

Figure 4.2: Radial distribution of the (a) radial velocity component and (b) radial Mach number (v_r/a) on the equatorial plane. Time is $t = 24.95$ s and specific angular momentum is $\lambda = 1.6$. We clearly see the slowing down of matter at the centrifugal barrier (a) and a supersonic to sub-sonic transition (b) forming a shock (Deb, Giri, Chakrabarti, 2016).

MRC96, RCM97). Chakrabarti et al. (2004) have demonstrated that the quasi-periodic variabilities are caused because of vertical as well as horizontal oscillation of shock waves in a two dimensional axisymmetric flow utilizing Smooth Particle Hydrodynamics (SPH). The results of the numerical simulations shown in this Chapter are obtained utilizing a code based on Total Variation Diminishing (TVD) scheme. Following C89, we inject matter at the outer boundary maintaining the vertical equilibrium. The injection rate of the momentum density is kept uniform all through the injected height (in this case, height of the total computational box) at the outer boundary. We stop the simulations at $t = 95$ s (physical time). This time is more than two hundred times the dynamical time of the flow. The solutions shown in Fig. 4.1(a-d) are at 45-50 times the dynamical time, long after the transient effects (~ 1 s) vanish. In this manner, the effects seen are genuine and can be relied to study the spectral properties. C89 anticipated that the standing shocks can form if $\lambda > 1.525$. We find that, indeed, CENBOL is formed whenever $\lambda > 1.5$, the 'discrepancy' could be because of the presence of turbulence pressure (produced by the interaction between the fluid bounced off the CENBOL and the incoming fluid in the post-shock region.) which enables the development of CENBOL to even at a lower angular momentum. In Fig. 4.2, we demonstrate the distribution of radial velocity and the Mach number which is the ratio between the radial velocity ($\langle v_r \rangle$) and sound speed ($\langle a \rangle$). The radial velocity and the sound speed are averaged over 10 grid points situated on either side of the equatorial plane. The plot is drawn for $t \sim 24.95$ s. The radial velocity abruptly drops at the shock location where the flow becomes subsonic as confirmed by the Mach number distribution. As the time advances, the shock is found to oscillate radially and vertically.

4.2.2 High angular momentum case

We repeat the simulation with a larger specific angular momentum. We use $\lambda = 1.7$. The centrifugal force increases moving the location of the shock further out and in this way the CENBOL is expanded. However, it can be observed that when the transient phase is passed, the CENBOL participates in a vertical oscillation around the equatorial plane. We additionally see that the outflowing wind is interacting with the approaching accreting matter making a weaker oblique shock close to the upper right and lower right corners. In Fig. 4.3(a-d), we plot the density and velocity vector maps of the fluid flow at $t = 17.34$ s, 22.57 s, 39.13 s, and 43.23 s respectively. The CENBOL takes a complex shape. It is also clear

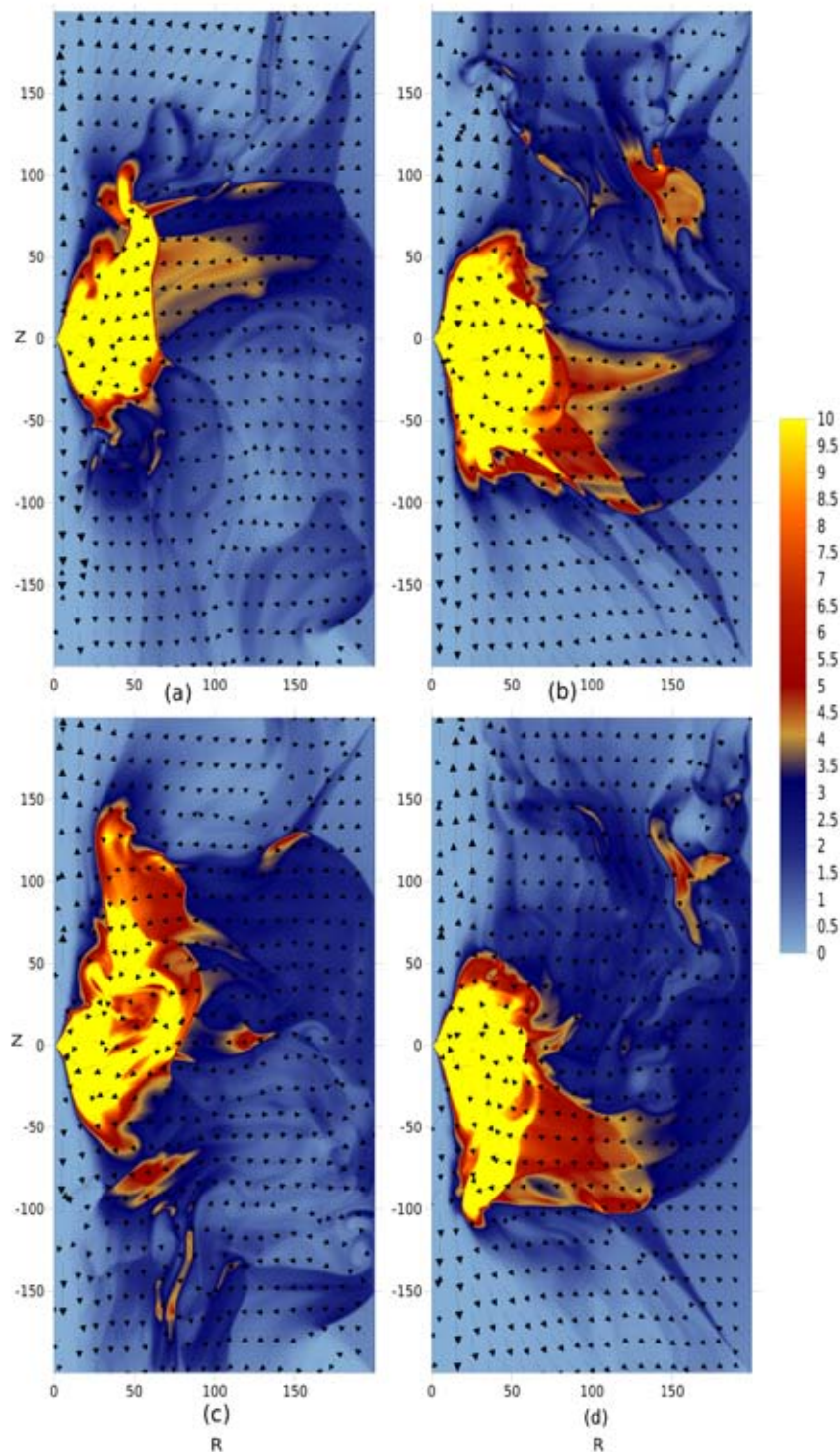


Figure 4.3: Density and velocity vector plots of the accretion flow to show instability within the flow. (a) and (c) show that the CENBOL is shifted above: flow density is higher in the upper quadrant and (b) and (d) show that the CENBOL is shifted below: flow density is higher in the lower quadrant. Plots are drawn at $t = 17.34, 22.57, 40.08,$ and 43.2 seconds respectively. Specific angular momentum is considered to be $\lambda = 1.7$ (Deb, Giri, Chakrabarti, 2016).

that the outflows oscillate, i.e., there are times when the outflow from the upper quadrant is very high. At some other times the outflow in the lower quadrant is substantial. The discs in Fig. 4.3(a) and Fig. 4.3(c) have the CENBOL moved marginally to upper quadrant and the outflow rate from the upper boundary is observed to be bigger. Nonetheless, discs in Fig. 4.3(b) and Fig. 4.3(d) have the CENBOL moved marginally towards the lower quadrant and the outflow is observed to be bigger. In the present setting, we note that the disc instability is higher when the specific angular momentum is increased.

Two important physical processes are triggered by the angular momentum: (i) infalling matter hits the centrifugal barrier (characterized by the region where the outward centrifugal force matches with the inward gravitational force) and reflects back close to the equatorial plane. This flow goes against the infalling matter and two turbulence cells of opposite vorticities are created, one above and the other beneath the central plane. (ii) Centrifugal pressure driven winds are formed which also flow outwards (sandwiched between the centrifugal barrier and the supposed funnel wall, for more details see, Molteni et al. 1996b), confronting the incoming flow away from the equatorial plane. This interface is thus vulnerable to Kelvin-Helmholtz instability. In every one of the cases of the simulations we performed, we found that for low angular momentum, the wind does not form at all and hence this instability is missing. Higher the angular momentum, stronger is the shear instability between the incoming and outgoing components. At the point when the amplitude of the fastest growing mode approaches toward becoming non-linear, instabilities in the upper and lower parts join and push the whole disc on one side or the other. This could be the reason for the vertical motion. This requires further study.

The simulations we did are inviscid in nature and therefore the flow motion exhibited violence when angular momentum is increased because the later is not transported away due to absence of viscosity. Likewise, we have excluded radiative cooling, on account of which, the fluid is extremely hot inside CENBOL. It has already been proposed that the shock oscillations could explain quasi periodic oscillations (QPOs) observed in black hole candidates.

4.3 Effect on the inflow-outflow ratio

In Fig. 4.4, we plot the ratio of the outflow rate to steady injected rate. The dot-dashed curve represents the ratio of the net outflow rate (\dot{M}_{out}) and the net

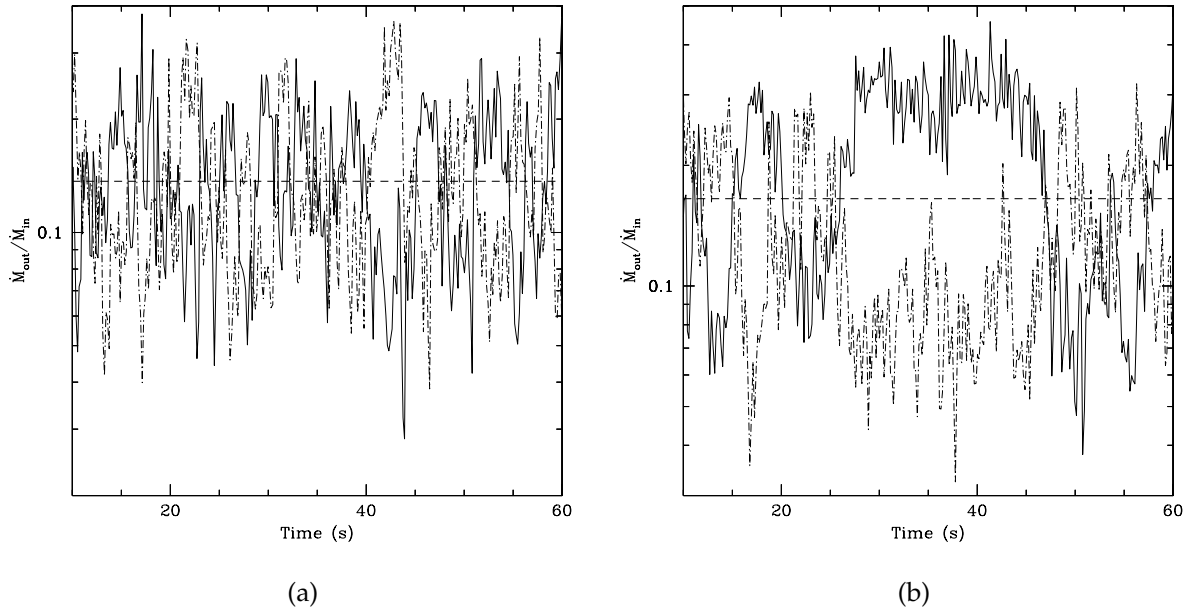


Figure 4.4: Time variation of the ratio between the total outflow rate (\dot{M}_{out}) and the total inflow rate (\dot{M}_{in}) showing an anti-correlated behavior. When the outflow rate from the upper boundary is high, the outflow rate in the lower boundary is low and vice versa. Here (a) $\lambda = 1.7$ and (b) $\lambda = 1.8$. Dot-dashed curve represents the outflow inflow rate ratio in upper quadrant, solid curve represents the ratio in lower quadrant, and dashed curve represents the mean value (time averaged) of the outflow inflow rate ratio. We note that the mean outflow rate as well as the degree of deviation from the mean is higher when angular momentum is higher (Deb, Giri, Chakrabarti, 2016).

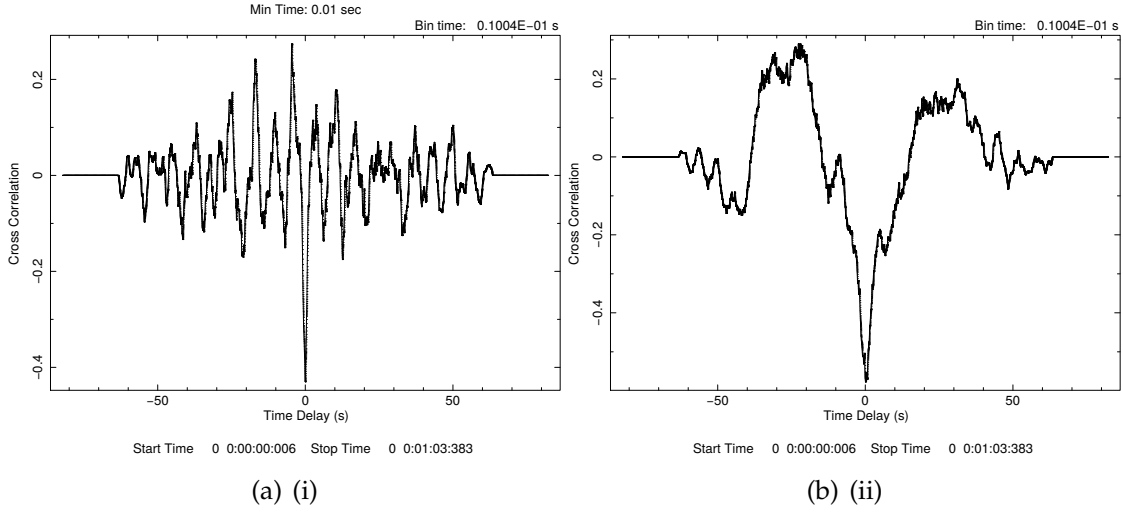


Figure 4.5: Plot of cross correlation between total outflow rates from upper and lower quadrant to show the anti-correlated behavior of the outflow. Fig 4.5(a) is drawn for $\lambda = 1.7$ and 4.5(b) is drawn for $\lambda = 1.8$ (Deb, Giri, Chakrabarti, 2016).

inflow rate (\dot{M}_{in}) in the upper quadrant, solid curve denotes the same ratio in lower quadrant, and dashed curve shows the mean value (time averaged) of the ratio. In Fig. 4.4(a) and Fig. 4.4(b), we choose $\lambda = 1.7$ and 1.8 respectively. We take note of that outflow rate and the mean rate increase with the increment of specific angular momentum. This further strengthen the argument that the outflow is driven by the centrifugal barrier. The overall rate is observed to be about 5 – 10% of the inflow rate. We additionally note that the deviation from the mean increases as well, showing that for higher λ , stronger vertical oscillation sets in. This was likewise found in the density and velocity plots. The plots 4.4(a) and 4.4(b) demonstrate anti-correlated behavior between the outflow rates from the upper and the lower boundary and this conclusion is corroborated by figs. 4.5(a-b) where we have plotted the cross correlation coefficients.

4.4 Time Variation of Shock Location

We continue further investigation into the accretion flow for both low and high specific angular momentum case by looking into the time variation of shock location. Here, the specific angular momentum we have chosen are $\lambda = 1.6, 1.7, \& 1.8$. In figs. 4.6(i)-4.8(i) we have plotted the time variation of the shock location. In those plots, the panels marked with (a) and (b) in group (i) depicts the shock lo-

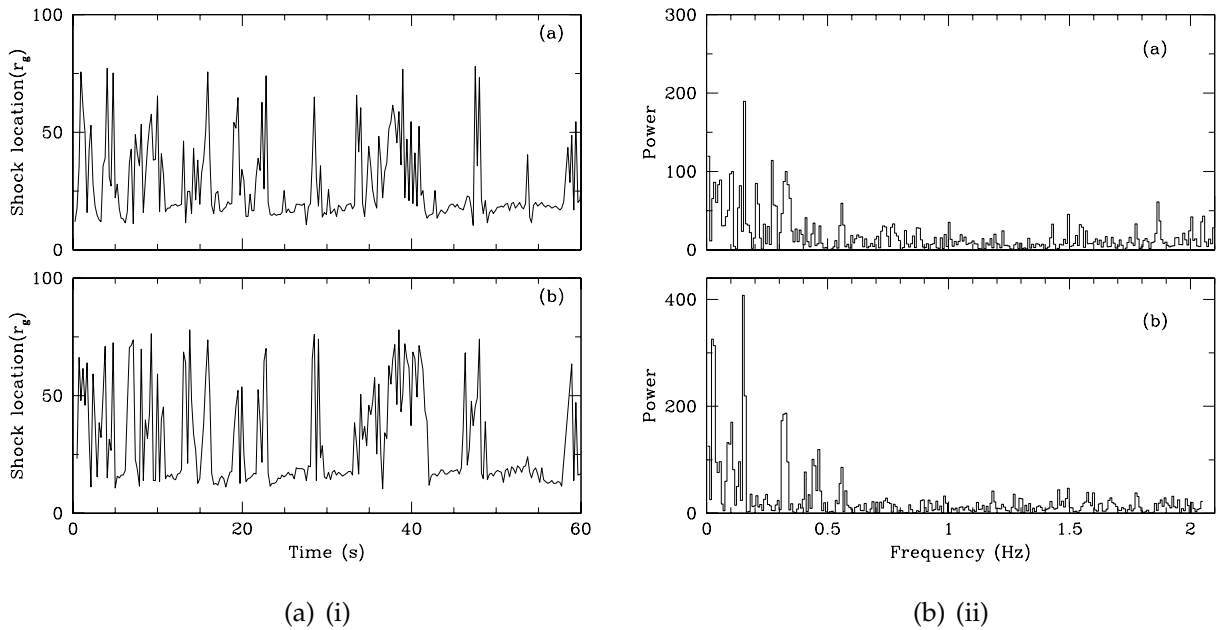


Figure 4.6: Time variation of shock location for two quadrant flow with $\lambda = 1.6$ angular momentum and their respective power density spectra. Group (i) shows the shock location variation in upper (a) and lower (b) quadrants. Group (ii) shows the power density spectra (PDS) of these locations. We see evidence of a prominent peak at $\sim 0.16\text{Hz}$ in both the cases and a harmonics at $\sim 0.32\text{Hz}$.

cation variation in upper and lower quadrant respectively. From these plots it is evident that, since for lower angular momentum case CENBOL is formed with a distinct shape (with repeated formation and deformation of the CENBOL) and the flow is less turbulent as compared to the higher angular momentum case, the time variation of shock location for the low angular momentum case has some periodicity in it. But as the angular momentum is increased, the flow becomes more and more violent and the CENBOL tends to take a very complex shape, the time variation of the shock location becomes more chaotic and from the Figures it can be concluded that as the λ increases, the shock tends to oscillate around a larger mean value.

Figures 4.6(ii)-4.8(ii) depict the power density spectrum (PDS) of the time variation of the shock location. In panels (a) and (b) PDS of the upper and low quadrant shock locations are shown. For low angular momentum case $\lambda = 1.6$, the power density spectrum has two distinct peaks at $\sim 0.16\text{Hz}$ in both the cases and

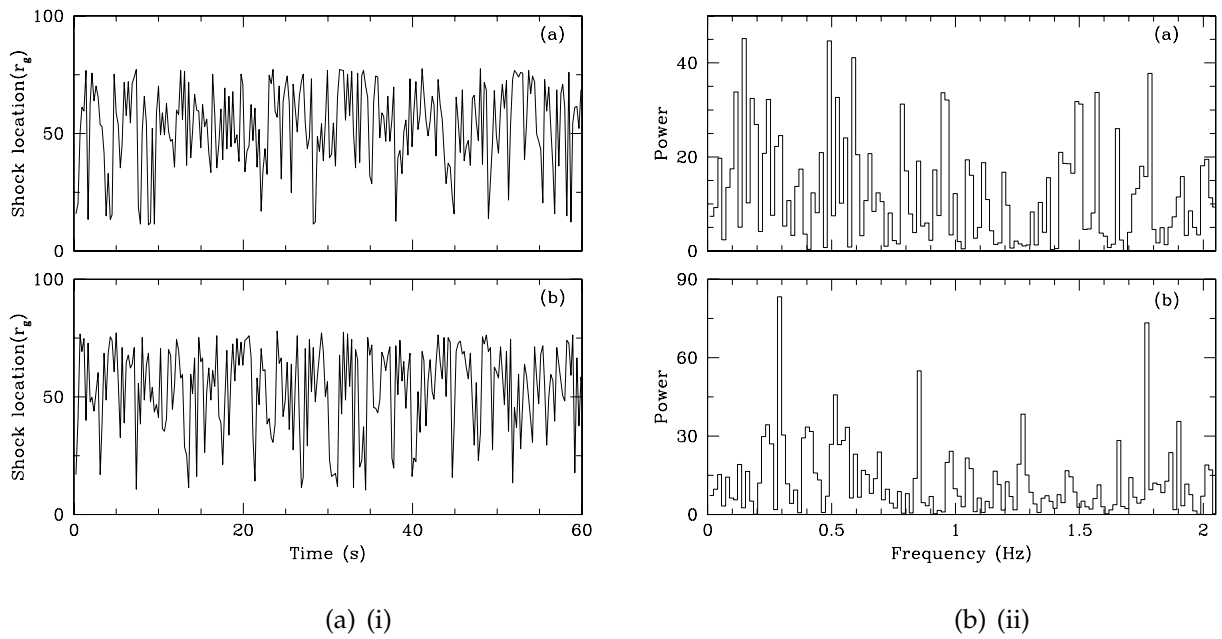


Figure 4.7: Same as in Fig. 4.6 for $\lambda = 1.7$. Note that the shock oscillates around a larger mean location, though the symmetry in upper and lower quadrant is lost. The power density spectra have several peaks and the oscillation is more chaotic.

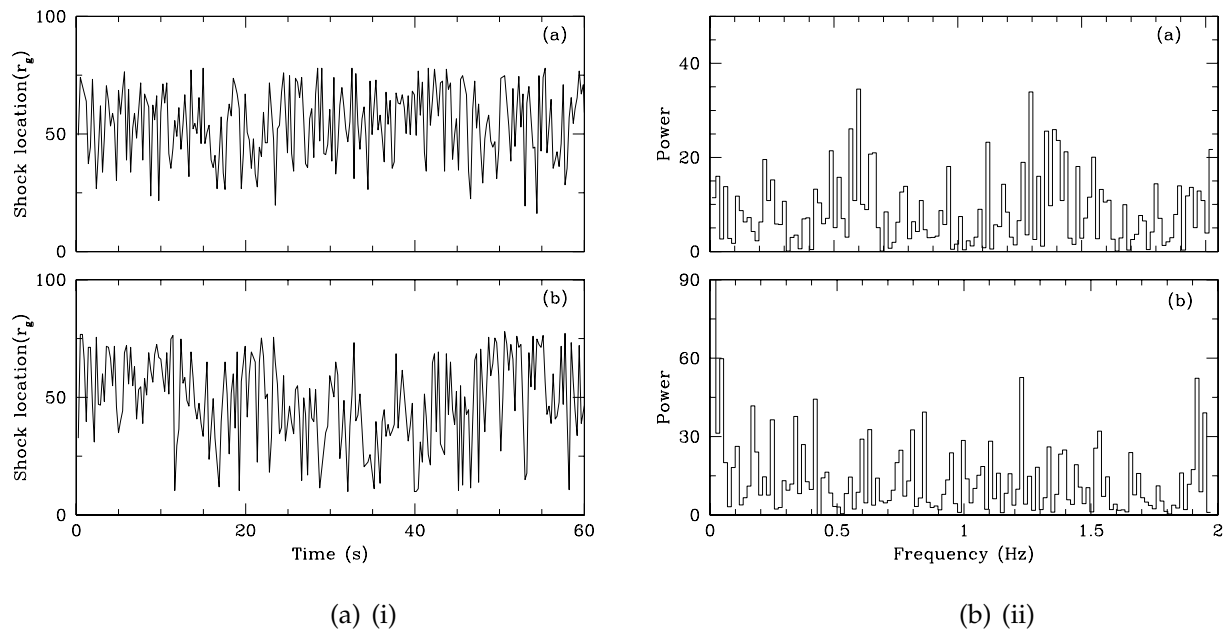


Figure 4.8: Same as in Fig. 4.6 for $\lambda = 1.8$. Note that the shock oscillates around a mean location similar to what we observed for $\lambda = 1.7$, perhaps due to the post-shock turbulence. The symmetry in upper and lower quadrant is lost. The power density spectra have several peaks and the oscillation is more chaotic.

a harmonics at $\sim 0.32\text{Hz}$ but as the angular momentum is increased to 1.7 and 1.8 the PDS of the shock locations has several peaks as the oscillation becomes more and more chaotic.

In the present chapter, we studied whether the CENBOL truly stays symmetric with respect to the equatorial plane. For this, we removed the reflection symmetry generally imposed on the equatorial plane. We inject matter just in first and the fourth quadrants. We find that for lower centrifugal force i.e., for lower angular momentum, the CENBOL stays symmetric, however a vertical oscillation sets in which turns out to become more violent as the specific angular momentum increases. This is superimposed with a horizontal oscillation. We likewise find that the outflow rates from the two quadrants are different: The quadrant in which the CENBOL is tilted, has a higher rate. The rates in the two quadrants are found to be anti-correlated. Giri & Chakrabarti (2013) and Giri et al. (2015) have demonstrated that an injected sub-Keplerian flow can re-distribute the angular momentum supplied at the outer boundary and forms a Keplerian disc when sufficient viscosity (greater than the critical value) is supplied, giving rise to the two component advective flow discussed theoretically by Chakrabarti (1990) and Chakrabarti (1996) and used in calculating the spectra in Chakrabarti (1995), Chakrabarti (1997) and Chakrabarti & Titarchuk (1995). The conclusions drawn in this chapter based on the simulation results produced here will act as the basis of the work which includes viscosity and radiative cooling as well as magnetic fields. These will be discussed in the next chapters.

Chapter 5

Non magnetized viscous flow

Chakrabarti (1990a,b), Chakrabarti (1996) (see also, Chakrabarti and Das, 2001) showed that there exists a critical value of viscosity parameter (α) which decides whether standing shocks may form in a transonic flow. If the viscosity parameter is greater than the critical value, the shock front will move outward and the disc would become Keplerian component and subsonic. In Giri & Chakrabarti (2012), this was demonstrated for a flow which have a reflection symmetry along the equatorial plane. Radiative process plays a key role in shaping up the flow geometry, since, for an optically thick flow, the radiation will not leak out and flow is puffed up. Though viscosity transports angular momentum, we need a proper cooling process in order to create a standard Shakura & Sunyaev (1973, SS-73) type disc. Chakrabarti 1995, Chakrabarti (1997, and references therein) based on theoretical solutions for inviscid and viscous transonic flows (Chakrabarti 1989, 1990, 1996) showed that an accretion disc, in general, will consist of two components: one is a subsonic Keplerian disc surrounded by a sub-Keplerian advective flow. This latter flow is puffed up and forms CENBOL which will act as the Compton cloud where soft photons coming out of the Keplerian disc will be scattered and energized to become hard photons. Soft photons constitute the black body part of the spectrum and hard photons give the power law tail. This Two Component Advective Flow model comes from the hydrodynamics itself and thus it can explain the spectral and timing properties (QPOs, time lags etc.) accurately. With suitable modifications, this model can also be extended to study spectral properties of Neutron stars (Bhattacharjee et al. 2018, 2019) and AGNs (Nandy et al. 2019). Giri & Chakrabarti (2013) simulated a two component advective flow using hydrodynamic simulation by appropriate choice of vertical viscosity variations. In this ground breaking work, the flow is injected only through the upper quadrant, ignoring the asymmetry of the flow with respect to the equa-

torial plane.

In the previous chapter, we have shown that if the reflection symmetry along the equatorial plane is not enforced i.e., if the CENBOL is allowed to have a vertical oscillation as well for an inviscid flow it will retain the flow symmetry for low angular momentum cases but as the angular momentum is increased, the flow becomes very turbulent influencing the outflow properties. Since according to Chakrabarti (1989, 1990a,b) for a lower angular momentum flow, matter can be advected even without efficient angular momentum transport, we have introduced viscosity and two types of radiative cooling depending on the optical depth in the flow with higher angular momentum. Our goal was to see (i) whether Keplerian disc is formed and (ii) whether the flow remains turbulent after introducing viscosity and cooling when matter is injected through both the quadrants. In this chapter, we will discuss these questions.

5.1 Simulation Procedure:

All the necessary governing equations and the procedure to implement two types of radiative cooling has already been discussed at length in the chapters 2 and 3 so we will not repeat them here. In order to choose the viscosity parameter α , we followed the prescription used in Giri & Chakrabarti (2013) and modified it to generate the α -profile for a two quadrant flow. Our choice was decided by what happens in a dwarf novae disc, where matter is accreted due to high viscosity in the equatorial plane region. A similar configuration is applicable to black holes also where in the equatorial region, the angular momentum transport is maximum and thus α required is also highest. We use the α profile for two quadrant flow as,

$$\alpha = \alpha_{max} - \alpha_{max} \left(\frac{|z|}{r_{max}} \right)^\delta \quad (5-1)$$

where $r_{max} = r_{out} = 200 r_g$ and $-200 \leq z \leq 200$ and $\delta = 1.5$. We have plotted the z variation of α in Fig 5.1. From the eqn 5.1 it is clear that when $z = 0$ i.e, at the equatorial plane the α value is maximum. The maximum value of α is chosen to be greater than the critical value of viscous parameter in order to facilitate an efficient way of angular momentum transport. Here, we have considered $\alpha_{max} = 0.012$. The simulation set up is already explained in chapter 4 in details. Here, we take the grid number as $N_r = 512$ and $N_z = 1024$. Thus the grid size is $0.39 r_g$. We have added two types of coolings, depending on the optical depth

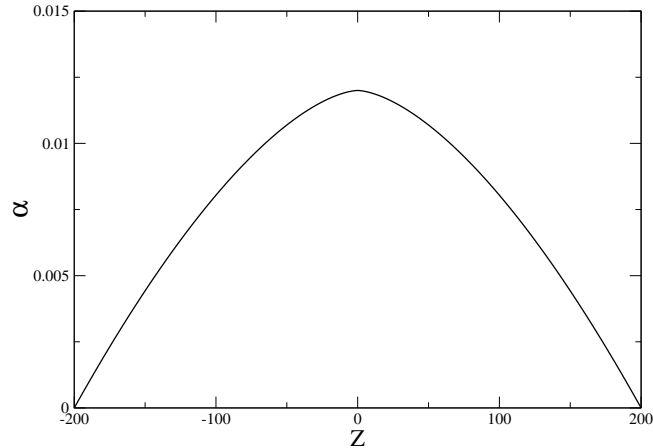


Figure 5.1: Variation of viscosity parameter (α) along the z -direction. Here, $\alpha_{max} = 0.012$.

of the flow which we calculate dynamically. A stellar black hole of mass $10M_{\odot}$ is placed at the origin of the co-ordinate system which we choose to be cylindrical. In order to mimic the horizon of the black hole we place an absorbing boundary at $1.1 r_g$. Here, we used a pseudo-Newtonian gravitational potential. We run the simulation for several hundreds of dynamical time scale which in reality correspond to a few seconds in physical time.

5.2 Simulation results

We consider that the flow is in vertical equilibrium (Chakrabarti 1989) at the outer boundary which enables us to calculate the injection velocity and sound speed of matter at the outer boundary. The matter is injected at all the radial grids. We ran our simulations up to 95s which is a few hundred times of the dynamical timescale. By this time, all the transient phases of the simulations are over. We perform a two dimensional simulation of the flow which spans in two quadrants of the $r - z$ plane of the cylindrical coordinate system. Here we have revoked the reflection symmetry along the equatorial plane. In the previous Chapters we have seen that the removal of reflection symmetry causes the shocks to have horizontal oscillations as well as the vertical oscillation. Also the flow becomes increasingly turbulent with angular momentum. Presently, we have added viscosity and a radiative cooling into the system and run the simulation. In Fig. 5.2

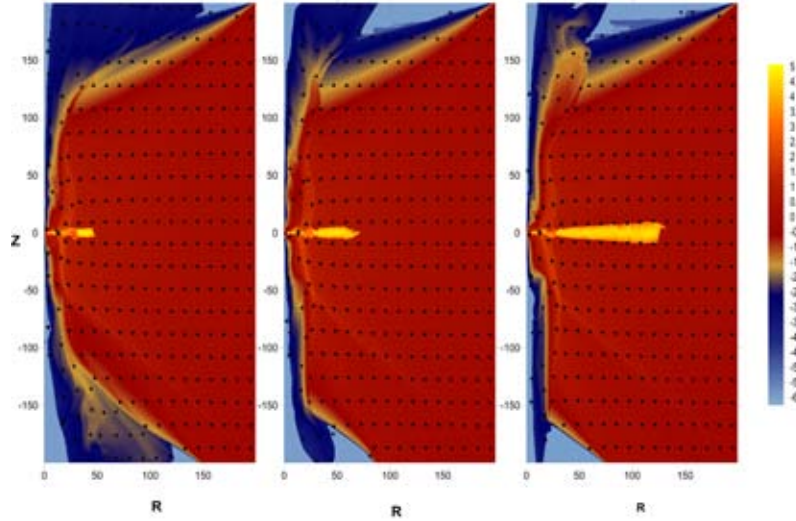


Figure 5.2: Density and velocity vector map to show the gradual formation of Keplerian disc at (a) $t = 9.6$ s, (b) 24.4 s, and (c) 95 s. Specific angular momentum is considered to be $\lambda = 1.7$.

we have plotted the density and velocity variation of the flow. Several snapshots of the simulation have been taken at different times. The first panel corresponds to simulation time of $t = 9.6$ s, the time in the second panel is $t = 24.4$ s, and the third panel refers to the simulation time of $t = 95$ s. The angular momentum (λ) and energy (ϵ) is chosen to be 1.7 and 0.001 respectively. The maximum value of the viscosity parameter α is chosen to be 0.012 which is greater than the critical viscosity parameter of the flow associated with the particular flow parameter. Since we have implemented radiative coolings according to the optical depth of the flow, we considered a critical value of optical depth (τ_c): $\tau_c = 10.0$ which is calculated using eqn. 2-67. If the optical depth of the region $\tau < \tau_c$, we will have a power law type cooling described in eq. 2-66 where the cooling index (β) is chosen to be 0.6 and if $\tau \geq \tau_c$, the black body type cooling is implemented (see 2-68). In fig. 5.3 we show the specific angular momentum distribution on the equatorial plane region and have compared with the Keplerian distribution. The dashed curve represents the theoretical Keplerian distribution which goes as $\sim r^{\frac{1}{2}}$ and the solid curve represents the radial distribution of specific angular momentum obtained from the simulation of matter flow with viscosity and radiative cooling. The panels are drawn for the times same as those of the snapshots in fig. 5.2. The time stamps are $t = 9.6$ s, 24.4 s, and 95 s respectively. From these three

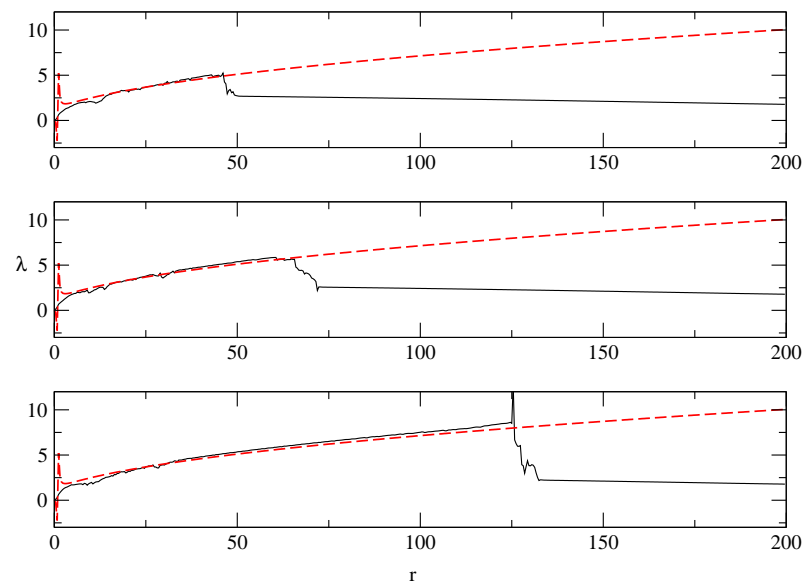


Figure 5.3: A comparison between specific angular momentum distribution at the equatorial plane with the Keplerian angular momentum distribution. Injected angular momentum is 1.7 and figures are drawn for different times as specified in fig 5.2.

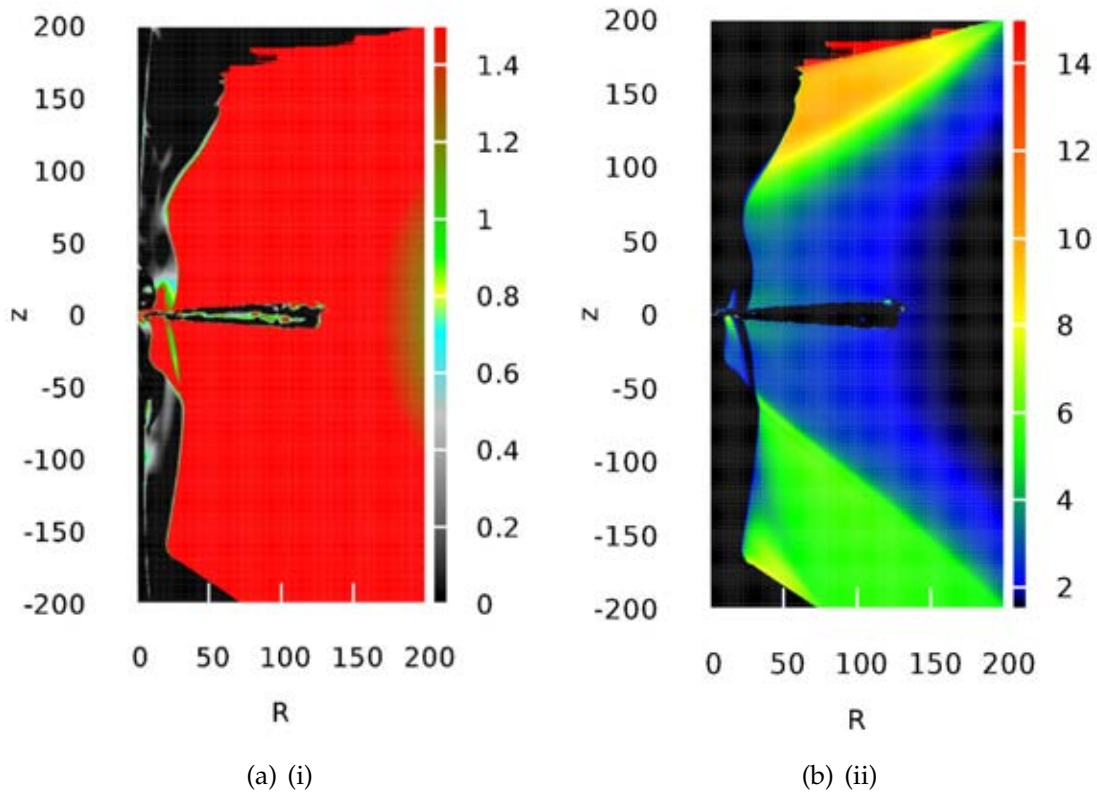


Figure 5.4: Mach number distribution for the subsonic (i) and supersonic (ii) flow.

panels it is evident that the specific angular momentum obtained from the simulation coincides with the Keplerian distribution. From this, we can infer that with viscosity and cooling, the injected flow of angular momentum of 1.7 the angular momentum is transported efficiently at the equatorial plane as expected and the Keplerian disc is formed gradually and also the angular momentum distribution attains Keplerian value till the point up to which the Keplerian disc is formed. The matter in the Keplerian disc region is sub-sonic and only at the region between horizon and the inner sonic point the matter will be supersonic. This can be seen in figs. 5.4 and 5.5 where we have plotted the Mach number distribution in both the components. In fig. 5.4 the Mach number range is set from 0 to 1.4 and in fig 5.5 this range is 1.5 to 15. The first figure corresponds to a subsonic regime which represents the Keplerian disc and second figure corresponds to the generally supersonic regime. In previous few figures we have seen that with sufficient amount of viscosity and with proper implementation of radiative cooling, the turbulence seen in the inviscid flow (see, Chapter 4) are smeared out completely and

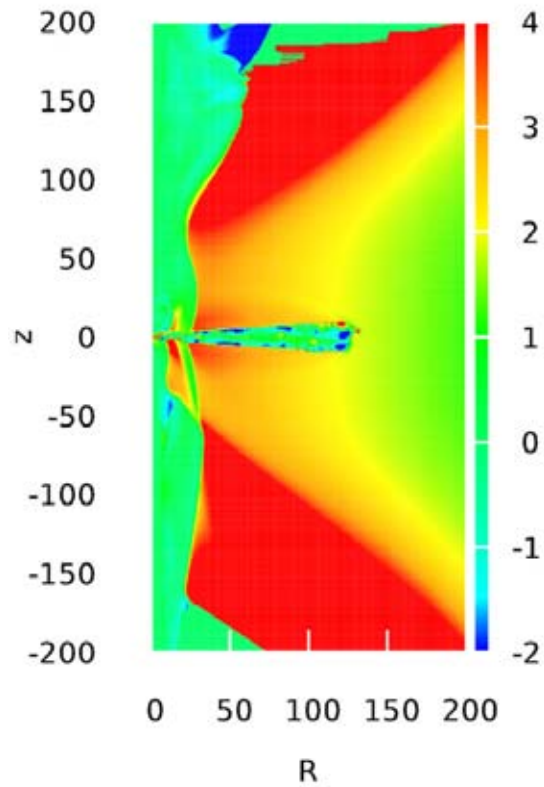


Figure 5.5: Temperature variation of the fluid flow. Temperatures are written in KeV unit. Here, we have plotted $\log_{10} T$. This snapshot of the temperature variation is taken for time $t = 95$ s

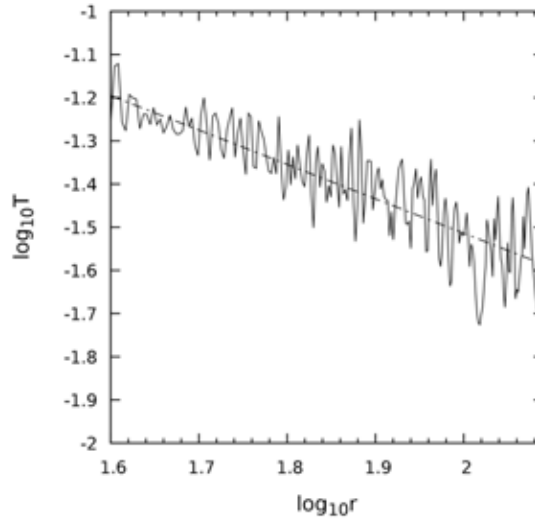


Figure 5.6: Radial variation of the temperature of the simulated Keplerian disc. Temperatures are written in KeV unit. Here, we have used $\log - \log$ scale. The index γ of the radial variation of temperature $T(r) \sim r^{-\gamma}$ is 0.797

flow becomes stable for higher angular momentum case as well and also forms a Keplerian disc at the equatorial plane region same as Giri & Chakrabarti (2013). In next few figures we shall demonstrate that not only angular momentum but temperature distribution also matches with the Keplerian disc. In fig. 5.6 we have plotted the spatial variation of $\log_{10}(T)$ in KeV. It is evident from this figure that due to black body type of cooling in the equatorial region where the disc is formed, this region is colder than that of the rest of the sub-Keplerian flow which surrounds the Keplerian component. After the shock region the Keplerian and sub Keplerian components get mixed up before entering the black hole. In fig 5.7 we have plotted the radial variation of vertically averaged temperature of the Keplerian disc in log scale. In Shakura & Sunyaev (1973) it was shown that for a thin Keplerian disc, the temperature varies as $\sim r^{-\frac{3}{4}}$. Since we also have employed $\sim T^4$ type cooling in Keplerian disc region we also should find similar type of radial variation. In fig. 5.7 we have used $\log - \log$ scale and have fitted it with a straight line with proper initial guess. We have the best fit for a straight line with slope $m = -0.797$. Thus the temperature of the simulated Keplerian disc varies with r as $\sim r^{-\gamma}$ where $\gamma = 0.797$. This almost matches with the theoretical slope.

Chapter 6

Magnetized accretion flow

6.1 Introduction

A clear comprehension of formation, acceleration, and collimation of radio jets has been eluding the astrophysicists for decades. Lynden-Bell (1978) proposed a vortex like structure near the axis of a geometrical thick disc. It was conjectured that some of the disc matter is pushed away and accelerated along the axis due to super-Eddington luminous radiation in that region. This paved the initial direction to the theoretical approaches which attempted to explain collimation and acceleration of the jets. In subsequent years, many theoretical works have been done by various groups and a large body of literature is available that explores many aspects of the mechanisms related to the jet collimation and acceleration. For example, Fukue 1982, Chakrabarti 1986 attempted hydrodynamic processes; Blandford & Payne 1982, Chakrabarti & Bhaskaran 1992 discussed jet collimation and acceleration by hydro-magnetic processes; Camenzind 1989; Heyvaerts & Norman 1989 and Lovelace 1976 discussed collimation of jets by magnetic fields; Eardley & Lightman 1975, Galeev et al. 1979, Coroniti 1981, Shibata et al. 1990, Chakrabarti 1990a discussed the effects of buoyancy and shear amplification on the magnetic flux tubes in the paradigm of thin accretion disc. Study of dynamics of toroidal magnetic flux tube in the setting of context of a thick accretion disc has been done by Chakrabarti & D'Silva (1994a, henceforth CD94) and D'Silva & Chakrabarti (1994b, henceforth DC94) where they demonstrated the dynamics of toroidal flux tubes injected into the thick disc. They studied the effects of various flows and flux tube parameters. So far, no study of the flux tube behavior and its possible effects on the flow dynamics and on the jet formation a time dependent, geometrically thick transonic flow has been performed.

In the present chapter, we extend our previous studies to time dependent

flows and investigate the dynamics of flux tubes inside a time dependent hydrodynamic flow. We find dependence on various flow parameters such as, angular momentum, flow energy and most importantly the flux tube parameters. We also study how the flux tubes will aide in the collimation and acceleration of jets/outflow. We first start an inviscid disc as described in chapter 4 and then build up our study for a viscous flow.

6.2 Computational procedure

In order to continue with our study, along with the hydrodynamic equations and equations of motion of the flux tubes we need to use the equation to compute magnetic buoyancy factor (M) and the area increment factor (A) with the constraint that the flux tubes move adiabatically inside the accretion flow, i.e., no heat is exchanged between the flux tube and the surrounding fluid. The entropy inside stays constant while the flux tubes navigated inside the disc. Following the calculations done in chapter 2 utilizing aforementioned assumptions we get an expression for ρ_i/ρ_e (CD94),

$$k_1 \left(\frac{\rho_i}{\rho_e} \right)^{4/3} + k_2 \left(\frac{\rho_i}{\rho_e} \right)^2 - 1 = 0, \quad (6-1)$$

where,

$$k_1 = \frac{(1 - \beta_e M_0)}{(1 - M_0)^{4/3}},$$

$$k_2 = \beta_e \frac{M_0}{(1 - M_0)^2} \left(\frac{T_e}{T_{e,0}} \right)^2 \left(\frac{\xi \sin \theta}{\xi_0 \sin \theta_0} \right)^2.$$

From this condition we get ρ_i/ρ_e and subsequently the magnetic buoyancy factor (M). Here, ρ represents density of the fluid and the subscripts i and e refer to internal and external values of the physical quantities. In our simulation, we considered an inviscid thick advective disc around a black hole of mass $10 M_\odot$. To compute within a sensible time frame, we consider a small disc with the outer boundary at $200 r_g$. The real size of the disc is significantly bigger than what we are assuming. Since we are keen on studying the generic behavior of the magnetic flux tubes near the centrifugal barrier we will proceed with these typical parameters all through our simulations. Second, at this distance, all the random flux tubes entering far away from the central object are thought to have a toroidal

geometry. We inject these flux tubes from the radial grid boundary, i.e., at the $200 r_g$ close to the equatorial plane. We consider an inviscid disc with the goal that the angular momentum remains the same all through. The specific energy of the injected matter remains constant since we have not considered any radiative cooling process. For the detailed portrayal of the numerical setup for the disc simulation, refer to Chapter 3 and also section 4.2 (see also Deb, Giri, Chakrabarti 2016). Schemes, essential properties of the code, and test outcomes are discussed in §3.6. For more explicit discussion refer to Harten (1983). In a transonic flow there are just two free parameters: angular momentum and specific energy. This is less than any other solutions, in light of the fact that the sonic point condition takes out the need of providing any more free parameters. With these two parameters, we know both the sonic points of the flow, the shock location and every single other property of the flow. We supply just λ and specific energy as the boundary condition. Angular momentum is characterized as, $\lambda = rv_\phi$ in the unit of $2GM/c$. The values taken are less than the marginally stable λ . Somewhat higher than the marginally stable value is likewise permitted (till marginally bound value of 2.0) so as to have a sonic point. In Giri and Chakrabarti (2013) it has been demonstrated that in presence of viscosity, beginning from angular momentum lower than λ_{ms} , Keplerian disc is formed. Along these lines, for inviscid case, we picked $\lambda < \lambda_{ms}$ so the flow essentially remains sub Keplerian. Total energy(ϵ) of the injected stream is chosen to be less than the rest mass energy of the electron. We use injected matter having constant angular momentum of (i) $\lambda = 1.6$, and (ii) $\lambda = 1.7$ and for every one of these cases we utilize the specific energies $\epsilon = 0.001, 0.002, 0.006$. We also used the same set up for a flow with viscosity. The magnetic flux tubes at the outer boundary are injected close to the central plane ($\theta = 89^\circ$) with an initial magnetic buoyancy (M_0) which we calculate by taking the ratio between the magnetic pressure and external gas pressure. We inject the flux tubes after the flow achieved an equilibrium configuration so that all the transient effects are removed. We couple the equation of motion for the tube with the hydrodynamic TVD code. We change the source term as given in 2-69 by including Lorentz force term. This will include the effects of the flux tube on the fluid. The input parameters, in particular, angular momentum and total energy gives a unique injection velocity and sound speed at the outer boundary. These together with a density at the outer boundary (scaled as unity at the equatorial region) gives the accretion rate. In a non-dissipative flow, the outcome does not depend on the density explicitly. We compute the density, velocity, pressure and temperature profiles utilizing time dependant TVD code in light of the

boundary conditions and the equation of state. These flow parameters' values are utilized as the input parameters to calculate the dynamics of a flux tube inside the disc since the drag, magnetic buoyancy, magnetic tension etc. depend on the surrounding in which the tube is moving. Those in turn are put in the eq. 2-71-2-73 and we numerically compute them with the help of the fourth order Runge-Kutta technique (Deb, Giri, Chakrabarti 2017).

6.3 Inviscid magnetized disc

In earlier works (CD94 and DC94), the toroidal flux tube was inserted into a rotating thick accretion disc (with radial velocity superimposed) for different angular momentum distribution where the distribution has the form of $\sim R^n$ where R is the axial distance and n is a positive constant according to the stability criterion under the axisymmetric perturbation. $n = 0$ implies that the angular momentum is constant which mimics an inviscid case and $n \neq 0$ implies that angular momentum varies with different axial distance inside the disc. It was seen in their calculation for different point of injection the flux tubes emerges from different parts of the discs and these positions of emergence also depend on the initial cross sectional radius. They also showed that for proper entropy condition flux tubes oscillate inside the disc creation the condition of flux storage. In our work (see Deb, Giri, Chakrabarti 2017), we proceed in the same line but we inject the flux tubes at the outer boundary as in a real situation these flux tubes are accreted along with the matter from the companion and also for a time dependent inviscid and viscous disc and also focus on the effect of magnetic flux tubes on collimation and acceleration of jets/outflows. For this purpose, we carried out simulations for various cases and obtained significant results. In the sections below we shall present those results (Deb, Giri, Chakrabarti 2017) and discuss them.

6.3.1 Dynamics of magnetic flux tubes inside an advective flow

The trajectories of the flux tubes as computed in our simulations are plotted in $r - z$ plane. Figure 6.1 demonstrates the paths for the flux tubes inserted with initial cross sectional radii 0.001, 0.005, 0.01, & 0.1 r_g respectively discharged from the outer boundary with two distinctive flow energies, in particular, $\varepsilon = 0.001, 0.002$ (labelled). The purposes for picking such small cross sectional radii are clarified in the following discussion. To begin with, the axisymmetric flux tubes must

be made *ab initio* through shear and re-connection processes. So they are, by definition filamentary. Second, the cross sectional radii have to be chosen to be smaller with respect to the gravitational radius and the local pressure scale height so we can make the approximation that the variation of disc variables inside the flux tube is insignificant. Third, regardless of whether the filaments join and make tubes of larger cross-sectional area, the drag force will be too high and magnetic buoyancy will expel them from the disc much before they come nearer the black hole. We choose a low angular momentum flow with $\lambda = 1.6$. This would be the component which will make CENBOL close to the horizon. Since close to the axis, the centrifugal force is extremely high, a vortex like opening is formed which is called the "chimney" or the funnel divider (CD94). We have seen that before getting accreted by the black hole, a flux tube experiences oscillation near the black hole for a significant time and actually emerges in both chimneys. For both the energies, magnetic flux tubes having initial $\sigma < 0.1r_g$ emerge in the chimney. In our Figures, they appear to be going into the black hole, though in reality, they leave through the surface of the disc. Flux tubes with $\sigma \geq 0.1r_g$ are expelled out for the lower energy cases (Deb, Giri, Chakrabarti 2017). As we increase the energy of the flow, the flux rings have a tendency to oscillate as they will have more kinetic energy than the lower flow energy setup. Since this is an inviscid flow with constant angular momentum, Coriolis force will not have any influence in the dynamics and flux tubes will move inwards along the local pressure gradient (CD94).

We repeat the simulations for a similar variation of σ s and for larger angular momentum ($\lambda = 1.7$) and the energies $\varepsilon = 0.002, 0.006$ for which the dynamics of flux tubes is demonstrated in Fig. 6.2 and Fig. 6.3. We see that the flux tubes having $\sigma \leq 0.005 r_g$ will fall onto the black hole which is same as what we have found in Fig. 6.1 (see also CD94 and DC94). However contrary to the earlier case (Fig. 6.1), the flux tubes with $\sigma \geq 0.01 r_g$ will be expelled away. The flux tubes with distinct initial σ will take different times to complete their trajectories. In case of Fig. 6.1, for $\varepsilon = 0.001$, end times for flux tubes with injected initial cross sectional radii $0.001 r_g, 0.005 r_g, 0.01 r_g$ and $0.1 r_g$ are $t_{end} = 2.12, 2.7, 9.46, \& 5.8$ seconds individually and for $\varepsilon = 0.002$, $t_{end} = 2.2, 19.8, 20.4, 6.1$ seconds respectively. In the event of Figs. 6.2 and 6.3 this t_{end} is given as, for $\varepsilon = 0.002$, $t_{end} = 8.65, 9.2, 3.34, \& 5.77$ s, and also, for $\varepsilon = 0.006$, $t_{end} = 21.2, 22.3, 5.15, \& 12.64$ s respectively. It is seen from our simulation results that the flux tubes exhibiting oscillatory motion have longer residence time inside the disc. The infall time in the simulations is $\sim 0.6 - 0.7$ s

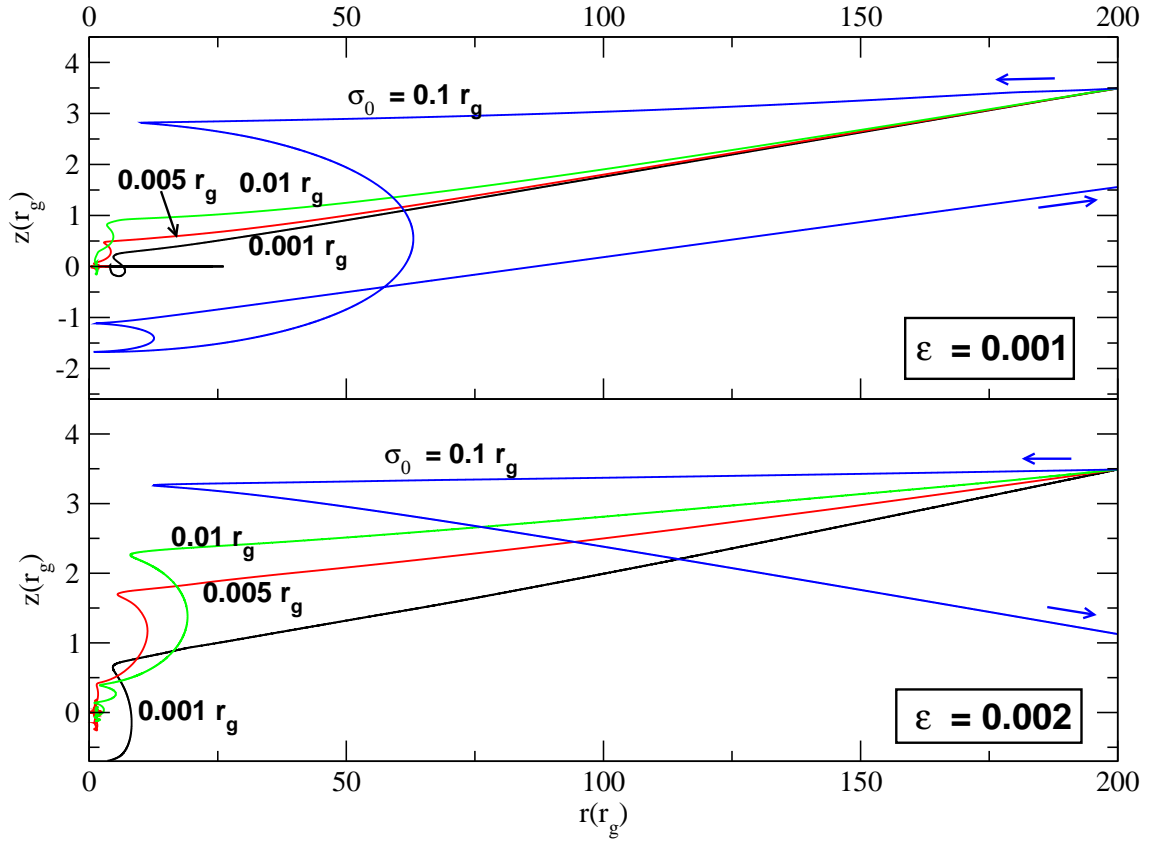


Figure 6.1: Trajectories of flux tubes injected from the outer boundary i.e., $r = 200r_g$ and $\theta = 89^\circ$ with zero initial velocity. Trajectories are in $r = R \sin \theta$ vs. $z = R \cos \theta$ plane. The trajectories are drawn for a flow with angular momentum $\lambda = 1.6$ and energies 0.001 (upper panel) and 0.002 (lower panel). σ is the cross sectional radii of the injected flux tubes. Here σ values are $0.001 r_g$, $0.005 r_g$, $0.01 r_g$ and $0.1 r_g$ (Deb, Giri, Chakrabarti 2017).

and it can be observed that the residence time of every flux tube inside the disc is a few times longer than this for all the cases we explored.

Figures 6.4 and 6.5 show the energy dependence of the trajectories of the flux tubes discharged in a flow having angular momenta 1.6 and 1.7 respectively. As we increase the energy, the flow turns out to be more turbulent and in this way it imparts more kinetic energy to the flux tubes. In Fig. 6.4 we have chosen the flow energy to be $\varepsilon = 0.001$ & 0.002 also, in Fig. 6.5 energy is $\varepsilon = 0.002$ & 0.006 .

As a flux tube moves toward the central object along the direction of the pressure gradient force it attempts to keep pressure equilibrium (i.e., an equilib-

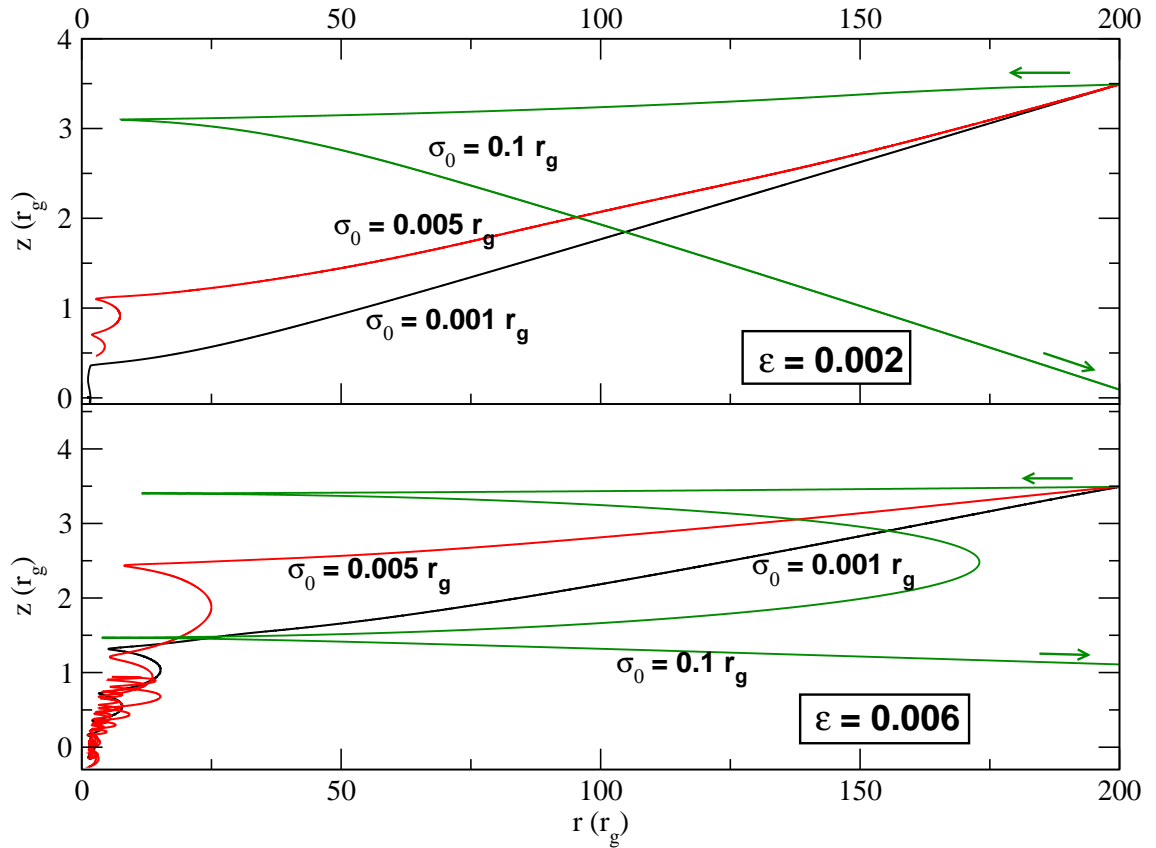


Figure 6.2: Trajectories of the flux tubes injected from the outer boundary i.e., $r = 200r_g$ and $\theta = 89^\circ$ with zero initial velocity. Trajectories are drawn in $r = R \sin \theta$ vs. $z = R \cos \theta$ plane. The trajectories are drawn for a flow with angular momentum $\lambda = 1.7$ and energies 0.006 (lower panel) and 0.002 (upper panel). σ signifies the cross sectional radii of the flux tubes for which the trajectories are drawn. Here σ values are $0.001 r_g$, $0.005 r_g$, and $0.1 r_g$ (Deb, Giri, Chakrabarti 2017)

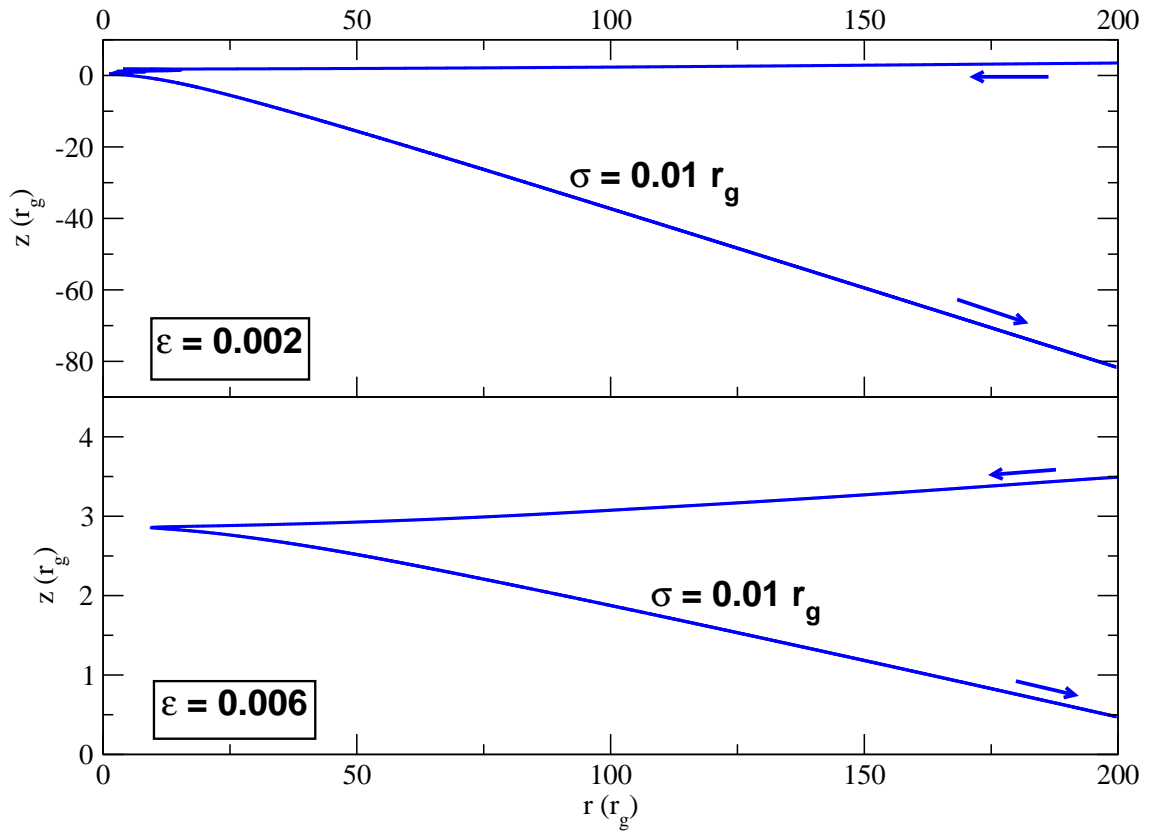


Figure 6.3: Trajectory of the flux ring having cross sectional radius (σ) $0.01 r_g$ released at $r = 200r_g$ and $\theta = 89^\circ$ with zero initial velocity. Angular momentum of the flow is 1.7 and the flow energies are $\varepsilon = 0.002$ (upper panel) and 0.006 (lower panel) (Deb, Giri, Chakrabarti 2017).

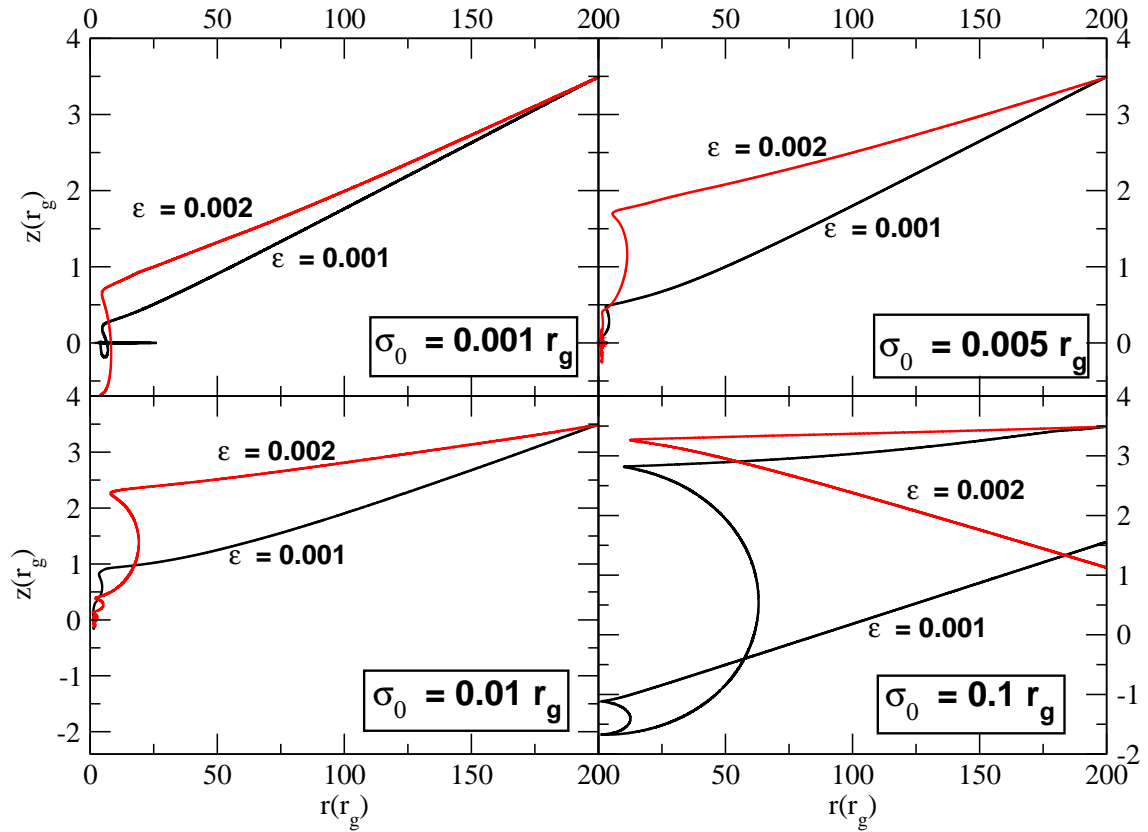


Figure 6.4: Trajectories of flux tubes having same σ but with different flow energies (marked) are drawn to demonstrate energy dependence of the trajectory of the flux tube inside the disc. $\varepsilon = 0.001$ & 0.002 are marked on the curves. Angular momentum of the flow is 1.6 (Deb, Giri, Chakrabarti 2017).

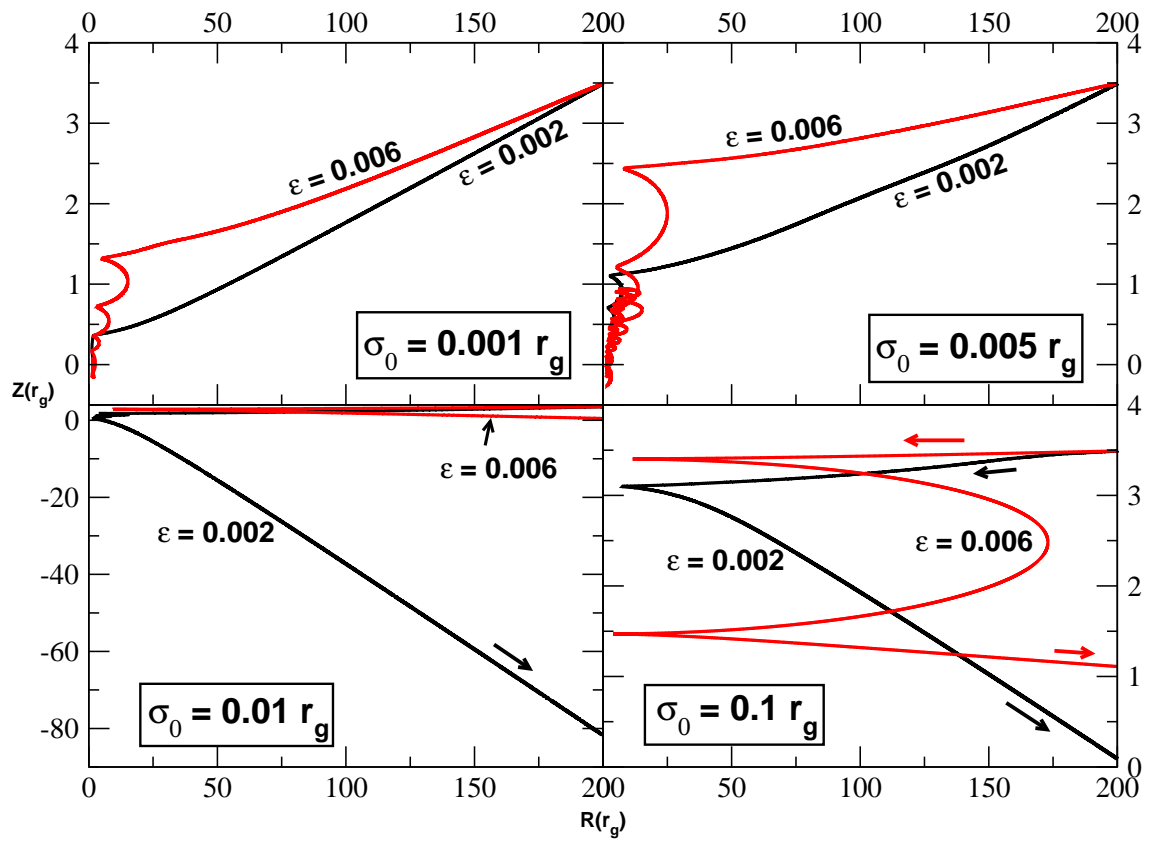


Figure 6.5: Same as in Fig. 6.4 except $\epsilon = 0.002$ & 0.006 and specific angular momentum of the flow is 1.7 (Deb, Giri, Chakrabarti 2017).

rium between the external gas pressure and internal gas pressure together with the magnetic pressure) with its immediate surroundings. When the flux tube is compressed during its journey towards the black hole, the internal density is increased and becomes heavier than the surrounding matter. However, closer to the black hole, density of the gas in the disc rises rapidly in the same direction. The outcome is that the inward journey of the flux tube is stopped and it is repulsed back. During the ensuing outward motion, the flux tube density drops faster than that of the surroundings and depending upon its direction, it can either escape or oscillate depending on the relative changes in the cross-section area and the disc density, which essentially control the buoyancy force. It has been discussed in CD94 and DC94 that as in the Sun, where the flux tubes are tied down in the region between the radiative and convective zones and at the base of the anchored flux tubes entropy gradient changes sign, similar anchoring as well as oscillation of flux tubes in case of accretion disc should be observed under similar conditions. In case of the Sun due to Parker's instability, the anchored flux tube emerged at the surface and likewise for an accretion disc, the anchored and oscillating flux tubes may also appear near the chimney because of a few perturbative effects causing magnetic activities (collimation as well as acceleration of jets) (see, CD94 and DC94). However, demonstration of aforementioned activities will require a three dimensional simulation which we planned to carry out in future. If the flow is turbulence free and laminar, the entropy remains constant throughout the flow but in our case because of tug-of-war between the gravitational force and the centrifugal force, the flow ends up turbulent close to the centrifugal barrier and could indeed, even form shocks which will create entropy. In Fig. 6.6, we plot the map of the radial component of the entropy gradient ($\vec{\nabla}_r$) at two unique times, $t \sim 4.06s$ and $6.33s$ separately. The angular momentum (λ) and specific energy of the flow are chosen to be 1.6 and 0.002 separately. In both the panels we see that the r component of the entropy gradient changes sign i.e., it goes from positive to negative and the other way around which creates a Solar interior like circumstance where the oscillating flux tube can be provided an anchorage by the entropy gradient. Figures 6.7 and 6.8 indicate variations of the cross sectional radius of the magnetic flux tubes with respect to the vertical distances the flux ring crosses. The panels in each Figure contain the σ -variations for distinct initial cross sectional radii (σ_0). The initial σ s for the plots are chosen to be $\sigma_0 = 0.001, 0.005, 0.01, \& 0.1r_g$. Every one of the Figures are drawn for different angular momenta and specific energies of the flow. Figures 6.7 and 6.8 have the λ and ε configurations as $(\lambda, \varepsilon) = (1.6, 0.002) \& (1.7, 0.006)$ respectively. The

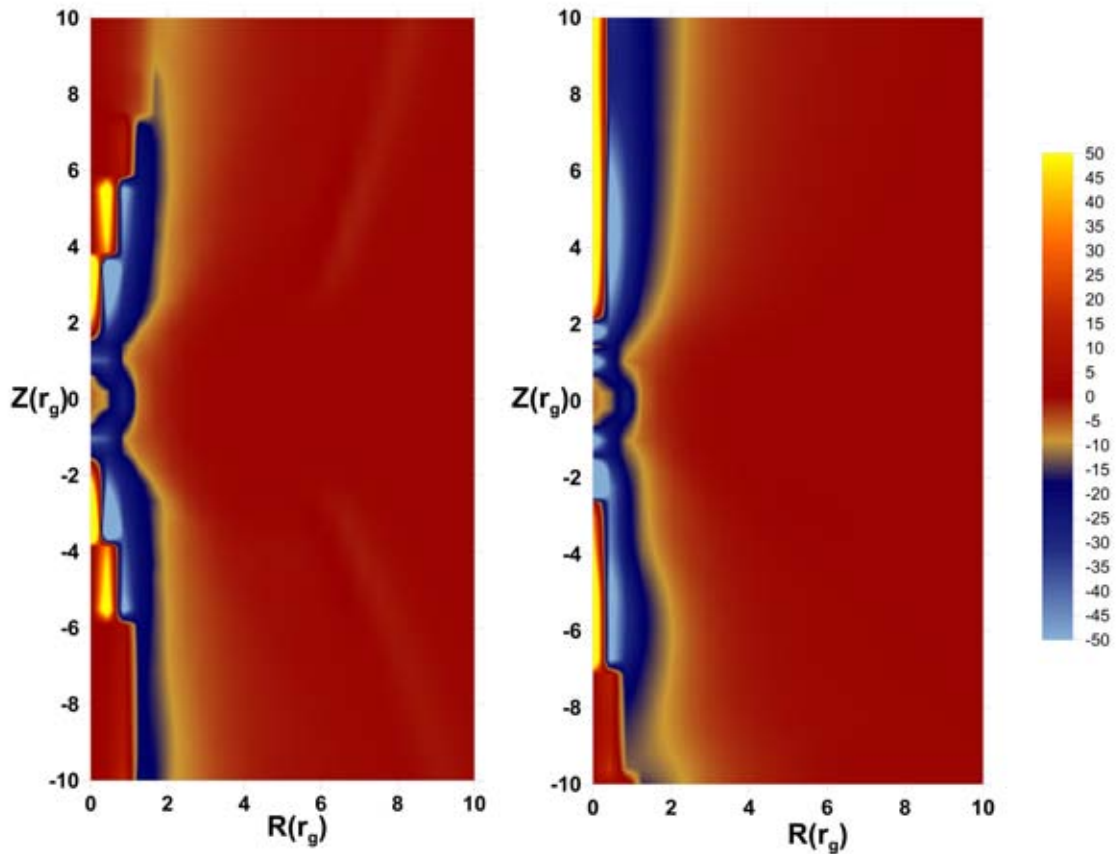


Figure 6.6: Time variations of radial component of the entropy gradient plot of the flow having angular momentum (λ) 1.6 and energy (ϵ) 0.002. Both the plot shows that the radial component of the entropy gradient switches sign from positive to negative and vice versa. This switching is responsible for providing an anchorage of the oscillating flux tubes and consequently may cause a corona like structure. Two plots are drawn at $t \sim 4.06$ & 6.33 s respectively (Deb, Giri, Chakrabarti 2017).

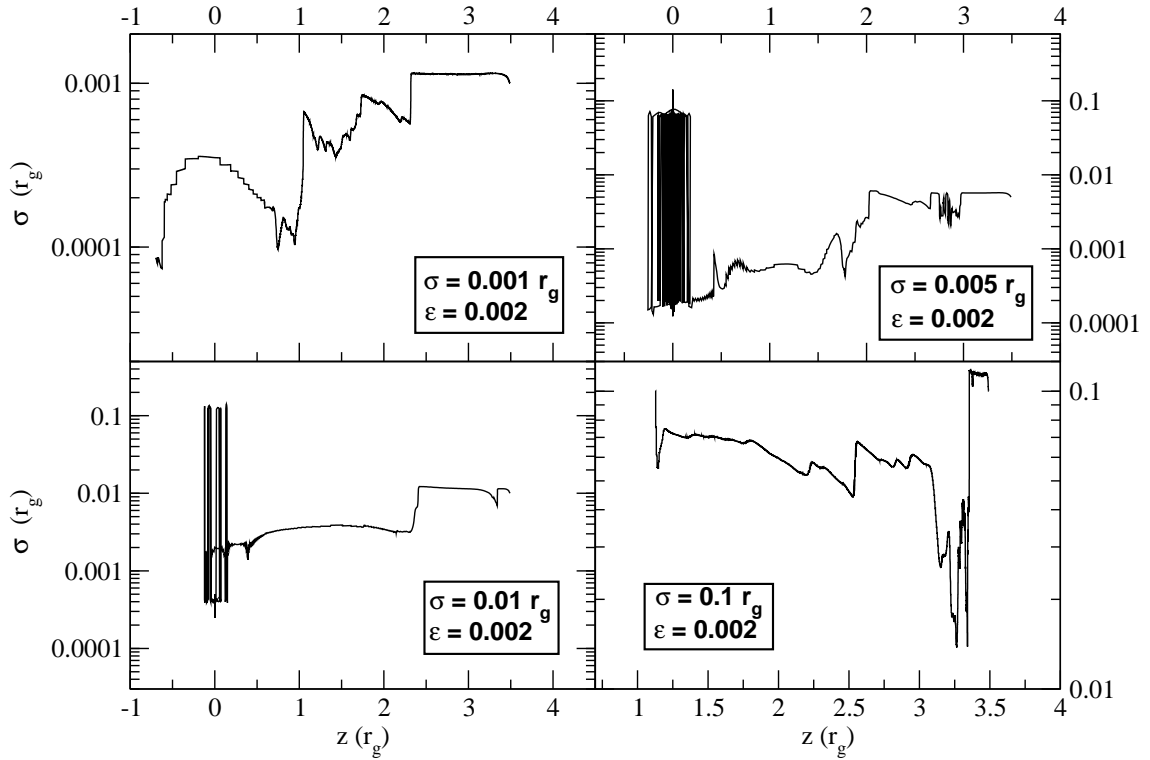


Figure 6.7: z variation of the radius of cross section(σ) of flux tubes released in an inviscid accretion flow with energy $\varepsilon = 0.002$ and angular momentum(λ) 1.6. Each panel shows the σ variation for different initial cross sectional radius. initial σ 's are $\sigma = 0.001, 0.005, 0.01, \& 0.1 r_g$ (Deb, Giri, Chakrabarti 2017)

divergence of the magnetic field should always be zero and the net flux of the toroidal flux tubes stays constant all through its trajectory. Accordingly, when σ diminishes, the magnetic field intensity (B) will increase ($B \propto \frac{1}{\sigma^2}$) and vice versa, influencing the buoyancy force.

In Figs. 6.7 and 6.8 it is seen that the cross sectional radius quickly increases and decreases hence subsequently to conserve the flux, the field will also change inverse squarely with the cross-sectional radius. Typically, at the point when the flux tube falls towards the central object the field intensity increases on an average (barring the oscillations) and because of this the magnetic pressure holds matter inside the tube and does not enable them to leak out sideways. Presently, There are two contradicting effects: While moving in, the flux increases and collimates the outflowing matter at the base of the jet. In any case, as the flux tube leaves along the axis its pressure decreases and its capacity to collimate diminishes, in

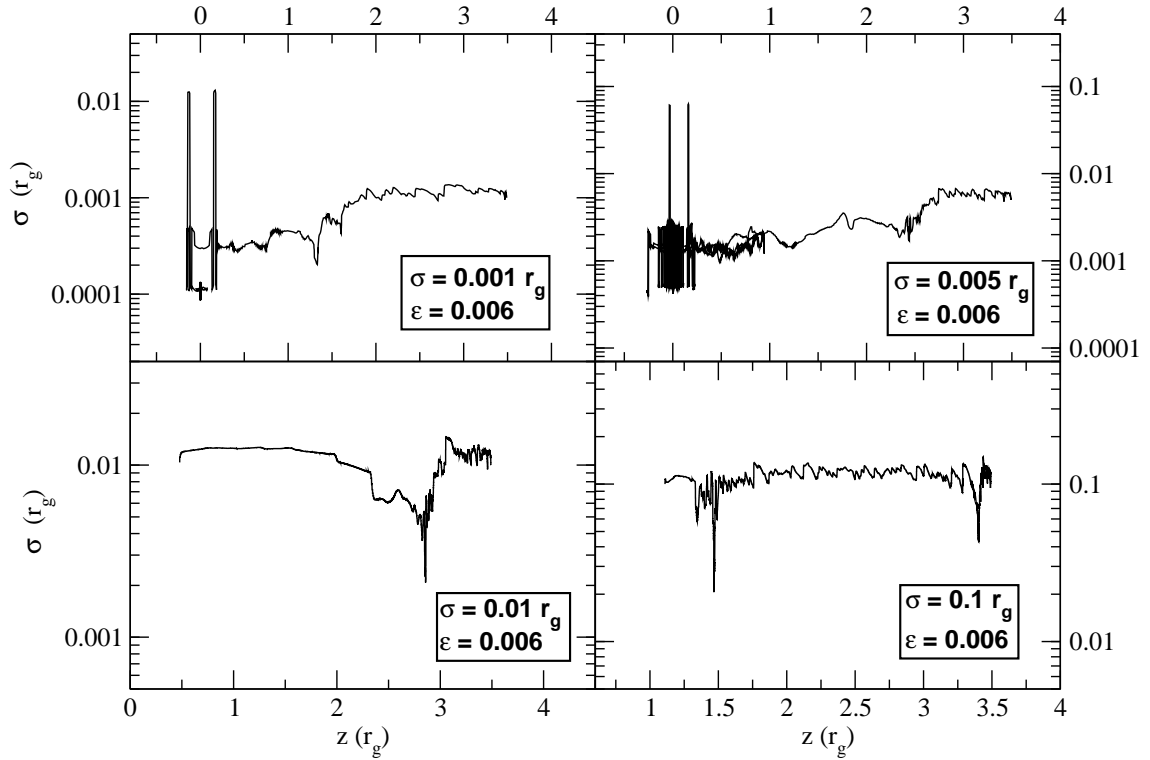


Figure 6.8: z variation of the radius of cross section (σ) of flux tubes released in an inviscid accretion flow with energy $\varepsilon = 0.006$ and angular momentum (λ) 1.7. Each panel shows the σ variation for different initial cross sectional radius. initial σ 's are $\sigma = 0.001, 0.005, 0.01, \& 0.1 r_g$ (Deb, Giri, Chakrabarti 2017).

spite of the fact that not to such an extent, since the jet itself is getting to be less dense as it extends out. We see an average effect instead of a sustained effect. If a huge number of such tubes could be infused, they would have a managed to render a sustained impact in collimating the jets.

6.3.2 Collimation and acceleration of outflows/jets

Jets can be classified into two broader classes: (a) persistent slow moving outflow which is continually ejected from the post-shock region and is collimated by the flux tubes on an average and (b) blobs of fast moving fluids which are squirted out because of a sudden collapse of the inward region of the disc. These are because of magnetic tension. In the event of a very strong magnetic flux tube, it would collapse towards its axis due to strong magnetic tension obliterating

the CENBOL and produce blobs of fluid by the so-called magnetic rubber band effects (b above). These blobs are quick moving in the first place. The type (a) outflows talked about above is accelerated implicitly: the collimation of the jets lessens its lateral width keeping its initial energy intact. The cross-sectional area increases gradually with distance (along the Z axis) and in this manner, they are accelerated.

In Figs. 6.10 and 6.11 we plot radial variation of the outflow rate acquired from both the quadrants, upper and lower. Here, we have made a comparative study of the outflow acquired from the flow with the magnetic flux tube infused in it with the flow that does not have any presence of the magnetic flux tube in it. The initial two rows show the outflow being collimated in the presence of the magnetic flux tube while the lower two rows imply fading of the collimating effects of the flux ring as it escapes from the computation box or falls onto the black hole. The black curve denotes the outflow rate for the magnetized flow and the red curve is for the non-magnetized case. Both the Figures (Fig. 6.10 and Fig. 6.11) are drawn for a similar set of σ ($= 0.001, 0.005, 0.01, 0.1 r_g$). We have run our simulation for $t \sim 23.76 s$ and for both the Figures each panel demonstrates radial variation of outflow rate at various time steps (see, Figs. 6.10 and 6.11). There was no particular reason behind picking these specific times. Our motivation solely stems from the fact that we wanted to demonstrate the impact of magnetic flux tubes on the outflow and how its presence or absence in the disc affects the outflow formation. So we covered the whole run time and exhibited four figures at each time where aforementioned effects were sufficiently prominent.

The angular momentum (λ) and the specific energy (ε) for Fig. 6.10 are chosen to be 1.6 and 0.002 respectively and for Fig. 6.11 the estimation of λ and ε are 1.7 and 0.006 respectively. In Fig. 6.10 (a-h), the collimation of the outflow is evident. The outflow rate for the magnetized flow has a sharp crest at around the region of $30 - 50 r_g$, whereas the outflow rate for the non-magnetized flow accomplishes a maximum value at around $50 - 90 r_g$. Again, the maximum value of the outflow rate is considerably higher, nearly 2 - 3 times higher than the maximum value of outflow rate for the non-magnetized case. As opposed to what we have found in Fig. 6.10, in the case of Fig. 6.11, in the panels (a-h) we see that the collimating effect is not as noticeable as what was seen in the previous case. In this case, the outflow rate for magnetized flow attains a maximum value of around $50 - 80 r_g$ which is more distant than what we have found in Fig. 6.10(a-h). The reason is that higher the angular momentum is, higher is the centrifugal force,

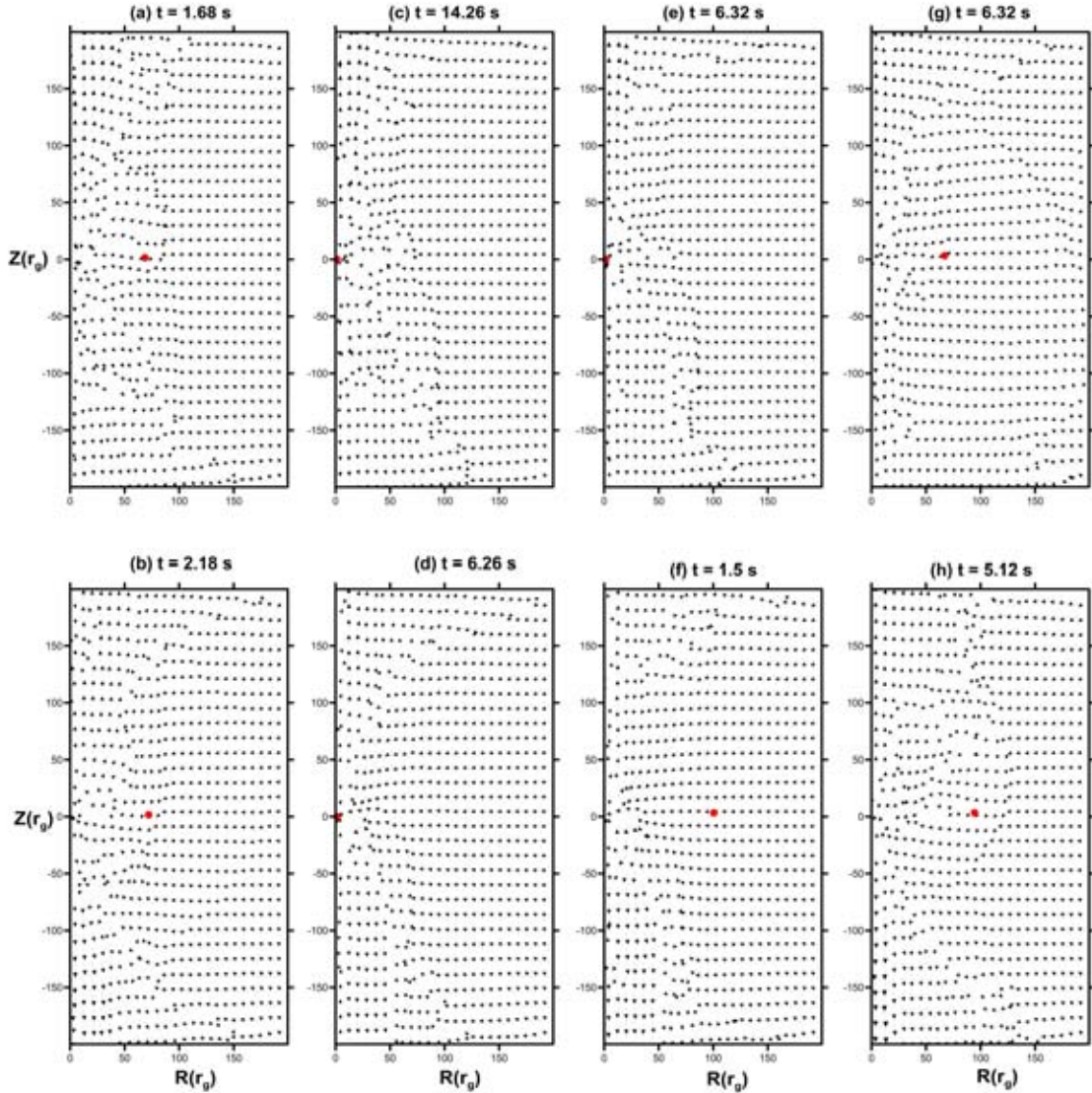


Figure 6.9: Velocity vector plot of the flow with magnetic flux tubes. (a,b), (c,d),(e,f), and (g,h) are velocity vector fields of the flow having magnetic flux tube of cross sectional radii 0.001, 0.005, 0.01, 0.1 r_g respectively. Angular momentum and specific energy are 1.6 and 0.002 respectively. The times specified are the same as in Fig. 6.10. The dots signify the position of flux tube at the respective times specified in each panel.

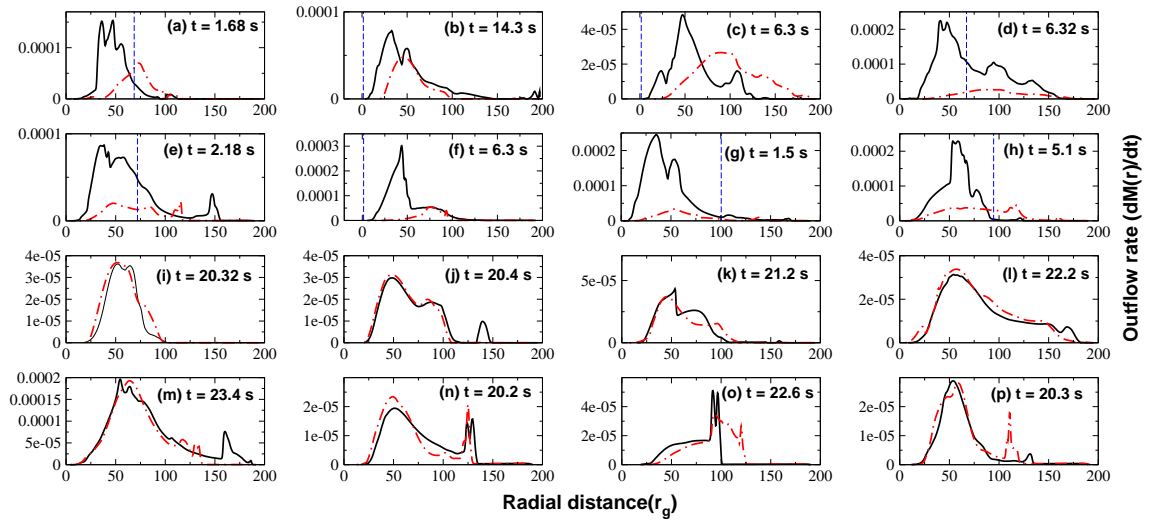


Figure 6.10: Radial distribution of the outflow rate (\dot{M}_{out}) of the flow having the specific angular momentum (λ) = 1.6 and energy (ϵ) = 0.002. The black solid curve represents the outflow rate for the flow with magnetic field and red solid curve (dot-dashed in hard copies) denotes the result in non-magnetic case. The upper two rows (a-h) of the plot show the collimation of the outflow from upper and lower quadrants respectively for different flux tubes with different σ . The lower two rows (i-p) depict the gradual reduction of the collimating effects once the flux tube has escaped or fallen into the black hole. The vertical dashed lines drawn in panels of first two rows depict the position of the flux tube at time for which the outflow rates are drawn (Deb, Giri, Chakrabarti 2017).

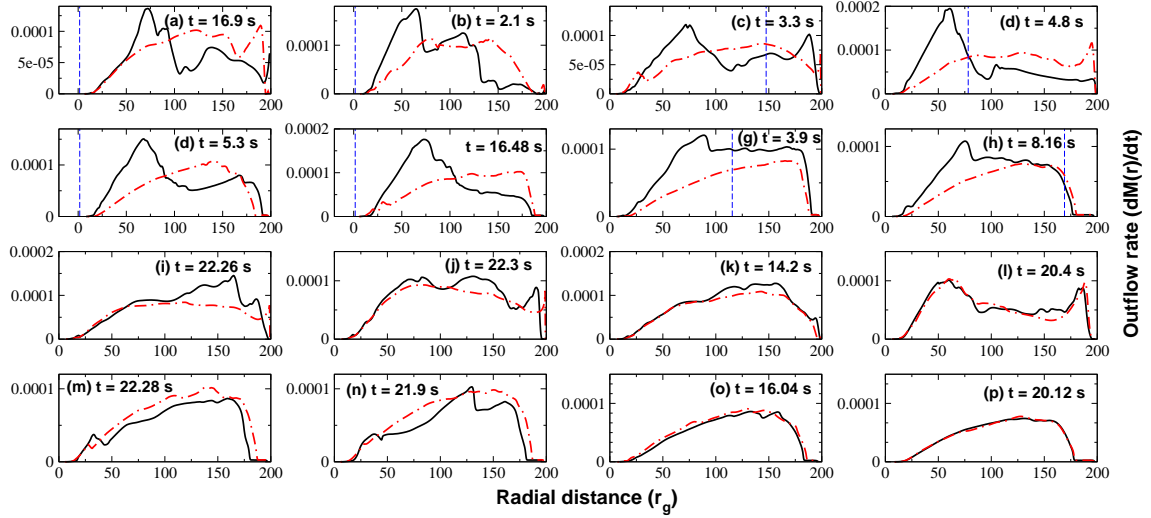


Figure 6.11: Same as Fig. 6.10, but $\lambda = 1.7$ and $\varepsilon = 0.006$ (Deb, Giri, Chakrabarti 2017).

and accordingly, it is hard to collimate the outward flow by the field lines of similar strength. In Fig. 6.10(i-p), the outflow rate is plotted after the magnetic flux tubes have either gotten away from the simulation box or fallen towards the black hole. We see that the impacts of the magnetic flux tubes have begun to blur away. For the case of Fig. 6.10 (i, j, m, and n), the outflow rate is plotted long after the flux tube has gone away or fallen into the black hole. In these cases, it is clear that the impacts of the flux tubes have diminished significantly and the outflow rates of magnetic and non-magnetic cases nearly match. Since for the case demonstrated in Fig. 6.10 (k) and (o), the radial variation of the outflow rate is plotted just a couple of tens of dynamical time after the flux tubes escape from the simulation box, the outflow rates of magnetic and non-magnetic cases do not match, however, the tendency that they approach each other is clear. In Fig. 6.11 (i-p), the fading away of the impacts of the magnetic field is particularly obvious for the flux tubes with high injected σ and in the cases Fig. 6.11(k, o, l, p), the outflow rate for both magnetic and non-magnetic cases almost match with one another. Figure 6.12 demonstrates time variation of the aggregate outflow rate for upper and lower quadrants. The outflow rate rises when the magnetic flux tube stays in the stream yet when it leaves the system, the outflow rate returns back to that of the non-magnetic flow.

As the outflowing matter gets squeezed and squirts off along the vertical axis because of the presence of the magnetic flux tube, the z -component of the velocity

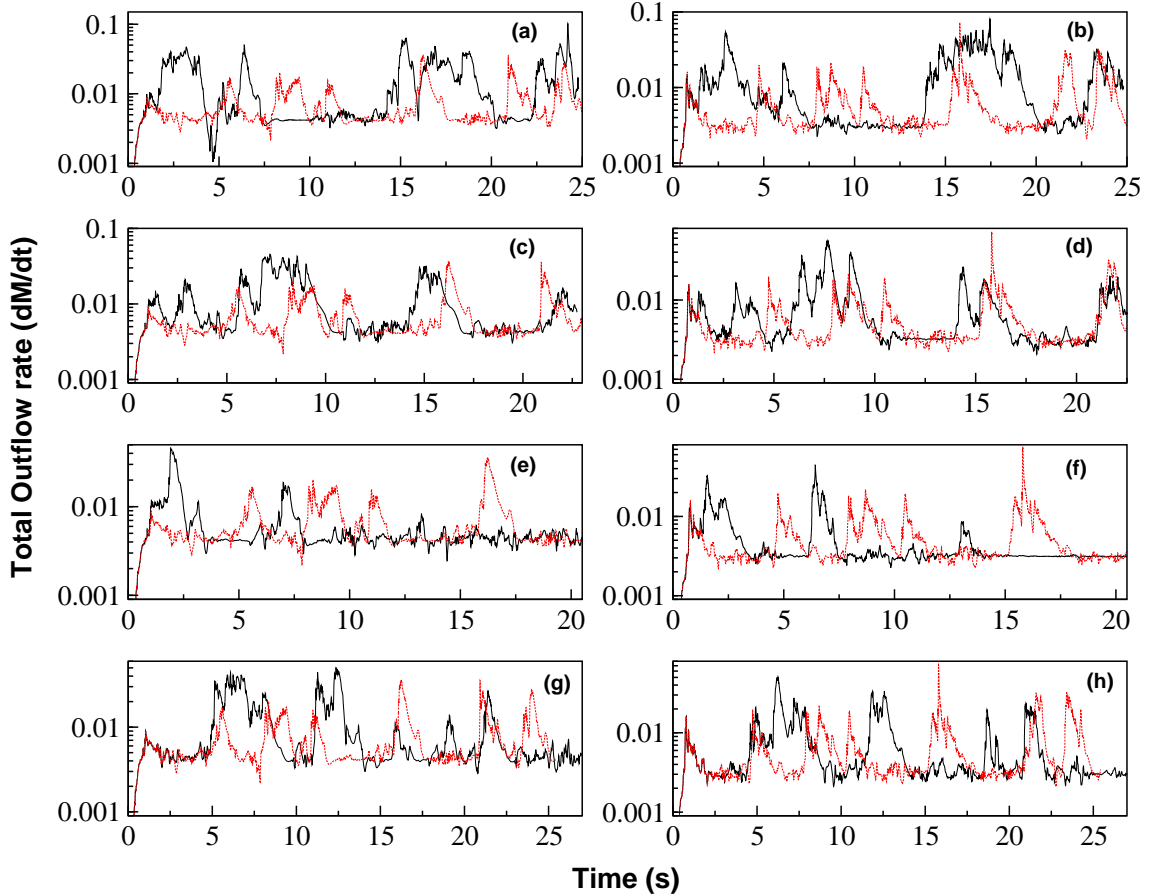


Figure 6.12: Time variation of the total outflow rate for magnetic and non-magnetic cases with angular momentum 1.6 and specific energy 0.002. Panels (a,c,e,g) represents net outflow rate for upper quadrant and panels (b,d,f,h) represents total outflow rate for lower quadrant of the flow. Solid line represents total outflow rate for magnetic cases and dashed line represents the non-magnetic cases. Panels (a,b), (c,d), (e,f), and (g,h) are drawn for flux tube with cross sectional radii 0.001, 0.005, 0.01, $0.1 r_g$ (Deb, Giri, Chakrabarti 2017).

of the matter is observed to increase altogether in contrast with the non-magnetic situation. This means that within the site of the toroidal flux tube, the outflowing matter is accelerated. To demonstrate that we captured this impact as well, in Figs. 6.13 and 6.14 we plot the contour maps of the differential speed, i.e., the difference between z-component of velocities for the magnetic and non-magnetic cases.

In Figs. 6.13 and 6.14, upper and lower panels demonstrate that the acceleration of matter velocity in the outflowing region of the disc is conspicuous in both the upper and lower quadrants of a two-quadrant flow. Every one of Figs. 6.13(a-h) and Figs.6.14(a-h) is drawn for various cross-sectional radii of flux tubes. Here, σs are the usual set for which previous Figures are drawn. The times for which the maps are drawn are similar as specified in the Figures indicating collimations of the outflow. We plotted $(v_{z,mag} - v_{z,non-mag})$. If the difference is positive that will imply that due to the presence of magnetic flux tubes the z-component of the velocity is increased i.e., the fluid flow in that region has been accelerated. Figure 6.13 is drawn for $\lambda = 1.6$ and Fig. 6.14 is drawn for $\lambda = 1.7$. In Fig. 6.13, it can be seen that for every one of the cases the z velocity of magnetized flow has increased within $5 - 50r_g$ in the radial direction for both the upper and lower quadrants and the maximum velocity difference has gone up to $0.36c$ in some instances. In contrast to Fig. 6.13, in Fig. 6.14, the region where the z-velocity of magnetized stream increases is wider and it extends up to a radial separation of $100 r_g$. For this situation, the maximum value of the velocity difference that can be achieved is $0.18c$. This is much lower than what is found in Fig. 6.13. This dissimilarity is because of the fact that for higher angular momentum the centrifugal force is higher and the flow is difficult to collimate as in Fig. 6.10 and hence the acceleration of jets/outflows by the field lines infused with similar initial strength was reduced.

6.4 Viscous magnetized disc

In this section we will discuss about viscous magnetized flow where we have added viscosity in the flow and have injected a single magnetic flux tube inside the flow from the outer boundary near the equatorial plane. The angular momentum of the flow is considered to be 1.6. Here we have considered α viscosity and the α profile is implemented in the same way as it was done in non-magnetized viscous flow as discussed in the previous chapter. Here, we have considered

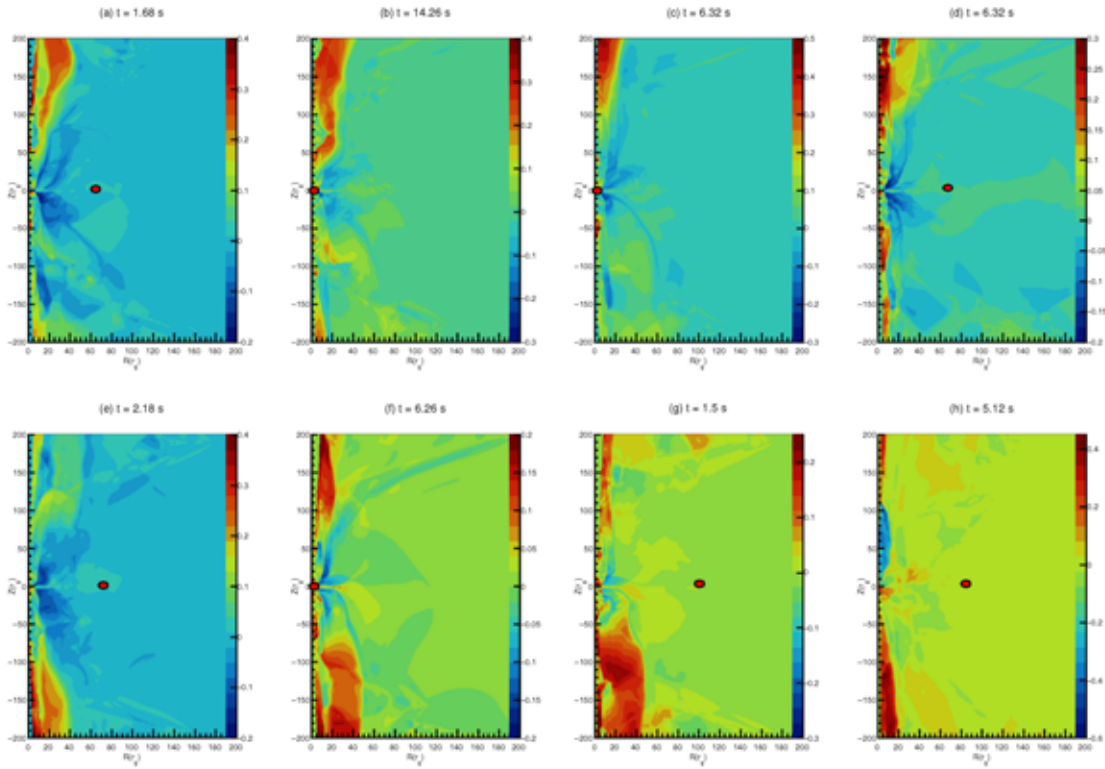


Figure 6.13: Map of the difference between z -velocity of magnetized and non-magnetized flows. (a-d) represent the upper quadrant and (e-h) represent the lower quadrant of a two quadrant flow. Each pair of panels (upper and lower) represent different cross sectional radius. Here, σ ($= 0.001, 0.005, 0.01, 0.1 r_g$). Angular momentum (λ) is 1.6 and specific energy (ϵ) is 0.002. Each panel is drawn for different times. The circles drawn in the panel give the position of flux tube at times for which the panels are drawn (Deb, Giri, Chakrabarti 2017).

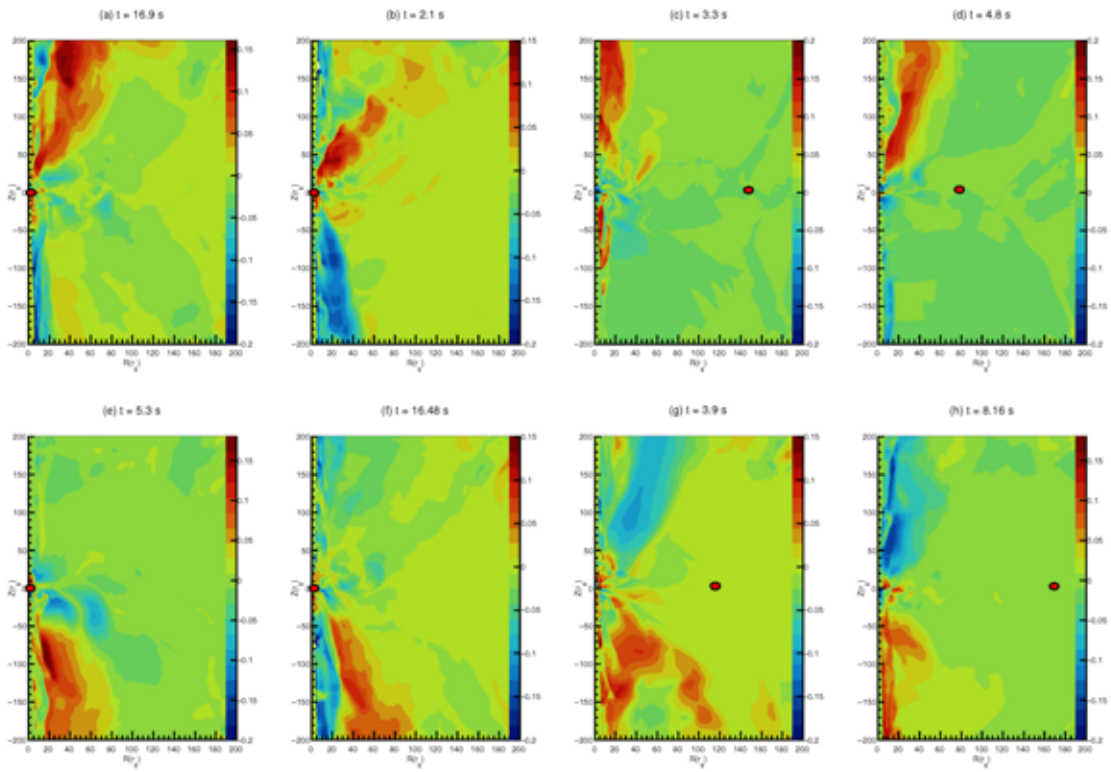


Figure 6.14: Same as Fig. 13, but $\lambda = 1.7$ and $\varepsilon = 0.006$. The time written in each panel is the same as Fig. 6.11 (Deb, Giri, Chakrabarti 2017).

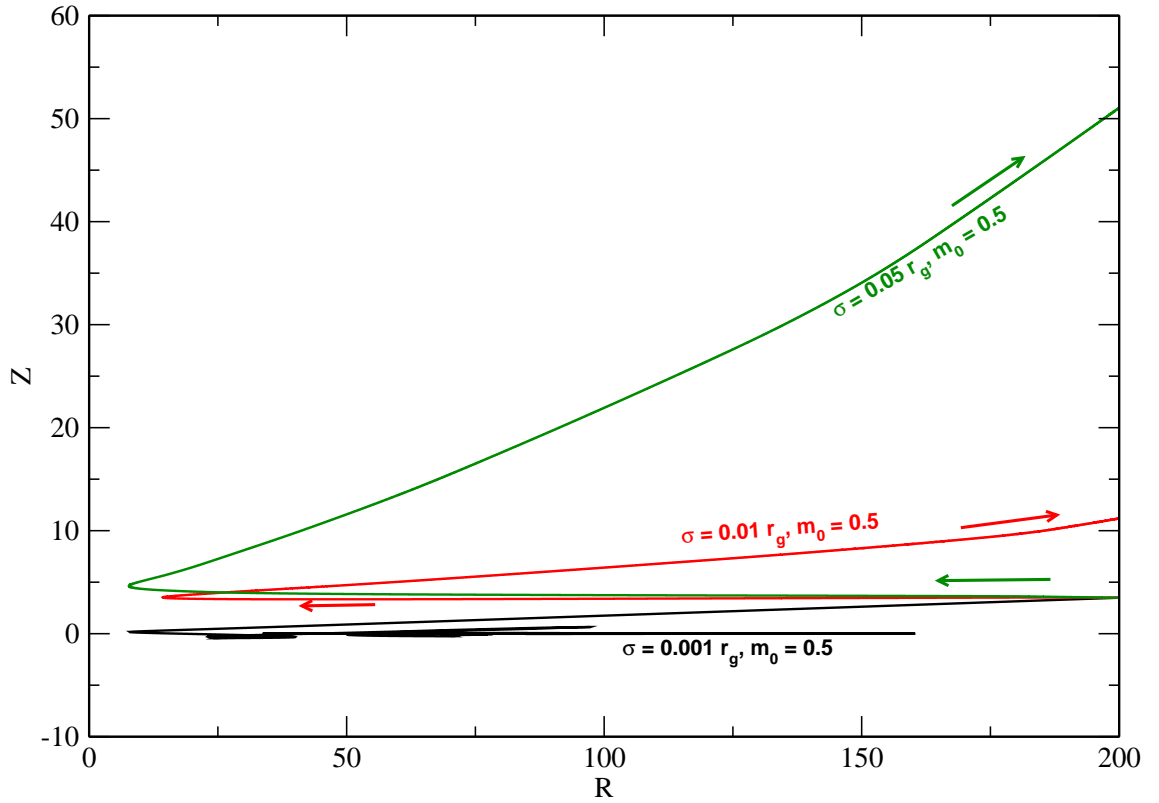


Figure 6.15: Trajectories of flux tubes injected from the outer boundary i.e., $r = 200r_g$ and $\theta = 89^\circ$ with zero initial velocity. Trajectories are in $r = R \sin \theta$ vs. $z = R \cos \theta$ plane. The trajectories are drawn for a flow with angular momentum $\lambda = 1.6$ and energies 0.001. σ is the cross sectional radii of the injected flux tubes. Here σ values are $0.001 r_g$, $0.01 r_g$, and $0.05 r_g$.

initial buoyancy factor (m_0) to be 0.5. With the addition of viscosity, angular momentum of the flow no longer remains constant and the effects of Coriolis force may be prominent (CD94, DC94) In Fig-6.15 we have plotted the trajectories of the magnetic flux tube for viscous flow. The initial cross sectional radii are $\sigma_0 = 0.001, 0.01, 0.05 r_g$. From this figure we can observe that the flux tubes with smaller cross sectional radii can undergo oscillations and eventually will be anchored inside the disc. However, those with bigger cross-sections, flux tubes will be expelled from the disc. In this case, since initial buoyancy factor is a few times higher than what we have used in inviscid case, the magnetic buoyancy force is also higher than the inviscid case which is evident from Fig-6.16. In this Figure, we have plotted the magnitude of the buoyancy force for two different M_0 . The

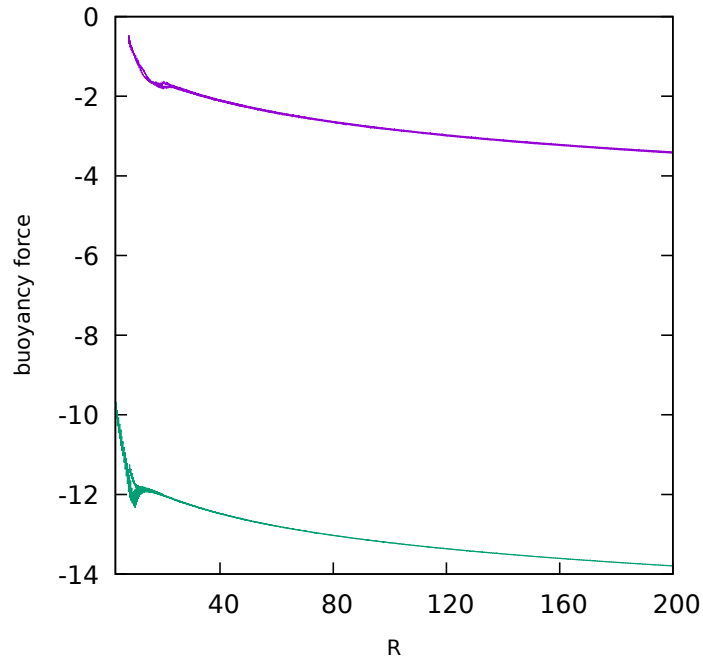


Figure 6.16: Comparison between radial distribution of magnitude of buoyancy force for $m_0 = 0.01$ (green) and $m_0 = 0.5$ (magenta).

profile with higher M_0 is drawn for viscous case and the lower one is for inviscid case. We now investigate if the outflows are collimated as what we have seen in inviscid case. For that purpose, we calculate the radial distribution of outflow rate for magnetized viscous flow and compare it with non-magnetized viscous flow.

Figures 6.17(i) and (ii) show a comparison between the radial distribution of outflow rate of magnetized and non-magnetized flow for upper and lower quadrants respectively. In these two Figures, we can see that the outflow is well collimated in presence of magnetic field in the same way as in an inviscid flow.

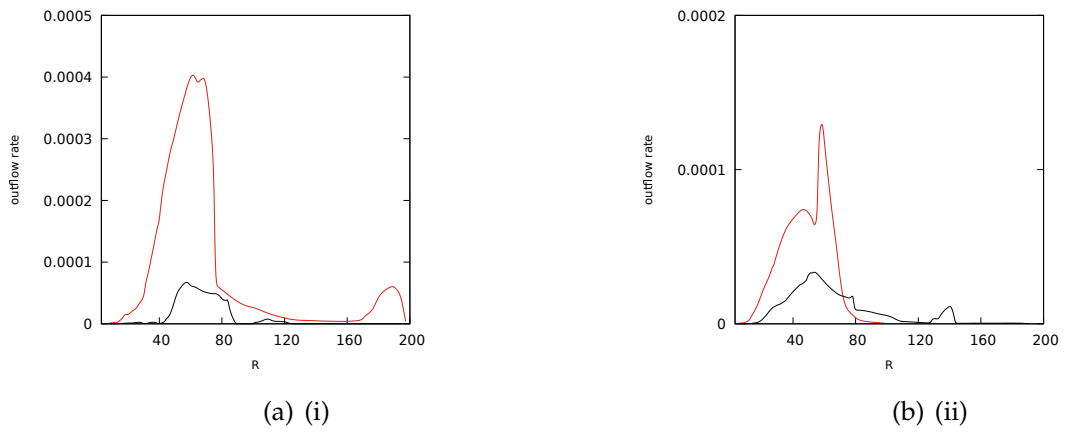


Figure 6.17: Comparison between radial distribution of outflow rate of magnetized and non-magnetized viscous flows. Panel (i) is drawn for upper quadrant and panel (ii) is drawn for lower quadrant at $t = 1.2s$.

Chapter 7

Conclusions & Future Work

Here we summarize the main conclusions of the work. This will be followed by the current activities and the future plans.

7.1 Conclusions

In two component advective flow (TCAF) paradigm, formation of outflow, collimated or not, is coupled with the formation and structure of the CENBOL as this acts as the base of the outflow (Chakrabarti 1999). These outflows can be accelerated either by hydrodynamical processes (Fukue 1982; Chakrabarti 1986) or radiative processes (Chattopadhyay & Chakrabarti, 2002; Chattopadhyay, Das & Chakrabarti, 2004) or by sudden collapse of magnetic field lines which eventually destroys the inner part of the disc causing the acceleration (Nandi, Chakrabarti, Vadawale & Rao, 2001). Magnetic field may not be dynamically important in explaining spectral or timing properties of the black hole and the accretion process as a whole. In TCAF paradigm, collimation of jets are initiated by hoop stress of toroidal the magnetic fields which are expelled from the accretion flow. In this thesis our goal was to examine if this toroidal flux tube is injected in a time dependant viscous or inviscid flow, whether it will be able to collimate and accelerate the outflow. We also wish to investigate the dynamics of the field lines inside a time dependent disc by improving on the earlier works of Chakrabarti & D'Silva (1994) and D'Silva and Chakrabarti (1994) where a steady thick disc was used. Here, we successfully demonstrate the dynamics using a set of equations which was historically constructed for sun (Choudhuri & Gilman, 1987; Choudhuri 1989, 1990 and implemented in Accretion disks by CD94 and DC94). We successfully show that indeed toroidal magnetic field can dynamically collimate

and accelerate the outflow.

In Chapter 1 we presented a brief introduction to the astrophysical black holes and accretion discs which surround them. I presented how theories of accretion discs evolved with time by discussing the theoretical models which explained many observed phenomena. After this we delved into the discussion of jets and outflows and their ubiquitous nature. A discussion regarding the general potential and pseudo-Newtonian potential described in Paczyński & Wiita 1980 was presented in §1.1. Next, in §1.2 we discussed about the accretion processes followed by a brief discussion on time independent theoretical models of accretion disc in §1.3. In §1.4 we discussed about the Jets and outflows and effects of the magnetic fields. Here, we have first started with describing the ubiquitous nature of the jets and outflows as they can be found in a wide array of astrophysical objects such as AGNs, Young Stellar Objects (YSO), Stellar mass black holes and microquasars etc. Next, we presented how the idea of magnetized disc and its connection to launching of collimated jets is evolved throughout the time for compact objects. We then discussed about the pioneering work of Chakrabarti & D'Silva (1994a) (CD94) and D'Silva & Chakrabarti (1994b) (DC94) where they demonstrated how a toroidal magnetic flux tube injected inside a steady thick disc (Rees et al. 1982, Paczyński & Wiita 1980) having a power law angular momentum distribution inside the disc (Paczyński & Wiita 1980, Chakrabarti 1985) behaves. In CD94 they explained how a flux ring can be expelled towards the "chimney" and in DC94 they showed that flux tubes can be anchored which mimics a solar type interior.

In Chapter 2, we discussed about the hydrodynamic simulation of both non magnetized and magnetized accretion flow around black holes. We started from the basic conservation equations that describe the dynamics of a fluid flow and modified it for inviscid non-magnetized accretion flow and discussed about the hydrodynamic equations in a compact form both in terms of conservative and primitive variables. In doing so we presented a discussion regarding construction of a set of Jacobian matrices which reduces the problem to an eigensystem with real eigenvalues and left and right orthonormal eigenvectors. We then briefly discuss the numerical techniques involved in solving the system and also a numerical scheme named Total Variation Diminishing scheme (TVD) (Harten, 1983) and also the Riemann solver. We then introduce viscosity as well as radiative cooling in the system and modify the source term matrix accordingly. We also point out the procedure to implement the cooling depending the optical depth of the flow. We then incorporate the magnetic force terms converting the accretion

flow into a magnetized one and briefly discuss the equations of motion for the flux tube and the thermodynamic properties of the flux tubes which are necessary to compute the dynamics of the field lines. In Chapter 3, we discussed the simulation procedure in detail. We briefly described the simulation box and the co-ordinate system used. Since to solve the system of partial differential equations, the boundary conditions are to be provided, we have also discussed about the boundary conditions invoked in the system to generate two quadrant inviscid and viscous flow. We have discussed the initial condition needed for the hydrodynamics and for the computation of the dynamics of the flux tube as well. We then test our code for both magnetized and non-magnetized spherical flows and compare the results.

In Chapter 4, we describe the time dependent two quadrant inviscid flow. Here we have not invoked any reflection boundary condition unlike Giri et al. (2010) and thus we have allowed the flow to undergo vertical oscillations along with the horizontal oscillation. We have injected the matter at the outer boundary maintaining the vertical equilibrium. We get very interesting results. For low angular momentum cases we find that the flow remains more or less stable and symmetric with respect to the equatorial plane. For angular momentum 1.6 we can see that CENBOL is formed but it is not stable as with time a repetitive formation and destruction of CENBOL occurs. As we go towards higher angular momentum, the flow becomes very turbulent and it is observed from the simulation that at some times a part of the CENBOL is tilted towards the upper quadrant of the flow and for other times the CENBOL is tilted towards the lower quadrant. This shifting of CENBOL has an effect on the outflow also. As the CENBOL shifts towards the upper quadrant, the total outflow from the upper quadrant becomes significantly higher than the lower quadrant and opposite happens when CENBOL tilts toward the lower quadrant. Thus, when plotted simultaneously an anti-correlation is seen between the outflows in the upper and the lower quadrants. This feature becomes more and more prominent as we increase the angular momentum.

In chapter 5, we wanted to see if radiative cooling and viscosity is added what happens to the flow and whether the Keplerian disc is formed or not as in Giri & Chakrabarti 2013 (GC13). We introduce α viscosity following the same prescription as GC13 as appropriate for our set up. We also incorporated two power-law type coolings depending upon the optical depths of the flow. From the simulation results, we see that for the flow with higher angular momentum, unlike the inviscid cases, the turbulent Eddies were smeared out and the flow become stable. Thus we believe that the violent behaviour of the inviscid flow could be an

artefact of strict shock capturing in TVD code itself. A Keplerian disc is formed on the equatorial plane of the flow when the angular momentum distribution obtained from the simulation matches exactly with the theoretical Keplerian distribution. The temperature inside the disc has the distribution of $\sim r^{-0.79}$ which almost matches with the analytical distribution of $\sim r^{-3/4}$.

In Chapter 6, we studied the dynamics of magnetic flux tubes which are released at the outer edge of a time dependant two quadrant thick advective disc and their role in collimation and acceleration of the jet and outflow from the upper boundary. In earlier studies, such as CD94 and DC94, simulations were carried out to study the dynamics of flux tubes in the realm of time independent thick disc (Paczyński & Wiita 1980). The general conclusion drawn were that depending upon the initial release points, initial cross-sectional radius of the flux tube, angular momentum distribution of the flow the flux tubes can emerge from different parts of the disc also at the vortex like opening called "chimney" making it a magnetically active region. However, it is also possible to construct physical models of time independent thick accretion discs with proper entropy conditions that can provide the storage of weaker flux tubes that instead of being expelled away tend to oscillate around equipotential surfaces until they are amplified and buoyant and leave the system. In order to have a more realistic picture, in Chapter 6, we studied the dynamics of the flux tubes released in a time dependent accretion after removing the reflection symmetry (Deb et al. 2016) condition. We do not use full Magnetohydrodynamic equations and thus flux tube we used are not sheared or reconnected. We simply followed the paths of the flux tubes through the flow and exchange momentum between them which the matter diffusion through the flux tubes were chosen to be instantaneous. We also answered whether these magnetic flux tubes aid in the acceleration and collimation of the jets or not. In order to do this we have injected a single flux tube in each simulation, at the outer boundary of the disc after a few dynamical timescales so that the initial transient phase of the flow is over and the flow settles down to a stationary solution. We assumed that flux tube is toroidal which is probably a good assumption in a rapidly rotating flow. It can be seen from the simulation that depending upon the initial cross sectional radius of the flux tube and the flow parameters, such as the angular momentum and energy, flux tubes can move directly towards the chimney or oscillate till it is expelled away. However, the shock location becomes higher for higher angular momentum and thus the amplification of the flux tubes are larger and have chances for ejection of flux tubes earlier on. The same argument stands for specific energy also. As the shock location moves further out with increase of

energy (Chakrabarti 1989) the post shock region becomes bigger making the magnetic field difficult to be advected in since the drag force considerably increases in regions of high density such as the post shock region. Increase in magnetic field cross section would increase in buoyancy force as well. We also find that in case of certain angular momenta and energies, (i) the outflow rates ($\dot{M}(r)$) from both upper and lower quadrants increase significantly in comparison to the outflow rates with respect to the non-magnetic cases (ii) The outflow rate is reaching its maximum value at much smaller radius, i.e., the spread of the outflow at the upper and lower boundaries has reduced significantly. It is to be noted that though we do not see much fluctuations on a day to day basis in the observed jets, at the base, the fluctuations are natural since the inner edge could be oscillating and produce jets with sporadic rates. We note that the pinch felt by the outflow causes its velocity to increase. At the start of the outbursts, the shock location is higher making the CENBOL bigger in size (Hard state) and above discussion suggests that the jets would be weakly collimated at the base. If the magnetic field in the companion is strong so that the disk intercepts it and amplifies and produces more flux tubes, we can expect stronger collimation of outflows in such systems. If the companion star is non-magnetic and the field can only enter sporadically, the outflow will not be well collimated. In our simulation, we showed that as long as the flux tube is close to the vertical axis, the outflow is collimated, and it achieves a high speed. When the flux tubes leave the disc, the outflow returns to the original un-collimated shape. We repeat our simulation for viscous case also and we find almost similar result.

7.2 Future Work

Though we studied one tube at a time, our final goal would be to understand what happens to the flow when an ensemble of flux tubes enters the disc, which is possibly the case in the realistic scenario. In that case, we will expect a faster and better collimated steady jet. Thus we have a clear prediction that magnetic activity of the companion (or, the surroundings in case of super-massive black holes) is directly correlated with the emanation of stronger and well collimated jets from the inner regions of the disc.

Of course some flux tubes may still pop-up and produce corona, but the probability does not seem to be strong, judging by our simulation results. Furthermore, presence of small scale turbulence may tear off fields of larger σ into smaller

ones which then move in further. These flux tubes may also be responsible for a large number of astrophysical processes, such as the variability of blazars, magnetic winds, production of high energy particles in coronae through Fermi acceleration processes etc. (DC94). In many objects such as, GRS 1915 + 105 the variability classes namely χ_1 , χ_3 and β are found to be associated with strong radio jets (Nandi et al. (2001), Naik & Rao (2000), Vadawale et al. (2003), Vadawale et al. (2001)). In case of β class it is suspected that magnetic tension in the post-shock region becomes the most dominant component causing an abrupt collapse of this region. This may signify that the collapse of the magnetic flux tubes causes a huge acceleration of jets (Nandi et al. 2001, Naik & Rao 2000, Vadawale et al. 2001, Vadawale et al. 2001). We observed that only the initially filamentary flux tubes which are produced due to the presence of shear in the disc could be advected to the innermost regions of the disc. It is not impossible that many of such filaments merge due to higher density and make stronger flux tubes which then suddenly collapse and remove the inner region altogether. The opposite would be true when small scale turbulence is strong. These aspects will be dealt with in future. In case of the Sun, magnetic flux tubes are known to be anchored between the radiative core and convective envelope and they come out to the surface due to Parker instabilities. This is possible since the time scale of instability is much shorter as compared to the buoyancy time scale. However, in case of thick flows around black holes, pressure gradients are very strong and the flux tube may escape as a whole, especially those with stronger fields (CD94, DC94, Deb, Giri, Chakrabarti 2017). By "escaping the disc" we mean that when the flux tubes enter into the funnel (Chimney) or leave the upper computational grid we assume that they escaped the disc. However due to topological constraints, they are not destroyed and will collimate the jet. If the jet is not formed, then they can move sideways and leave the system altogether (Deb, Giri, Chakrabarti 2017).

References

- Batchelor G. K., 1967, *An Introduction to Fluid Dynamics*. Cambridge Univ. Press, Cambridge
- Blackman E. G., 1996, *ApJ*, 456, L87
- Blandford R. D., Payne D. G., 1982, *MNRAS*, 199, 883
- Blaes, O. M., Arras, P. & Fragile, P. C., 2006, *MNRAS*, 369, 1235-1252
- Chakrabarti, S.K. 1989, *ApJ* 347, 365 (C89)
- Chakrabarti, S.K. 1990 *Theory of Transonic Astrophysical Flows* (World Scientific: Singapore) (C90)
- Chakrabarti, S.K. 1993, *MNRAS* 259, 410
- Chakrabarti, S.K. 1996, *MNRAS* 283, 325
- Chakrabarti, S.K., Acharyya, K. A. & Molteni, D., 2004, *A&A*, 421
- Chakrabarti, S.K. & Das, S., 2001, *MNRAS*, 327,808
- Chakrabarti, S.K. & Molteni, 1993, *ApJ* 417, 672
- Chakrabarti, S.K. & Molteni, D. 1995, *MNRAS*, 272, 80
- Colbert E. J. M., Mushotzky R. F., 1999, *ApJ*, 519, 89
- Chattopadhyay, I & Chakrabarti, S. K. *MNRAS*, 333, 454 (2002)
- Chattopadhyay, I., Das, S. & Chakrabarti, S.K., *MNRAS*, 348, 846 (2004)
- Chakrabarti S. K., 1985, *ApJ*, 288, 1
- Chakrabarti S. K., 1986, *ApJ*, 303, 582

- Chakrabarti S. K., Bhaskaran P., 1992, MNRAS, 255, 255
- Chakrabarti S. K., D'Silva S., 1994, ApJ, 424, 138
- Chakrabarti S. K., Rosner R., Vainshtein S. I., 1994, Nature, 368, 434
- Choudhuri A. R., Gilman P. A., 1987, ApJ, 316, 788
- Coroniti F. V., 1981, ApJ, 244, 587
- D'Silva S., Chakrabarti S. K., 1994, ApJ, 424, 149
- Deb A., Giri K., Chakrabarti S. K., 2016, MNRAS, 462, 3502
- Eardley D. M., Lightman A. P., 1975, ApJ, 200, 187
- Fendt C., Camenzind M., 1996, A&A, 313, 591
- Ferriz-Mas A., Schuessler M., Anton V., 1989, A&A, 210, 425
- Fukue J., 1982, PASJ, 34, 483
- Galeev A. A., Rosner R., Vaiana G. S., 1979, ApJ, 229, 318
- Giri K., Chakrabarti S. K., Samanta M. M., Ryu D., 2010, MNRAS, 403, 516
- Giri K., 2015, Numerical Simulation of Viscous Shocked Accretion Flows Around Black Holes, by K. Giri. Springer Theses. ISBN 978-3-319-09539-4. Berlin: Springer-Verlag, 2015
- Giri K., Chakrabarti S. K., 2013, Monthly Notices of the Royal Astronomical Society, Volume 430, Issue 4, p.2836-2843
- Harten A., 1983, J. Comp. Phys., 49, 357
- Heyvaerts J., Norman C., 1989, ApJ, 347, 1055
- Galeev A. A., Rosner R., Vaiana G. S., 1979, ApJ, 229, 318
- Giri K., Chakrabarti S. K., Samanta M. M., Ryu D., 2010, MNRAS, 403, 516
- Giri K., 2015, Numerical Simulation of Viscous Shocked Accretion Flows Around Black Holes, by K. Giri. Springer Theses. ISBN 978-3-319-09539-4. Berlin: Springer-Verlag, 2015

- Giri K., Chakrabarti S. K., 2013, Monthly Notices of the Royal Astronomical Society, Volume 430, Issue 4, p.2836-2843
- Harten, A., 1983, J.Comp. Phys., 49, 357
- Hawley, J.F. & Smarr, L.L., 1986, AIPC, 144, 263
- Hawley, J.F., Smarr, L.L., & Wilson, J.R., 1984a, ApJ, 277, 296
- Hawley, J.F., Smarr, L.L., & Wilson, J.R., 1984b, ApJ, 55, 211
- Heyvaerts J., Norman C., 1989, ApJ, 347, 1055
- Königl A., 1989, ApJ, 342, 208
- Longcope D. W., Klapper I., 1997, ApJ, 488, 443
- Lovelace R. V. E., 1976, Nature, 262, 649
- Lynden-Bell D., 1978, Phys. Scr., 17, 185
- Molteni D., Ryu D., Chakrabarti S. K., 1996, ApJ, 470, 460
- Molteni, D., Acharya, K., Kuznetsov, Oleg, Bisikalo, D., Chakrabarti, Sandip K. 2001, ApJ, 563, 57
- Molteni, D., Lanzafame, G., & Chakrabarti, S.K., 1994, ApJ, 425, 161
- Molteni, D., Ryu, D., & Chakrabarti, S. K., 1996b, ApJ 470, 460
- Molteni, D., Sponholz, H., & Chakrabarti, S.K., 1996a, ApJ, 457, 805
- Paczynski, B. & Wiita, P. J., 1980, 88, 23
- Patruno A., Zwart S. P., Dewi J., Hopman C., 2006, MNRAS, 370, L6
- Ryu, D., Brown, G. L., Ostriker, J. P. & Loeb, A., 1995, ApJ 452, 364
- Rees M. J., Begelman M. C., Blandford R. D., Phinney E. S., 1982, Nature, 295, 17
- Ryu D., Brown G. L., Ostriker J. P., Loeb A., 1995, ApJ, 452,364
- Ryu D., Chakrabarti S. K., Molteni D., 1997, ApJ, 474, 378
- Sakimoto P. J., Coroniti F. V., 1989, ApJ, 342, 49

- Eggum, G. E., Coroniti, F. V. & Katz, J. I. 1985, *ApJ*, 298, L41-L45
- Fryxell, B. A., Taam, Ronald E. 1988, *ApJ* 335, 862
- Camenzind M., 1989, in Belvedere G., ed., *Astrophysics and Space Science Library* Vol. 156, *Accretion Disks and Magnetic Fields in Astrophysics*. pp 129-143, doi:10.1007/978-94-009-2401-714
- Shakura, N. I. & Sunyaev, R. A. (1973). *Astronomy & Astrophysics*, 24, 337.
- Abramowicz, M. A. (1985), *PASJ*, 37, 727.
- Abramowicz, M., Jaroszynski, M., & Sikora, M. (1978). *Journal of Astrophysics & Astronomy*, 63, 221.
- Abramowicz, M., & Zurek, W. H. (1981). *The Astrophysical Journal*, 246, 314.
- Bondi, H. & Hoyle, F. (1944). *MNRAS*, 104, 273.
- Bondi, H. (1952). *MNRAS*, 112, 195.
- Chakrabarti, S. K. & Titarchuk, L. G. (1995). *The Astrophysical Journal*, 455, 623.
- Landau, L. D., & Lifshitz, E. M. (1959). *Fluid Mechanics*. Oxford: Pergamon Press.
- Novikov, I. & Thorne, K. S. (1973). In: C. DeWitt & B. DeWitt (Eds.), *Black Holes* (pp. 343) New York: Gordon and Breach.
- Ostriker, J. P., McCray, R., Weaver, R., & Yahil, A. (1976). *The Astrophysical Journal*, 208, 61.
- Rees M. J., 1984, *Ann. Rev. Astron. Astrophys.*, 22, 471
- Rees M., Begelman M., Blandford R., Phinney E., 1982, *Nature*, 295, 17
- Marscher, A. P., & Gear, W. K. 1985, *ApJ*, 298, 114
- Marscher, A. P., Gear, W. K., & Travis, J. P. 1992, in *Variability of Blazars*, ed. E. Valtaoja & M. Valtonen(Cambridge U. Press), 85
- Hughes, P. A., Aller, H. D., & Aller, M. F. 1985, *ApJ*, 298, 301
- Hughes, P. A., Aller, H. D., & Aller, M. F. 1989, *ApJ*, 341, 54
- Blandford, R. D., & Königl, A. 1979, *ApJ*, 232, 34

- Aller, M. F., Aller, H. D., & Hughes, P. A. 2003, *ApJ*, 586, 33
- Camenzind, M. 2005, *Mem. S.A.It.*, 76, 98
- Türler, M., Courvoisier, T. J.-L., & Paltani, S. 2000, *A&A*, 361, 850
- Vlahakis, N., & Königl, A. 2004, *ApJ*, 605, 656
- McHardy, Ian & Czerny, Bozena, *Nature* (ISSN 0028-0836), vol. 325, Feb. 19, 1987, p. 696-698.
- Vadawale S. V., Rao A. R., Nandi A., Chakrabarti S. K., 2001, *A&A*, 370, L17
- Vadawale S. V., Rao A. R., Naik S., Yadav J. S., Ishwara-Chandra C. H., Pramesh Rao A., Pooley G. G., 2003, *ApJ*, 597, 1023
- You S., Yun G. S., Bellan P. M., 2005, *Phys. Rev. Lett.*, 95, 045002
- Nandi, A.; Chakrabarti, S. K.; Vadawale, S. V.; Rao, A. R., *Astronomy and Astrophysics*, v.380, p.245-250 (2001)
- Dewangan G. C., Titarchuk L., Griffiths R. E., 2006, *ApJ*, 637, L21